UNIVERSIDAD NACIONAL AUTÓNOMA DE MÉXICO

PROGRAMA DE POSGRADO EN CIENCIAS DE LA TIERRA
CENTRO DE GEOCIENCIAS

RELACIÓN ENTRE EPISODIOS TECTONO-MAGMÁTICO CRETÁCICO TARDÍO - OLIGOCENO TEMPRANO Y EL DESARROLLO DE MULTIPLES EVENTOS MINERALIZANTES DE PLATA – ORO EN EL DISTRITO MINERO SAN DIMAS, SIERRA MADRE OCCIDENTAL, MÉXICO

TESIS QUE PARA OPTAR POR EL GRADO DE:
DOCTORADO EN CIENCIAS DE LA TIERRA

PRESENTA:
MSc PAULA ANDREA MONTOYA LOPERA

TUTORES
DR. LUCA FERRARI
DR. GILLES LEVRESSE
CENTRO DE GEOCIENCIAS

MIEMBRO DEL COMITÉ TUTOR
DR. ÁNGEL NIETO
CENTRO DE GEOCIENCIAS

CDMX, AGOSTO 2020

HOJA EN BLANCO

Declaración de originalidad

"Declaro conocer el Código de Ética de la Universidad Nacional Autónoma de México, plasmado en la Legislación Universitaria. Con base en las definiciones de integridad y honestidad ahí especificadas, aseguro mediante mi firma al calce que el presente trabajo es original y enteramente de mi autoría. Todas las citas de, o referencias a, la obra de otros autores aparece debida y adecuadamente señaladas, así como acreditadas mediante los recursos editoriales convencionales."

Agradecimientos

Este estudio de investigación fue posible gracias al patrocinio de los proyectos CONACYT - CB 237745-T otorgado a L. Ferrari y DGAPA-PAPIIT – IN106017 otorgado a G. Levresse, y fue desarrollado en Centro de Geociencias de la Universidad Autónoma de México (UNAM), campus Juriquilla. Me gustaría también dar sinceros agradecimientos a First Majestic Silver Corp., que apoyó proporcionando información y soporte logístico para el desarrollo de este estudio. Expreso también, grandes agradacimientos a mis tutores Dr. Luca Ferrari y Dr. Gilles Levresse ya que sin su ayuda y asistencia el proyecto no hubiera sido posible. Especiales agradecimientos al Dr. Ángel Nieto, Dra. Teresa Orozco, Dra. Eliza Fitz, Dr. Aldo Ramos, Dr. Martin Valencia por su asistencia y guía durante diferentes etapas del proyecto doctoral. A los Ingenieros Luis Mata, Nicolas Landón y Miguel Pérez por compartir su basto conocimiento y soporte logístico durante las salidas de campo.

Agradezco también a los diversos laboratorios dentro y fuera de UNAM, no solo por la posibilidad de usar sus equipos, sino también por el apoyo intelectual para el desarrollo exitoso de este doctorado: Dr. Luigui Solari, Dr. Carlos Ortega, Dr. Fanis Abdullin, por su asistencia con técnicas U/Pb y trazas de fisión; Dra. Gabriela Hernandez, Dra. Margarita López por su asistencia con las técnicas Ar/Ar; Dra. Marina Vega y Ing. Carlos Linares López por asistencia con microanálisis químicos de minerales con microsonda electrónica ; Dr. Pedro Morales, M.Sc. Edith Cienfugos Alvarado, MSc Francisco Javier Otero Trujano, por su asistencia en isotopía estable. Juan Tomás Vazquez y Manuel por la elaboración de láminas delgadas y asistencia en trituración y separación de minerales. M.Sc. “Conchis” por su asistencia en recubrimiento de láminas, Dr. Andrea Luca Rizzo, Maria Grazia y Mariano Tantillo de la Universidad de Palermo (INGV) en Italia por su ayuda en la preparación de muestras, análisis de gases nobles y sus valiosas discusiones y aportes en la escritura del documento. Asimismo, agradezco a Seequent Limited por otorgar una licencia académica del software Leapfrog GEO y EAGE.

Por último, pero no los menos importantes a todos mis colegas de doctorado los cuales de una manera positiva aportaron de una u otra forma al desarrollo de la investigación, Dra.

Tatiana Lobato, Dr. Kurt Wogau, Dra. Maria Isabel Sierra, Dr. Rodrigo León, M.Sc. Vania Ferrer, Dr. Roberto Molina, Dra. Laura Culí, M.Sc. Maria Clara Madrigal, M.Sc. Sebastian Giraldo, M.Sc. Santiago Urquiza, Dr. Mattia Parolari, Dr. Fernando Corbo, Dr. Adolfo Pacheco, M.Sc. Gabriela Contreras y Dra. Paola Botero.

Resumen

El Distrito San Dimas es un clásico referente a nivel mundial de yacimientos epitermales de Ag/Au de baja sulfuración (tipo cuarzo + adularia + sericita) localizado en la Sierra Madre Occidental (SMO) al oeste de México. A pesar de ser un depósito de clase mundial que ha tenido producción por hace más de un siglo, la génesis de sus sistemas vetiformes de variable contenido Ag/Au continua sin ser bien entendido. En el modelo actual, basado principalmente en el Bloque Tayoltita, la evolución del sistema de vetas ha sido dividida en tres fases: (a) temprana, (b) mineralizante y (c) tardía. La fase mineralizante presenta un rango de edades entre ~41 a 32.7 Ma en adularia, y una edad de ~31.9 Ma en sericita. Basado en estas edades, el sistema de vetas del distrito San Dimas fue considerado como el resultado de un solo evento hidrotermal desarrollado en un periodo de ~10 Ma. Éste a su vez se asoció genéticamente al emplazamiento de cuerpos intrusivos de afinidad intermedia con edades K-Ar en el Eoceno tardío. Debido a la fuerte alteración hidrotermal en estas rocas, las edades reportadas probablemente no representan la edad de cristalización de los cuerpos sino una edad de reseteo parcial de los minerales. Por otro lado, el modelo metalogenético tradicional de un solo evento no concuerda con la presencia de vetas con dos orientaciones distintas y relación Au/Ag variable.

Nuevas edades U-Pb en zircón y trazas de fisión en apatito reportadas en este estudio corresponden a tres pulsos magmáticos: uno entre ~77 y 64 Ma asociados al arco laramídico, otro entre ~49 y 45 Ma durante la formación del batolito Piaxtla y el otro entre ~32 y 27 Ma que se relaciona al primer pulso ignimbrítico de la SMO. En este contexto, las edades K-Ar previas de la mineralización estarían ubicadas durante un periodo sin actividad magmática desarrollada entre el segundo y tercer pulso, lo que indica que el periodo continuo de la mineralización de ~10 Ma sugerido en trabajos previos puede deberse al reseteo parcial de algunos minerales.

Los resultados presentados en esta investigación demuestran que el distrito San Dimas exhibe múltiples eventos mineralizantes durante diferentes episodios magmáticos y tectónicos desde el Cretácico Tardío al Oligoceno temprano. Un primer evento está asociado a pórfidos de cobre emplazados en el edad Cretácico Tardío y asociados al arco laramídico.

En el Eoceno, un segundo evento mineralizante desarrolló vetas mesotermales ricas en Ag en sistemas de orientación ~E-W, principalmente de tipo cuarzo-adularia. La formación de estas vetas se estima a temperaturas mayores de 300ºC y profundidades de aproximadamente 3 km, asociadas a etapas finales de formación del batolito Piaxtla. Un tercer evento se caracteriza por vetas epitermales tipo sericita-clorita de baja sulfuración ricas en Au con edades en el Oligoceno temprano, emplazadas en sistemas de orientación NNW-SSE. Para estas vetas se estimaron temperaturas de formación promedio de 250ºC y profundidades someras (< 1km). La geoquímica de los circones indica una asociación con pulsos magmáticos reducidos y fértiles desarrollados al final del primer pulso ignimbrítico de la SMO.

Palabras claves

Sierra Madre Occidental, fluidos hidrotermales, epitermal, mesotermal, telescopeo, plata, oro, San Dimas.

Abstract

The San Dimas (SD) district is a world reference Ag/Au epithermal low sulfidation (quartz + adularia + sericite type) deposit located in the Sierra Madre Occidental (SMO) of western Mexico. Despite being a world class deposit under production for over a century, the genesis of its vein system with variable Ag/Au content is still not well understood. In the current model the vein system has been divided in a traditional early, ore, and late phases at Tayoltita Block. The ore phase ages ranging from ~41 to 32.7 Ma in adularia, and a single age of ~31.9 Ma in sericite. On the basis of these ages, the San Dimas vein system was considered the result of a single hydrothermal event developed over a ~10 Ma period, genetically associated to the emplacement of intermediate intrusive bodies of Eocene age. Given the widespread alteration of these rocks, the K-Ar ages are doubtful and were probably the result of partial resetting of the dated minerals. In addition, the traditional metallogenetic model not only includes genetical ambiguities, but also it was constructed based on the studies of a limited portion of the district.

Our new U-Pb and FT geochronologic study of the district, revealed three main magmatic pulses at ~77-64 Ma (Laramide arc), ~48-45 Ma (Piaxtla batholith) and ~32-27 Ma (first SMO ignimbrite flare up). In this frame previous K-Ar ages would place the mineralization episode during a magmatic lull between the second and third magmatic pulse, confirming our previous suggestion of partial resetting of minerals dated by K-Ar method.

Our revision of mineralized veins and the origin and evolution of the ore-forming fluids and genesis demonstrate that SD exhibits multiple mineralization events during different magmatic and tectonic episodes from Late Cretaceous to early Oligocene. The results suggest that the SD deposit developed through two different mineralization episodes: 1) Ag-dominant mesothermal Eocene veins that formed at temperatures > 350ºC developed at ca. 3 km depth, associated to the final stages of intrusion of the Piaxtla batholith, and 2) epithermal low sulfidation Au-dominant Oligocene veins formed at 250ºC, at shallower depths (<1km), associated to the faults feeding rhyolitic domes developed at the end of the main ignimbrite flare up of the SMO.

Our results highlight the importance of a multidisciplinary approach, such as field observations, geochronological and geochemical studies, to better understand the complexity of the hydrothermal magmatic processes involved in the formation of many Mexican ore deposits and their proper classification

Keywords

Sierra Madre Occidental, hydrothermal fluids, epithermal, mesothermal, telescoping, silver, gold, San Dimas

Tabla de Contenido

Capítulo 1: Introducción

1.1 Introducción

La Sierra Madre Occidental (SMO) es el resultado de diferentes episodios magmáticos y tectónicos ocurridos entre el Cretácico y el Cenozoico, asociados a la subducción de la placa Farallón debajo de la placa norteaméricana y a la apertura del Golfo de California (Ferrari et al., 2005). Estos episodios magmáticos se pueden agrupar en dos grandes eventos: 1) el desarrollo del Arco Larámide (~90-45 Ma) con el emplazamiento de los batolitos de Sonora, Sinaloa y Jalisco y su cobertura volcánica (Fm. Tarahumara y sus equivalentes, Wilson y Rocha, 1949; Ferrari y Rosas-Elguera, 2000; McDowell et al., 2001; Valencia et al., 2013), y 2) un episodio de extensión litosférica que se desarrolla a partir del final del Eoceno favoreciendo la fusión parcial de la corteza con producción de magmas diferenciados que dan origen a la llamada gran provincia silícea de la SMO, caracterizada por dos grandes pulsos ignimbríticos entre ~34-28 Ma y ~24-18 Ma (Ferrari et al., 2014 y 2018). Estos procesos geodinámicos mayores han generado grandes distritos mineros en la SMO, reconocidos a nivel mundial por su importancia económica en la producción de Ag, Au, Cu (Albinson et al., 2001; Camprubí et al., 2001; Camprubí et al., 2003; Levresse et al., 2017; Zamora-Vega et al., 2018). Ferrari et al., (2005) describen de manera general el ambiente geológico, estructural en la SMO y muestran, en la parte sur de la SMO, la complejidad y la multiplicidad de los procesos de mineralización y sus relaciones con los eventos magmáticos a escala regional.

El distrito minero de San Dimas está catalogado como un clásico depósito epitermal de baja sulfuración de Ag/Au de talla mundial (Henshaw, 1953; Clarke, 1986). Éste se encuentra localizado en el flanco occidental de la parte central de la SMO cerca del límite entre los estados de Durango y Sinaloa en México. San Dimas es uno de los distritos mineros mas importantes de México en cuanto a producción de metales preciosos (11 Moz Au, 745

Moz Ag) siendo explotado desde el año 1757 hasta el presente (First Majestic, 2018). El distrito en mención se encuentra en una región que ha sufrido diferentes eventos magmáticos acompañados de eventos de extensión cortical desde el Cretácico Tardío. El conocimiento geológico del distrito se remonta a los trabajos históricos realizados por Henshaw, (1953), Smith y Hall, (1974), Nemeth, (1976), Enríquez y Rivera, (2001b) y Henry et al., (2003), entre otros. Dichos autores definen la geología, cronoestratigrafía y la mineralización del distrito, mencionando varios eventos magmáticos. El primero está constituido por el Batolito Piaxtla de edad eocénica (~52-43 Ma, K/Ar en hornblenda y biotita, Enríquez y Rivera, 2001b; Henry et al., 2003; ~47 Ma, U/Pb en circón, Henry et al., 2003), que representa el basamento de toda la columna estratigráfica. Este cuerpo intrusiona una secuencia volcánica y subvolcánica de composición riolítico–andesítica del Complejo Volcánico Inferior (CVI), dividida en unidades conocidas en el área como Riolita Socavón, Andesita Buelna, Riolita Portal, Andesita Productiva, Andesita Intrusiva, Diorita Arana, estas últimas fechadas por el método K/Ar, reportando edades entre ~36.6 y 40 Ma (Enríquez y Rivera, 2001b), y las formaciones sedimentarias de carácter continental como la Formación Camichín y Formación Las Palmas.

Sobreyaciendo el CVI y en discordancia angular, se describen paquetes lávicos andesíticos con edades de ~24 Ma (K/Ar en plagioclasa, Enríquez y Rivera, 2001b), los cuales son nombrados Andesita Guarisamey. Finalizando la secuencia estratigráfica, se reporta un paquete llamado "*riolita capping*", nombrado así por no tener conexión aparente con la mineralización, con una edad de ~20 Ma (K/Ar en plagioclasa, Enríquez y Rivera, 2001b).

Las unidades anteriores fueron cortadas por diques porfídicos andesíticos (diques Bolaños), y por diques de basalto con piroxeno (diques San Luis), los cuales cortan desde la base hasta el "capping", así como por un dique porfídico dacítico (dique Santa Rita), que intruye desde la base hasta la secuencia sedimentaria de la Formación Las Palmas (Enríquez y Rivera, 2001b). Ninguno de los diques había sido fechado hasta el momento.

En cuanto al conocimiento estructural, el distrito minero San Dimas se encuentra subdividido estructuralmente en 4 bloques por estructuras NNW-SSE: (a) Oeste, (b) Graben Sinaloa, (c) Central y (d) Tayoltita. Horner y Enríquez (1999) muestran la relación entre

estructuras extensionales y transtensionales y las trampas para la generación de depósitos minerales, describiendo 3 eventos principales: 1) fuerzas compresivas E-W a NW-SE con desarrollo de estructuras de E-W y ENE-WSW subverticales relacionados con las partes finales de la Orogenia Larámide, las cuales hospedan los metales (eg. vetas Cedral, Culebra, Candelaria y Castellana). En general son sistemas de vetas emplazadas en todo el CVI y la formación sedimentaria Las Palmas; 2) de fallamiento lateral derecho con componente normal desarrollando estructuras transtensionales NNW-SSE, produciendo los sistemas de fallas Arana y la Peña, sirviendo como canales para el desarrollo los sistemas de vetas Arana, La Patricia y 3) de extensión regional desarrollada durante el Oligoceno y el Mioceno provocando el desarrollo de sistema de fallas de dirección NNW-SSE. Ambos sistemas de vetas se definieron como tipo cuarzo-clorita-adularia a cuarzo-adularia formándose en tres fases generales, llamadas como, temprana, mineralizante y tardía con base al estudio en el Bloque Tayoltita. Para la fase mineralizante, o evento de alta ley, se consideraba un rango de edades entre ~41.0 a 31.9 Ma, en adularia, y en sericita (Henry, 1957; Enríquez y Rivera, 2001b; Enríquez et al., 2018). Basado en estas edades, los autores interpretaban el yacimiento como el resultado de un solo evento hidrotermal desarrollado en un periodo de ~10 Ma, y asociado genéticamente al emplazamiento de cuerpos intrusivos de afinidad intermedia (Andesita Productiva, Andesita Intrusiva, Diorita Arana) debido a que comparten el mismo rango de edades (Enríquez y Rivera, 2001b; Enríquez et al., 2018).

Estudios previos de inclusiones fluidas fueron enfocados solamente en un nivel llamado “nivel de bonanza” para Ag/Au en las estructuras NNW-SSE del BloqueTayoltita (Clarke y Title, 1988; Smith et al.,1982). Los anteriores autores definen este nivel basados en la correlación entre los radios Ag/Au y la salinidad de las inclusiones fluidas, indicando una profundidad entre 400 a 1000 metros desde la paleosuperficie. En general las temperaturas de homogenización de la fase mineralizante en el nivel de bonanza presentan un rango entre 250ºC a 310ºC, con promedio 260ºC (Smith et al., 1982; Clarke and Title, 1988; Conrad et al., 1992; Enríquez and Rivera, 2001; Albinson et al., 2001; Churchill, 1980). Se reportaron puntos de enfriamiento con un rango de variación entre -0.11ºC a -1.5ºC (Smith et al., 1982; Clarke y Title, 1988; Conrad et al., 1992; Enríquez and Rivera, 2001b). Los valores de $\delta^{18}O_{qtz}$ de las fases mineralizantes se reportaron en un rango de 3.9 a 9.5 ‰ y para $\delta^{18}O_{H2O}$ recalculado en un rango -2.9 a 3.7 ‰, lo cual indica un sistema hidrotermal dominado

por aguas meteóricas (Smith et al., 1982; Conrad y Chamberlain, 1992). Los valores reportados de espectrometría de gases indican fases bifásicas en las cuales el agua es superior al gas, a su vez el gas predominante es CO_2 en comparación con CO, y trazas de H_2, CH_4, N_2, C_2H_6, H_2S, C_3H_8, SO_2 and NO (Smith et al., 1982).

La contribución científica principal de este estudio doctoral se enfoca en el entendimiento de la evolución geológica y tectónica durante el desarrollo del arco laramídico hasta los inicios de la apertura del Golfo de California y su asociación genética y fisicoquímica para el desarrollo de múltiples eventos mineralizantes sobreimpuestos en la generación de yacimientos de clase mundial en la Sierra Madre Occidental.

1.2 Objetivos

El objetivo principal de este estudio doctoral es la actualización del modelo geológico del distrito minero de San Dimas (SD). Esto implica determinar las condiciones geológicas, temporalidad y geoquímicas necesarias para la formación de un yacimiento de clase mundial dentro de la evolución geodinámica regional de la SMO.

Para lograr el objetivo se combinaron los siguientes procedimientos. 1) caracterización petrológica, petrográfica y geocronológica detallada de la columna estratigráfica de San Dimas; 2) caracterización petrológica y petrográficamente de los diferentes sistemas de vetas del distrito minero San Dimas; 3) se obtuvieron nuevos datos geocronológicos y se reinterpretaron las edades existentes de los eventos mineralizantes del área de estudio; 4) se desarrolló una caracterización fisicoquímica de los diferentes fluidos hidrotermales y sus relaciones con la roca encajonante; 5) se propuso un nuevo modelo metalogenético del área.

1.3 Procedimientos analíticos

Con el objeto de obtener datos analíticos que permitan evaluar los objetivos propuestos, este estudio doctoral integra diferentes técnicas analíticas que permiten generar nuevas

interpretaciones sobre los eventos que llevaron al desarrollo de múltiples mineralizaciones en el distrito de SD en diferentes contextos tectónicos y magmáticos.

Petrografía

La petrografía de roca caja, composición mineral y texturas fue documentada a través de análisis petrográfico y microscopía electrónica. Las láminas delgadas pulidas se examinaron con el microscopio óptico Olympus® BX-50. Las fases minerales fueron identificadas usando el microscopio electrónico Hitachi TM-1000 con microscopía de microanálisis EDS en el Laboratorio de Geofluidos del Centro de Geociencias de la UNAM, Campus Juriquilla, Querétaro, México (CGEO).

Química mineral

La composición química de los minerales (Au, Ag, sulfosales) fue determinada con el Microscopio Electrónico con Analizador (EMPA) JOEL JXA 8900R en el Laboratorio Universitario de Petrología de la UNAM, Campus Ciudad de México, usando estándares sintéticos y naturales. Los metales asociados a la mineralización fueron analizados con un haz de corriente de 20 nA y una aceleración de voltaje de 20 keV. Todos los análisis fueron llevados a cabo por medio de "targeting" de búsqueda basados en las relaciones texturales con otros minerales.

Geocronología U/Pb

Treinta y dos muestras de roca con control estratigráfico fueron seleccionadas para fechamientos U/Pb. Las muestras fueron trituradas y tamizadas (Mallas 200-50). Los minerales pesados fueron concentrados usando técnicas convencionales (batea y magnetómetro isodinámico Frantz). Los cristales de circón fueron seleccionados manualmente (hand-picked) con el uso de un microscopio binocular y posteriormente montados en un EpoFix® con anillo de plástico de diámetro 2.5 cm, posteriormente fueron pulidos. Los puntos de ablación fueron seleccionados basados en las imágenes de

catodoluminiscencia con el fin de identificar los centros y bordes de crecimiento del circón. Cada ablación se desarrollo con el sistema de ablación laser Resonetics RESOlution® LPXPro (193 nm, ArF excimer), acoplado a Thermo® Scientific iCAP® Qc quadrupole ICP-MS en el Laboratorio de Estudios Isotópicos (LEI) en el CGEO. Para cada circón, la ablación consistió en la adquisición de 15 s señales del fondo (gas blanco), 30 s de ablación, y 15 s de estabilización dejando así que la señal alcance la línea base de nuevo. El diámetro de cada spot fue de 33 μm, usando una velocidad de 6 J/cm^2 con una repetición de 5 Hz. Se registraron todos los isótopos requeridos para obtener la edad U/Pb (^{206}Pb, ^{207}Pb, ^{208}Pb, ^{232}Th y ^{238}U), adicional este método (LA-ICP-MS) permite detectar otros elementos mayores, trazas y tierras raras (REE) simultáneamente. Estos datos fueron relevantes para identificar los diferentes pulsos magmáticos en términos de la hidratación y fertilidad. La calibración de ICP-MS se realizó siguiendo los procedimientos de Solari et al., (2010) y Ortega-Obregón et al., (2014). La corrección de los radios isotópicos y el error por edad fueron calculados con Iolite (Paton et al., 2011) usando la data de reducción VizualAge (Petrus y Kamber, 2012). La composición química de cada circón fue obtenida basado en los estándares de vidrio NIST. Se uso el circón 91500 (Wiedenbeck et al, 1995) como referencia principal para los análisis de U/Pb.

Para cada muestra se analizaron ~35 circones, y las edades fueron reportados en base a la edad promedio de cristalización utilizando la metodología propuesta por Ludwing (2008). Los análisis por fuera de 2σ fueron descartados. Porcentajes con discordancias mayores al 20 % no fueron considerados. Para rocas volcánicas, la edad reportada fue la edad de la población de circones más jóvenes. En rocas ígneas los circones más antiguos se interpretaron como herencias del basamento. Para rocas sedimentarias se analizaron alrededor de ~100 circones. La edad máxima de sedimentación fue asociada a los circones más jóvenes. Para esto se analizaron diferentes poblaciones de circones y se reportaron haciendo uso de histogramas y diagramas de densidad de probabilidad.

Termocronología trazas de fisión en apatitos y titanitas

El fechamiento de trazas de fisión (TF) en apatitos fue desarrollada en el Laboratorio de Estudios Isotópicos (LEI) del CGEO usando la técnica LA-ICP-MS (Hasebe et al., 2004; Donelick et al., 2005). Los detalles de la metodología se describen en Abdullin et al., (2018).

Se usaron los cristales de Durango F-apatito con una edad de 31.4 ± 0.5 Ma (Hurford, 2019) como equivalente de calibración (Hasebe et al., 2004; Donelick et al., 2005; Vermeesch, 2017), así como también las medidas de Cl en un apatito desconocido (0.43 ± 0.03wt% de Cl in Durango, Goldoff et al., 2012). Las edades de TFA para cada apatito con 1σ fueron calculadas usando IsoplotR (Verneesch, 2017, 2018). La edad promedio de TFA y los diferentes picos de edad fueron obtenidas usando RadialPlotter (Verneesch, 2009).

*En el caso de las titanitas, s*e separaron 200 cristales que se montaron en un EpoFix® con anillo de plástico de diámetro 2.5 cm. Los EpoFix fueron pulidos con papel-arena SiC P1500 y P2500 hasta exponer las superficies internas de los cristales (4π), posterior fueron pulidas con 3, 1, 0.3 y 0.1μm de aluminio en suspensión. Las titanitas pulidas fueron grabadas con 1HF:2HNO_3: 3HCL:6H2O a temperatura ambiente (24ºC) por 16 minutos (Kohn et al., 2019). El estándar de titanita Fish Canyon Tuff (FCT) fue también grabado por 22 minutos. El conteo de trazas de fisión fue desarrollado usando el microscopio Carl Zeiss AxioScopeA1 acoplado con cámara digital y objetivos "secos". Se uso la técnica LA-ICP-MS con un haz de rayo laser 60 μm, se ablacionó exactamente en las mismas áreas que fueron usadas para determinar los valores de ρ_s (densidad de trazas). El estándar de titanita (FCT) de edad 28.4 ± 0.1 Ma (Schmitz y Bowring, 2001) fue usado para la calibración equivalente (Hasbe et al., 2004; Donelick et al., 2005; Vermeesch, 2017). Los resultados crudos fueron reducidos con Iolite 3.4 (Paton et al., 2011). Se uso NIST612 para los resultados de medidas isotópicas (Pearce et al., 1997) y fueron normalizados usando 29Si como estándar interno, tomando un promedio de SiO_2 de 30 ± 1 wt% para todas las titanitas analizadas. Las edades de TF en titanitas fueron calculados con IsoplotR (Vermeesch, 2017, 2018). Se usaron los protocolos internos de LA-CIP-MS del LEI.

Geocronología $^{40}Ar/^{39}Ar$

Seis muestras de adularia con control geológico asociadas a diferentes eventos mineralizantes en SD fueron seleccionadas para ser fechadas por $^{40}Ar/^{39}Ar$ en base a calentamiento por pasos utilizando un láser. La preparación de las muestras se desarrollo en el CGEO. Las muestras fueron trituradas y tamizadas a un tamaño de 420-840μm y posteriormente lavadas

con agua desionizada, acetona al 98%, y secadas en horno durante una noche a 50ºC. Los cristales de adularia fueron seleccionados manualmente en un microscopio binocular.

Las muestras fueron irradiadas en dos diferentes paquetes (JUR02, JUR03) en la posición 8C en el reactor de investigación U-enriquecido de la Universidad de McMaster en Hamilton, Ontario, Canadá. Durante la irradiación, las muestras y el monitor de flujo de neutrones fueron cubiertos con un haz de Cd para bloquear neutrones térmicos. Se usó el estándar de sanidino, Fish Canyon tuff (FCT-2 (28.198 ± 0.044 Ma, Kuiper et al., 2008) como monitor. Las muestras fueron analizadas en el Laboratorio Interinstitucional de Geocronología de Argón (LIGAr), instalado en el CGEO, usando el láser para extracción de gases Coherent Innova 200-20 Ar-ion, una línea de gas automatizado para limpieza, dos captadores SAES GP-50, y un espectrómetro multicolector de masas para gases nobles. El haz de iones de isótopos de Ar fue simultáneamente medido por cuatro colectores Faraday con 10^{12} Ω amplificadores (m/z 36 a 39), y un colector con 10^{11} Ω amplificadores (m/z 40). Cada corrida consistió en 20 ciclos de 10s, con una integración de tiempo de 1s, precedido de 30 medidas base con integración de tiempo de 1s. Se intersectaron medidas de aire repetidamente con muestras desconocidas para corregir la discriminación por masas y la contaminación de Ar atmosférico, usando un ratio de $^{40}Ar/^{36}Ar$ de 295.5. Cada paso y medida de aire fue precedido de una medida de blanco.

Para la reducción de datos, se usó el software NGX-Red 1.0® y AgeCalc 1.9® desarrollado por el CICESE, Ensenada, México. Encima de la sustracción del blanco, los datos isotópicos de Ar fueron corregidos por discriminación por masas, y para calcio, potasio y cloro se realizaron reacciones de interferencia. Los parámetros usados para corregir las reacciones de neutrones inducidos fueron: $(^{39}Ar/^{37}Ar)_{Ca} = 6.50 \times 10^{-4}$; $(^{36}Ar/^{37}Ar)^{Ca} = 2.55 \times 10^{-4}$; $(^{40}Ar/^{39}Ar)^{K} = 0$. La masa 36 también fue corregida para cloro derivado ^{36}Ar [$^{35}Cl(n, \gamma)$ $^{36}Cl \rightarrow {}^{36}Ar + \beta-$ with $t^{1/2}$ 3.01 × 105 a]. Los isotopos de ^{37}Ar y ^{39} Ar fueron corregidos por decaimiento radioactivo. Se uso el decaimiento constante recomendado por Steiger y Jäger, (1977) en todos los cálculos, adicional a cálculos de straight-line presentados por York et al., (2004). Todos los errores fueron reportados a 1 σ estándar, los errores, mesetas y edades de isócrona incluyendo la incertidumbre en el parámetro J fueron integrados. Las edades de integración fueron calculadas adicionando todas las fracciones del experimento en

calentamiento por pasos. Las edades de meseta (plateaus) fueron seleccionadas en la base de los valores MSWD con probabilidad de corte 0.005 (Wendt y Carl, 1991), las edades de meseta fueron calculadas como peso promedio entre mínimo de tres consecutivas fracciones que representaran el 50% o mas de perdida de ^{39}Ar. Los errores del peso promedio y regresiones que tuvieran valores de MSWD mayores que 0.05 de probabilidad del valor de corte fueron multiplicados por 1 σ error por la raíz cuadrada de MSWD. Los errores también fueron reportados al 95% en intervalo de confianza, calculados y multiplicados por 1 σ error por su apropiado Valor de t Student.

Petrografia de inclusiones fluidas y microtermometría

Los estudios de inclusiones fluidas (IF) incluyeron petrografía detallada para la determinación de las diferentes fases, formas y tamaños de las inclusiones. Se uso el Microscopio óptico Olympus® BX-50 con Qimaging Micropublisher 5 Mp equipado con cámara digital a Peltier-cooled CCD para la caracterización de las inclusiones en láminas gruesas pulidas. Para la obtención de temperaturas mínimas de atrapamiento o temperaturas de homogenización y temperaturas de congelamiento se utilizó el microtermómetro platina Linkam THMSG-600 (2) acoplado a microscopio Olympus BX-51. Para la determinación de temperaturas máximas de atrapamiento por población de IF se utilizó el método de decrepitación térmica con el equipo Decriptrómetro BGS Modelo 04. Los estudios de inclusiones fluidas fueron llevados a cabo en el Laboratorio de Geofluidos del CGEO.

Isotopía estable

Diez muestras de cuarzo de ~15g cada una fueron seleccionadas para los estudios isotópicos de cada evento mineralizante. Las muestras fueron trituradas y cribadas en mallas 45 y 60. Las fracciones no magnéticas fueron separadas con el magneto isodinámico Frantz en el Laboratorio de separación de minerales del CGEO. Las muestras de cuarzo fueron separadas manualmente con microscopio binocular con el objeto de seleccionar los mejores cristales de cuarzo (sin impurezas). Finalmente, las muestras fueron lavadas con HCL, agua regia y acetona al 98% en 5 ciclos de 5 minutos cada una en una lavadora ultrasónica.

Las muestras fueron decrepitadas térmicamente desde 0 a 900ºC con una rampa de calentamiento de 5ºC por minuto en la línea de vacío "Ultra Vacuum Glass Line" (10-9 – 10-10 mbar), se siguió el procedimiento de Montoya et al., (en preparación) en el Laboratorio de Isotopía Estable, Departamento de Geología, UNAM campus Ciudad de México. Se separaron 3 poblaciones de agua de inclusiones fluidas 100ºC - 300ºC, 300ºC – 545ºC, 545ºC – 900ºC por muestra. Cada muestra de agua fue guardada separadamente en tubos de cuarzo en ultra vacío. Los isótopos de δ^2H y $\delta^{18}O$ fueron medidos en el equipo Analizador Isotópico de Inyección Automatizada DLT -100 en el Laboratorio de Isotopía Estable, Departamento de Geología, UNAM campus Ciudad de México. Los resultados fueron reportados por mil relativo a los estándares V-SMOW y VSLAP (Coplen, 1988 y Coplen et al., 2006) con una precisión de ± 2 ‰ for δ^2H and ± 0.2 ‰ for $\delta^{18}O$.

Isotopía de gases nobles

Se seleccionaron 10 muestras de cuarzo de vetas para analizar los volátiles contenidos en las inclusiones fluidas. La preparación de las muestras se realizó siguiendo el procedimiento de Di Piazza et al., (2015) y Rizzo et al., (2015) desarrollado por el Istituto Nazionale di Geofisica e Vulcanologia, Sezione di Palermo (INGV-Palermo). Los gases atrapados en las IF en cuarzo fueron obtenidos por medio de trituración a 200ºbar en un sistema de vacío siguiendo los procedimientos de Kurz, (1986) y Hilton et al., (1993, 2002). Los gases asociados a la fragmentación mecánica fueron removidos de la línea de vacío. Los isótopos de Helio (^3He and ^4He) y Neón (^{20}Ne, ^{21}Ne and ^{22}Ne) fueron medidos separadamente en dos diferentes tubos en el espectrómetro de masas (Helix SFT-Thermo). Los valores de $^3He/^4He$ fueron reportados en R/Ra (donde Ra es el valor del radio del aire de $^3He/^4He$, el cual es igual a $1.39 \bullet 10^{-6}$). La incertidumbre analítica del radio isotópico de He es entre 1.5 y 15%. Los isotópos de Ar (^{36}Ar, ^{38}Ar and ^{40}Ar) fueron analizados con un espectrometro de masas multicolector (GVI Argus) con una incertidumbre analítica menor 0.4%. La incertidumbre en la determinación del contenido elemental He, Ne y Ar fue menor al 5%. Lo valores de los blancos para He, Ne y Ar fueron <10–14, <10–15 y <10–13 mol, respectivamente.

Capítulo 2: **New insights into the geology and tectonics of the San Dimas mining district, Sierra Madre Occidental, Mexico**

Ore Geology Reviews 105 (2019) 273–294

Contents lists available at ScienceDirect

Ore Geology Reviews

journal homepage: www.elsevier.com/locate/oregeorev

New insights into the geology and tectonics of the San Dimas mining district, Sierra Madre Occidental, Mexico

Paula Montoya-Lopera[a], Luca Ferrari[a,*], Gilles Levresse[a], Fanis Abdullin[b], Luis Mata[c]

[a] Centro de Geociencias, Universidad Nacional Autónoma de México, Campus Juriquilla, 76230 Querétaro, Qro., Mexico
[b] CONACyT–Centro de Geociencias, Universidad Nacional Autónoma de México, Campus Juriquilla, 76230 Querétaro, Qro., Mexico
[c] First Majestic Silver Corp., Tayoltita, Dgo., Mexico

ARTICLE INFO

Keywords:
Sierra Madre Occidental
San Dimas mining district
Epithermal deposit
Geochronology
Volcanic stratigraphy

ABSTRACT

The San Dimas district is a world-class silver-gold low-sulfidation epithermal deposit located in the central part of the Sierra Madre Occidental of Mexico, within the eastern part of the Gulf of California extensional province. Previous works assumed a single period of mineralization between ~38.5 and 31.9 Ma, which is at odds with the existence of vein systems with two different orientations and Ag/Au ratios. We present a re-evaluation of this district based on new zircon U/Pb and apatite fission-track ages as well as petrographic and field observations of mineralization styles. Our study also includes two new prospective areas of Causita and Mala Noche located to the south of the main district.

Within the Lower Volcanic Complex, we identify a Late Cretaceous volcanic succession (~77 to 69 Ma) correlative with the Tarahumara formation from southern Sonora and coeval with the San Ignacio batholith exposed to the west. This volcanic succession hosts Au-rich mineralized sub-volcanic felsic bodies yielding slightly younger ages and is covered by Paleocene intermediate lavas with hypabyssal intrusions with ages around 48 Ma. A voluminous intrusive suite (Piaxtla batholith and associated dike swarms) was emplaced in the region between ~49 and 44 Ma. Early extensional basins were filled by a continental sedimentary sequence (Palmas formation), which yielded U/Pb age peaks at 66 and 56 Ma from detrital zircons and a maximum depositional age of ~43 Ma. The last magmatic activity, as in the rest of the Sierra Madre Occidental, consists of silicic ignimbrites and less basaltic lava flows clustered in two pulses of ~31.5–29 Ma and 24–20 Ma.

NNW–SSE extensional fault systems expose the mineralization and tilted all the succession prior to the emplacement of a ~24 Ma ignimbrite package. This late Oligocene extension, associated to the early stage of the Gulf of California rift, is confirmed by apatite fission-track dating of samples from the Piaxtla batholith, which consistently indicate an episode of cooling at 25–23 Ma followed by a second episode at ~12.5 Ma. Our absolute ages and geologic mapping allow to infer that an older, WSW–ENE trending normal fault system with up to 1 km of displacement must exist between the San Dimas district and the Causita area to the south. This fault system, currently buried beneath Oligocene–Miocene ignimbrites, may have controlled the intrusion of the Piaxtla batholith and played a crucial role in the preservation of large vein systems of San Dimas in a tectonic depression setting.

The main epithermal mineralization is associated with two kinds of structures: Ag/Au veins with WSW–ENE to E–W orientation and Au/Ag veins with NNW–SSE to N–S orientation. The dominant Ag/Au veins slightly postdate the Piaxtla intrusive suite and partly recycled older felsic intrusion with porphyry mineralization. The NNW–SSE to N–S Au/Ag veins are most probably associated with the Oligocene silicic volcanism.

1. Introduction

A proper understanding of the formation and preservation of mineral deposits in continental settings implies assessing the dynamic interaction among magmatic, tectonic, erosional, and depositional processes. This approach is particularly important in the case of western Mexico, which has undergone a complex tectono-magmatic history since the Cretaceous (Ferrari et al., 2017). In this region, the Sierra Madre Occidental (SMO) geologic province hosts numerous important porphyry and epithermal deposits mostly occurring in its western side,

* Corresponding author.
E-mail address: luca@unam.mx (L. Ferrari).

https://doi.org/10.1016/j.oregeorev.2018.12.020
Received 13 August 2018; Received in revised form 4 December 2018; Accepted 28 December 2018
Available online 02 January 2019
0169-1368/

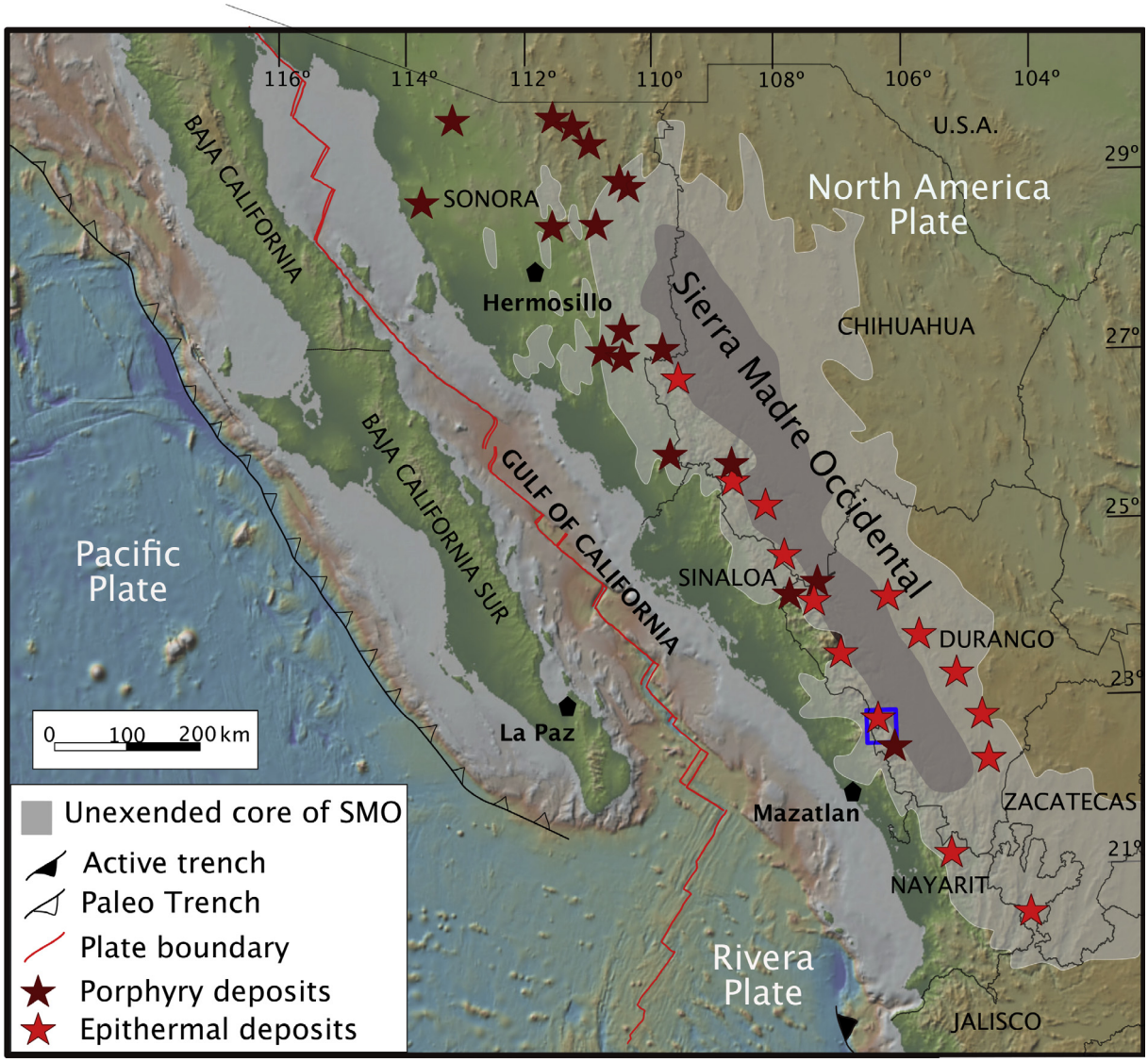

Fig. 1. Geodynamic context of western Mexico and main porphyry and epithermal deposits of the Sierra Madre Occidental volcanic province. The blue rectangle represents the study area. (For interpretation of the references to color in this figure legend, the reader is referred to the web version of this article.)

a portion that represents the eastern rifted margin of the Gulf of California (Fig. 1). Several reviews and classifications of the SMO mineralization have been proposed in past decades. The initial attempts relied on the concept of metallogenic provinces or belts, where mineralization is essentially tied to a geographic domain and produced by the interaction of arc magmatism with a certain type of basement terrane (e.g. Damon et al., 1981, 1983; Campa and Coney, 1983; Salas, 1994). More recent reviews (e.g. Staude and Barton, 2001; Camprubí, 2013; Camprubí and Albinson, 2007) placed each mineralization type into a specific magmatic-tectonic episode since Mesozoic, implicitly recognizing the dynamic nature of this plate margin and the possibility of superposition of mineralization events. Several studies have also been devoted to classifying the SMO epithermal deposits based on fluid geochemistry and physical parameters (e.g. Smith et al., 1982; Clarke and Titley, 1988; Albinson et al., 2001; Camprubí and Albinson, 2007). However, reviews and analytical studies are significantly limited by the fact that most parts of the SMO lack a good geochronologic control and a detailed geologic description of veins systems, which may jeopardize a correct interpretation of a mineral deposit development.

The San Dimas mining district, centered at the town of Tayoltita, is a world-class silver-gold epithermal deposit and possibly the archetype of such deposits in the SMO (Locke, 1918; Davidson, 1932; Henshaw, 1953; Clarke, 1986). Mined since the 18th century, the San Dimas district contains more than 200 discovered Ag-Au veins, located in five blocks separated by major NNW-striking normal faults. Despite being a world reference for low-sulfidation Ag-Au epithermal veins, the mineralization model for San Dimas has not been improved significantly since the middle of the past century. The current stratigraphic overview is based on field and mine observations, supported by petrographic and geochronologic studies (Nemeth, 1976; Henry and Fredrikson, 1987; Enriquez and Rivera, 2001a,b; Henry et al., 2003). The rocks hosting the mineralization are not dated and the Ag-Au veins have been traditionally considered to be developed in a single mineralization episode between ~41 and ~31 Ma (Enríquez and Rivera, 2001b; Enriquez et al., 2018). However, most these ages, obtained by the K–Ar method, are not always reliable given the widespread hydrothermal alteration of the district. The difference in vein orientation with variable Ag/Au ratio through the district are also at odd with the idea of a single mineralization episode.

In this study, we present a revision of the geology and stratigraphy of the San Dimas district as well as of adjacent areas based on fieldwork at surface and in mine interior, supported by a detailed petrographic study and U/Pb and apatite fission-track ages of the whole geologic column. This provides a robust geologic and geochronologic context

towards a better understanding of the mineralization events that will be described in detail in a forthcoming paper (Montoya-Lopera et al., submitted for publication).

2. Previous studies

2.1. Regional geology and tectonic setting

As a physiographic province, the SMO comprises a high plateau with an average elevation exceeding 2000 m above sea level that cover an area ~1200 km long and ~200 to 400 km wide extending from the Mexico–US border approximately to Latitude 21° N, where it intersects the Trans Mexican Volcanic Belt (Fig. 1). The western part of the SMO high plateau is cut by normal faults systems that are part of the Gulf of California rift and where most ore deposits are exposed. As an igneous province, the SMO includes Late Cretaceous to early Miocene rocks formed during two main periods of continental magmatic activity (McDowell and Keizer, 1977; Ferrari et al., 2017). The first period, concurrent with the Laramide orogeny, produced a dominantly intermediate intrusive suite and its volcanic counterpart, associated with a normal supra-subduction magmatic arc active between ~100 and 50 Ma (Gastil, 1975; McDowell et al., 2001; Henry et al., 2003; Ortega-Gutiérrez et al., 2014). These rocks, traditionally named Lover Volcanic Complex (LVC) (McDowell and Keizer, 1977), formed the Sonora, Sinaloa, and the Jalisco batholiths, as well as the Late Cretaceous to Paleocene volcanic succession of the Tarahumara Formation in Sonora (Wilson and Rocha, 1949; McDowell et al., 2001), and equivalent rocks in the Jalisco Block (Ferrari and Rosas-Elguera, 2000; Valencia et al., 2013) (Fig. 1). Volcanic successions of this age have been inferred in Sinaloa and Durango, but no radiometric ages have been provided so far.

After a transitional period that lasted until the late Eocene (Ferrari et al., 2017), volcanism became dominated by rhyolitic ignimbrites with less basaltic lavas, building one of the largest silicic volcanic provinces on Earth (Bryan and Ferrari, 2013). Defined as the Upper Volcanic Supergroup (UVS) (McDowell and Keizer, 1977), these rocks were emplaced mostly in two episodes of ignimbrite flare up at ~35 to 29 Ma along the entire province and at ~24 to 20 Ma in its southern part (Ferrari et al., 2002, 2007; McDowell and McIntosh, 2012). Mafic lavas with both asthenosphere and mantle lithosphere affinity are found interspersed within the ignimbrite successions, often associated with normal faulting (Ferrari et al., 2017). Extensional basins and associated continental sedimentary deposits formed between ~27 and ~15 Ma in a NNW-trending belt along the western half of the SMO, spanning the western part of Sonora (McDowell et al., 1997; Nourse et al., 1994; Gans, 1997; González León et al., 2000; Wong et al., 2010; Murray et al., 2013) and most of Sinaloa and Nayarit (Ferrari et al., 2013) (Fig. 1). The temporal and spatial association of the silicic (or felsic) to bimodal magmatism of the UVS with crustal extension supports the idea that these processes represent the beginning of the rifting process that led to the formation of the Gulf of California (Bryan and Ferrari, 2013; Ferrari et al., 2013, 2017).

The San Dimas mining district lies within the central part of the SMO, near the Sinaloa–Durango state border (Fig. 1). The geology of this part of the SMO is summarized in Fig. 2 and is briefly described in the following based on recent regional works presented in Ferrari et al. (2013, 2017). The basement predating the continental batholiths is exposed in the western part of the region in the state of Sinaloa and consists of strongly folded metasedimentary and meta-volcanic rocks, deformed granitoids, phyllite sandstones, quartzites, and quartz-biotite-muscovite schists with ages spanning from Jurassic to Early Cretaceous (Henry and Fredrikson, 1987; Henry et al., 2003). These rocks are locally covered by Albian–Cenomanian limestones north of Mazatlán (Bonneau, 1970). The LVC consists of granite, granodiorite and diorite intrusive rocks exposed in the coastal areas and along the lower course of the main rivers, with ages progressively younger to the east. They form two main plutonic complexes: the San Ignacio batholith exposed towards the coast with mostly Late Cretaceous to early Paleocene ages; and, the Piaxtla batholith, cropping out towards the east along the Piaxtla and Presidio rivers with mostly Eocene ages (Fig. 2). The plutonic rocks were extensively studied by Henry (1975), Henry et al. (2003), who published many K–Ar and four U/Pb ages. Volcanic rocks consisting dominantly of ignimbrites with less lava flows are intruded by the Piaxtla batholith. Andesite lava flows cover these successions and the San Ignacio batholith and are sometimes intruded by the Eocene plutonic rocks. None of these volcanic successions have been dated so far.

Continental conglomerates and sandstones fill intermontane basins and separate the LVC from the UVS. The latter consists of two successions of silicic ignimbrites with minor basaltic lavas and some rhyolitic domes that covers the eastern part of the region. The first ignimbrite succession, mostly exposed towards the east in the Durango state, has been dated at ~32 to 30 Ma (McDowell and Keizer, 1977; McDowell and McIntosh, 2012; Ferrari et al., 2013). The second ignimbrite package, defined as the El Salto-Espinazo del Diablo succession by McDowell and Keizer (1977), yielded Ar–Ar ages of 24–23.5 Ma (McDowell and McIntosh, 2012) and is only exposed in the western part of the region. A NNW-trending extensional fault system, named Pueblo Nuevo–Tayoltita (Ferrari et al., 2013), separates the undeformed plateau of the SMO to the east, mostly in the Durango state, from the faulted and highly incised terrain to the west, in the Sinaloa state (Fig. 2). In this 90-km-wide, coast-parallel, extensional belt the El Salto-Espinazo del Diablo ignimbrite succession filled pre-existing valleys and lies in angular unconformity (20–30°) over the ~32 to 30 Ma ignimbrite successions, which indicate that a first extensional phase of deformation took place in the late Oligocene (Ferrari et al., 2013). Large volume rhyolitic domes with ages of ~29 to 28 Ma are aligned along the Pueblo Nuevo–Tayoltita fault system (Fig. 2). This coast-parallel extensional belt is characterized by several late Oligocene to middle Miocene graben, filled with conglomerates and some rhyolitic domes and basaltic lava flows (Ferrari et al., 2013).

2.2. Local geology

Previous knowledge on the geology and geochronology of the San Dimas district is summarized in the following. The LVC has been traditionally divided into informal geologic units primarily based on field observations. From base to top, these are the “Socavón rhyolite”, the “Buelna andesite”, and the “Portal rhyolite”, defined as a sequence of interlayered tuffs and lesser lava flows of felsic to intermediate composition (Locke, 1918; Davidson, 1932; Henshaw, 1953). These rocks are overlain unconformably by a succession of andesitic lavas named “Productive andesite” which is intruded by intermediate rocks called the “Arana intrusive andesite” and the “Arana intrusive diorite” (Henshaw, 1953) as well as by a felsic suite consisting of the “Piaxtla Granite” (partly mapped as Candelero granodiorite in Henry et al., 2003) and “Santa Lucia”, “Bolaños”, and “Santa Rita” dikes. Enríquez and Rivera (2001b) reported K–Ar ages obtained in a commercial laboratory for these intrusions. The intermediate intrusions yielded feldspar K–Ar ages ranging from 39.9 ± 1 to 36.6 ± 1 Ma, which are likely the result of partial resetting given that these intrusions lie near the core of the mineralized area. Henry et al. (2003) obtained a U/Pb age of 47.8 ± 1.0 Ma and hornblende and biotite K–Ar ages for six samples of the intrusive suite along the Piaxtla valley ranging from 51.2 ± 1.6 to 43.9 ± 0.3 Ma. In the Tayoltita area, biotite concentrates yielded K–Ar ages of 45.9 ± 1.2 and 45.1 ± 1.1 Ma (Enríquez and Rivera, 2001b), and an Ar–Ar age of 46.3 ± 0.1 Ma (Enriquez et al., 2018).

The LVC is separated from the younger rocks by a major erosional unconformity, marked by the so called “Las Palmas” and “Camichin” units made of conglomerate and red beds (Davidson, 1932; Henshaw, 1953). The overlying UVS, consists of a voluminous package of

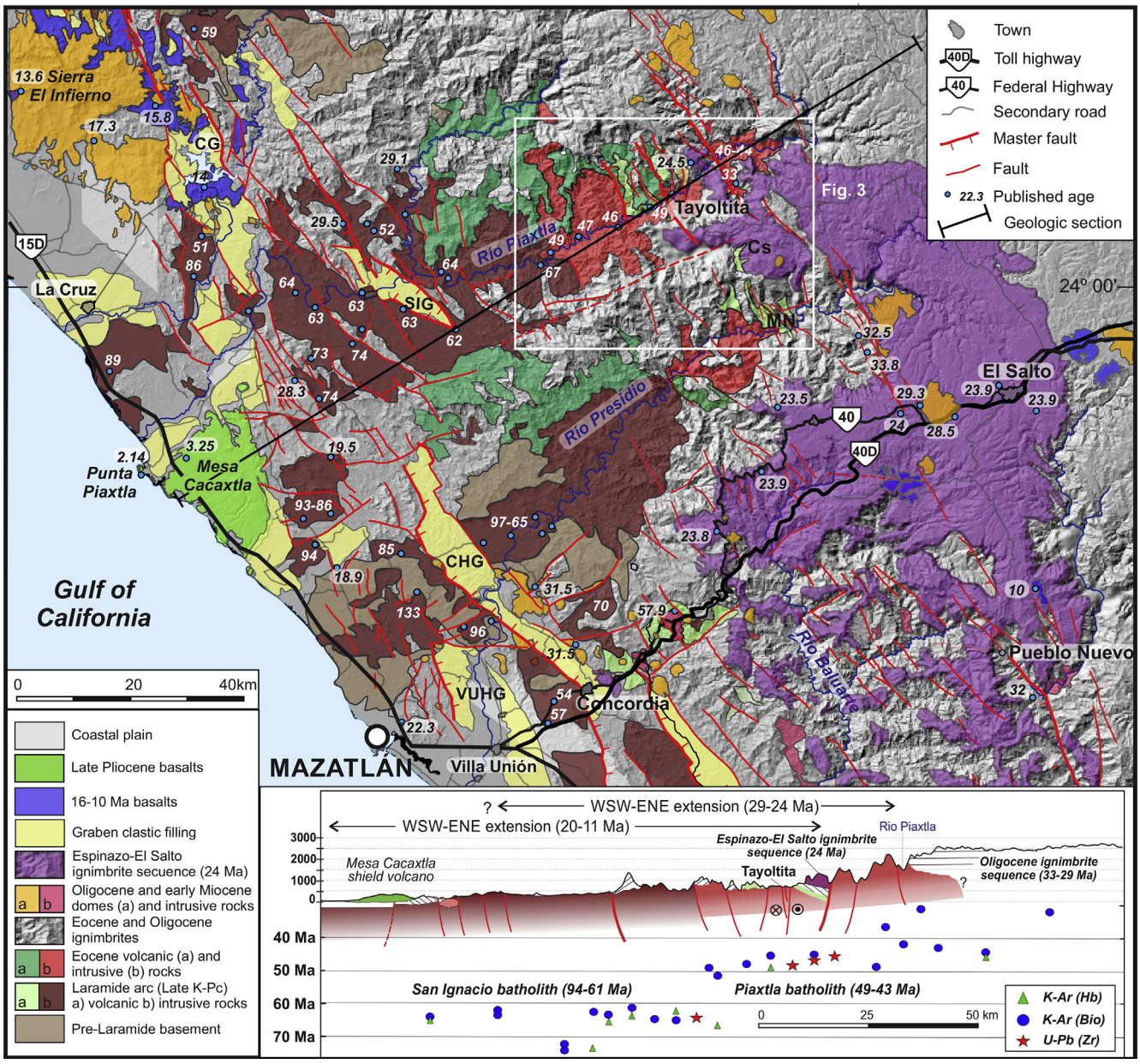

Fig. 2. Regional geologic map of central Sierra Madre Occidental showing the main extensional structures and published ages (modified from Henry and Fredrikson, 1987, and Ferrari et al., 2013). SIG—San Ignacio graben; CG—Conitaca graben; CHG – Concordia half-graben; VUHG – Villa Unión half-graben; MN—Mala Noche; Cs—Causita. The geologic section includes the ages of intrusive rocks in the Piaxtla valley (projected along the trace of the section) to show the sharp variation between the San Ignacio y Piaxtla batholiths.

ignimbrites, breccias, and less lava flows (Henshaw, 1953). Enríquez and Rivera (2001b) obtained a K–Ar age of 24.5 ± 0.9 Ma for the distinctive "Guarisamey andesite", located at the base of the sequence, and an age of 20.3 ± 0.8 Ma for the upper part of the ignimbrite succession.

The structural context has been addressed by Ballard (1980), who investigated the structural control of mineralization in the Tayoltita mine, and by Horner and Enriquez (1999), who studied the structural geology and tectonic control for the whole district. The most prominent structures are major north–northwest–trending normal faults with opposite vergence that divide the district into five blocks tilted to the ENE or WSW (Enriquez and Rivera, 2001a) (Fig. 3). All the major faults exhibit northeast–southwest extension, and dips that vary from nearly vertical to approximately 55° (Horner and Enriquez, 1999). E–W to WSW–ENE striking fractures, perpendicular to the major normal faults, are filled by quartz veins, dacite porphyry dikes, and pebble dikes, all cut by rhyolite porphyry dikes which occupy N–S to NNW–SSE trending fissures (Smith et al., 1982). Horner and Enriquez (1999) grouped the development of major faults, vein and dikes into three deformational events: 1) event D1, represented by tension gashes with E–W to ENE–WSW orientation with a slight right-lateral offset, developed in the late Eocene. These structures host the first hydrothermal vein systems. 2) Event D2, produced N–S-trending right-lateral strike-slip to transtensional faults due to a rotation of the maximum horizontal principal stress to a ~NE–SW position. In this stage, inferred to have occurred in the early Oligocene, a second set of hydrothermal veins developed. 3) Event D3 produced the major block faulting that affected the entire district along NNW–SSE-striking normal faults, which in some cases reactivated the former strike-slip faults during the late Oligocene–Miocene period. These faults hosted bimodal dikes, which are part of the UVS.

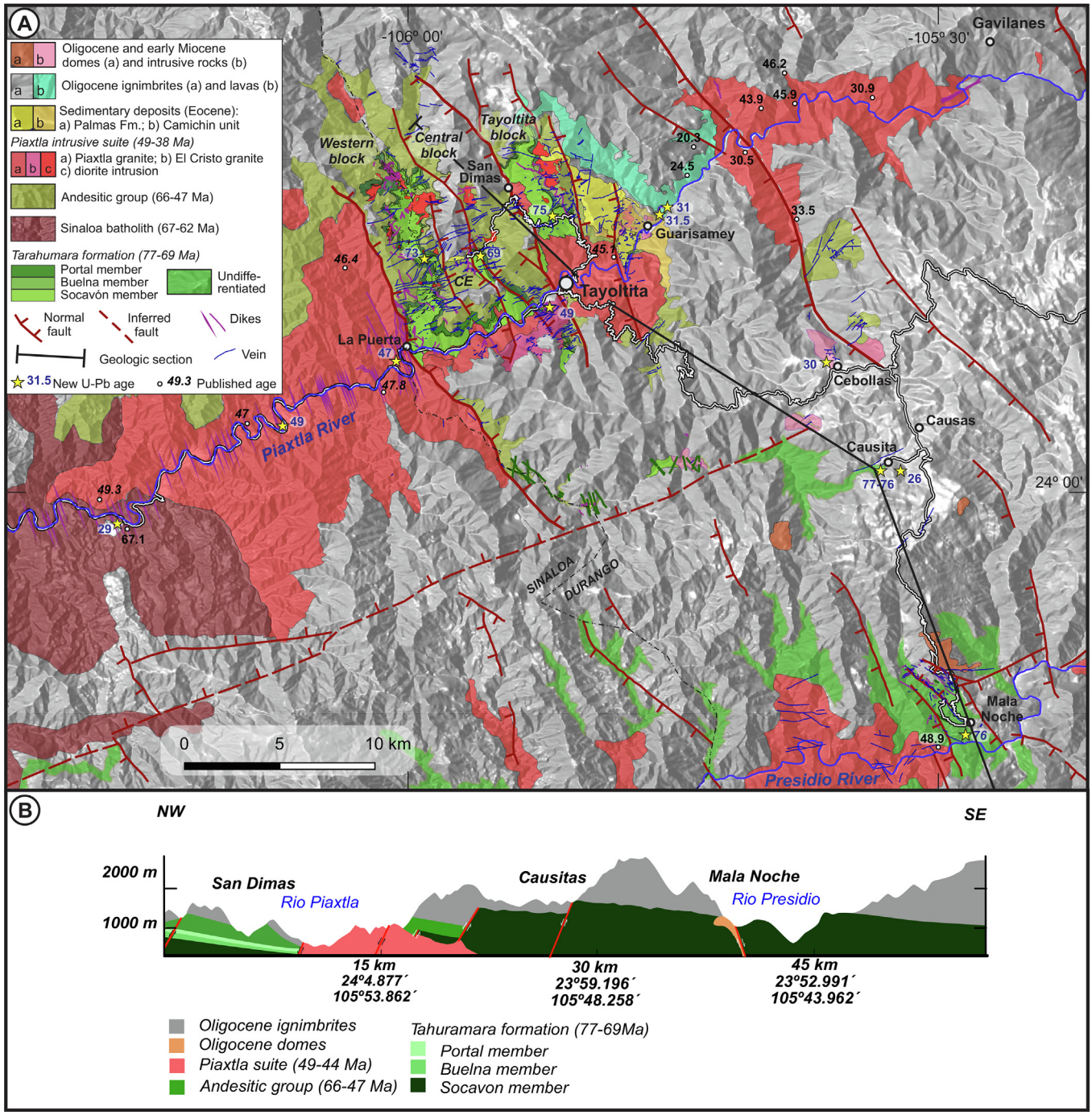

Fig. 3. A) Geologic map of San Dimas mining district and Causita-Mala Noche areas, with location of published and new ages. B) Geologic section.

3. Analytical techniques

3.1. Geologic mapping and sampling

A revision of the geologic cartography was carried out by detailed mapping (at a scale 1:10,000) along key transects along roadcuts that crossed all the geologic units of the district. Geologic observations were also made along the Piaxtla river and adjacent creeks. We also made observations along a transect to the south of the district up to the Presidio river valley to compare the stratigraphy of San Dimas with that of the Causita prospective area and the inactive Mala Noche mining area (Fig. 3). Based on the result of fieldwork and the revised stratigraphy we selected twenty-nine representative samples for petrographic and geochronological analyses. Some of these samples come from exploratory drillings provided by Primero Mining Corp (recently acquired by First Majestic Silver Corporation) that were chosen to obtain information from the lowermost part of the succession.

3.2. Petrography

Twenty-one thin-sections were analyzed petrographically. The petrographic study was made using an Olympus® BX-50 optical microscope with a Qimaging Micropublisher 5 Mp digital camera equipped with a Peltier-cooled CCD. Modal analyses were carried out using an average count of 600–800 points for igneous rocks. For rocks with porphyritic texture, phenocrysts modal proportions (crystal > 1 mm) are based on

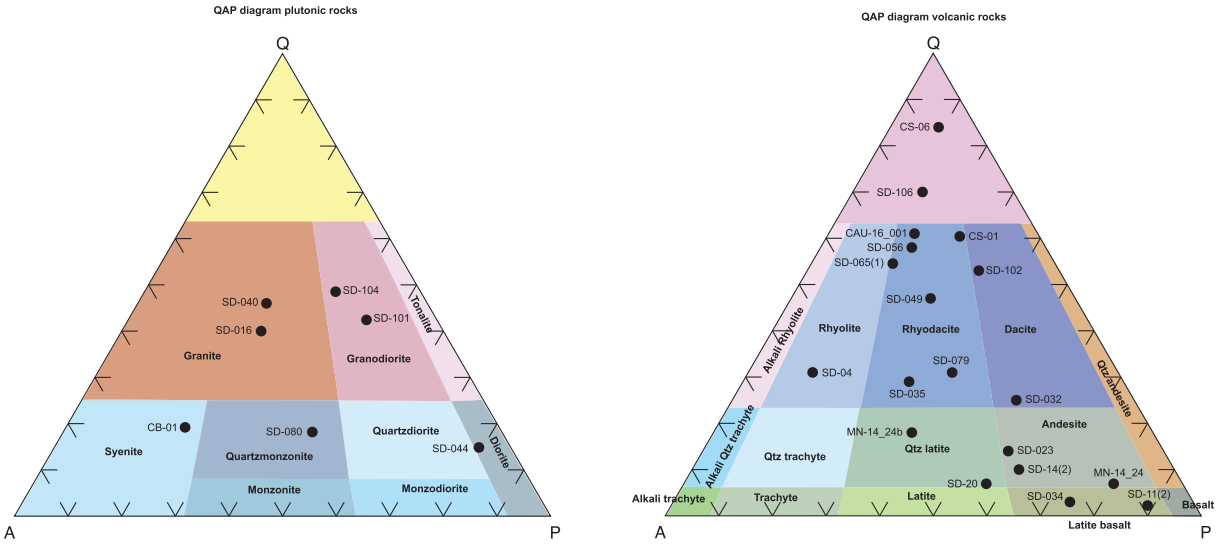

Fig. 4. Petrographic classification (Le Bas and Streckeisen, 1991) of studied samples.

a minimum of 800 points per thin-section. Samples were described according to the subcommission on the Systematic of Igneous Rocks standards (Le Maitre et al., 2002) and classified according to the Streckeisen QAP triangle for plutonic and volcanic rocks (Le Bas and Streckeisen, 1991) (Fig. 4). The composition of plagioclase was estimated by Michel-Levy's method wherever possible. Sedimentary rocks were classified according to the conventional FQR triangle for detritus samples (Folk, 1974).

3.3. U/Pb geochronology and zircon geochemistry

Twenty-nine rock samples with stratigraphic control were selected for U/Pb dating. The samples were crushed, powdered, and sieved (200–50 mesh). Heavy minerals were concentrated using conventional techniques. Zircon crystals were hand-picked under a binocular microscope and mounted with EpoFix® in a 2.5-cm-diameter plastic ring, and then, were polished. Laser ablation target points were selected based on cathodoluminescence images to identify zircon cores and overgrowth zones. Single-spot analyses were performed with a Resonetics RESOlution® LPX Pro (193 nm, ArF excimer) laser ablation system, coupled to a Thermo® Scientific iCAP® Qc quadrupole ICP-MS at Laboratorio de Estudios Isotópicos (LEI), at Centro de Geociencias, Campus Juriquilla, UNAM. For every zircon, each spot analysis consists in the acquisition of 15 s of background signal (gas blank), 30 s of ablation, and 15 s to allow the signal to reach the base-line again (washout). The spot diameter was of 33 μm, using a fluency of 6 J/cm^2 with a repetition rate of 5 Hz. Together with those isotopes required for the U/Pb age calculation (^{206}Pb, ^{207}Pb, ^{208}Pb, ^{232}Th, and ^{238}U), LA–ICP-MS permits to detect additional elements simultaneously such as major and trace elements and rare earth elements, etc. These compositional data may also be used to obtain information about the different magmatic pulses in term of mineral fertility. ICP-MS tuning follows the parameters reported in Solari et al. (2010) and Ortega-Obregón et al. (2014). Corrected isotope ratios and ages with errors were calculated with Iolite (Paton et al., 2011) using the VizualAge data reduction (Petrus and Kamber, 2012). Chemical compositions in zircons were obtained based on NIST standard glasses. "91500" zircon (Wiedenbeck et al., 1995) was used as a main reference mineral for zircon U/Pb analyses. For igneous samples, ~35 zircons were analyzed. The intrusive and volcanic ages are reported based on the weighted mean crystallization age into two standard deviations (Ludwig, 2008). Analyses outside of two standard deviation were discarded. Discordant percentages higher than twenty percent were not considered. For volcanic rocks, the preferred age was considered that of the youngest zircon populations. For igneous samples, crystals with noticeably old ages were interpreted as zircons inherited from the basement. For sedimentary samples, ~100 zircons were analyzed. The maximum age of sedimentation was associated to the younger zircons analyzed. The different family ages were reported using histograms and probability density diagrams.

3.4. Apatite fission-track thermochronology

Apatite fission-track (AFT) dating was performed at LEI Lab, using LA–ICP-MS-based technique (Hasebe et al., 2004; Donelick et al., 2005). Details of the methodology is described in Abdullin et al. (2018). In this experiment, Durango F-apatite, with an age of 31.4 ± 0.5 Ma (Hurford, 2019), was used for ζ-equivalent calibration (Hasebe et al., 2004; Donelick et al., 2005, Vermeesch, 2017) as well as for Cl measurements in unknown apatite samples (taking Durango as a primary standard, with 0.43 ± 0.03 wt% of Cl in Durango; Goldoff et al., 2012). Single-grain AFT ages with 1SE were calculated using IsoplotR (Vermeesch, 2017, 2018). The central (mean) AFT ages and different age peaks were obtained using RadialPlotter of Vermeesch (2009).

4. Results

4.1. Introduction

In this section we present our revision of the stratigraphy of the San Dimas mining district that integrates the results of new mapping and the petrographic and geochronologic studies. Table 1 presents the results obtained for twenty-nine representative samples of the stratigraphy of the San Dimas district and adjoining areas. Experimental results are presented in Figs. 5–8. For igneous rocks (Figs. 5, 6 and 8) we chose the mean age of the dominant population as the most reliable age, but Concordia diagrams are also presented to illustrate the quality of the data. Full analytical data are presented in Table 1a in the appendix. For sedimentary rocks we present probability density diagrams of detrital zircons (Fig. 7). AFT results are shown on Fig. 9 and Table 2a in the appendix. The petrographic characteristics of each geologic unit are presented in Table 2. Macro- and micro-photographs of the samples are presented in the appendix (Supplementary material, Figs. 1A–10A).

In our geological re-evaluation, the stratigraphic column is divided into five groups (Fig. 10): 1) the silicic to intermediate ignimbrites and lavas from the lower part of the LVC and the San Ignacio batholith; 2) the Andesitic Group, composed by intermediate lavas and hypabyssal intrusions; 3) the Piaxtla batholithic intrusion and associated dikes, 4)

Table 1
Summary of new U-Pb ages.

Sample	Geologic unit and location	Long. W (datum WGS84)	Lat. N (datum WGS84)	Elevation (m asl)	Rock type	Age (Ma)	Error (Ma)	Age type	Comments
Sierra Madre Occidental silicic large igneous province – Upper Volcanic Supergroup									
CS-06	Second flare-up. First ash flow above a conglomerate covering tilted ignimbrites at Causita	105°46′45.08″	24°0′47.72″	2595	Ash flow tuff	**26.2**	**0.29**	Tuffzirc average	MSWD = 0.77. Mean of 14 grains of the dominant population (max age)
SD-102	Silicic dike intruded by mafic dike, riverbed near La Puerta	106°00′23.57″	24°04′4.45″	415	Silicic pyroclastic dike	**27.0**	**1.00**	Tuffzirc average	MSWD = 0.16. Mean of 24 grains of the dominant population
SD-106	Silicic lava near riverbed. Road Tayoltita to San Ignacio	106°08′14.40″	23°59′31.23″	290	Porphyritic rhyolitic lava	**29.0**	**0.54**	Tuffzirc average	MSWD = 0.57. Mean of 26 grains of the dominant population
CB-01	Shallow intrusion just north of Cebollas, below ignimbrites	105°4820.94″	24°4246.02″	1200	Fine-grained, hb-rich syenite	**31.3**	**0.48**	Tuffzirc average	MSWD = 3.1. Mean of 14 grains of the dominant population
						30.0	0.76	Lower intercept	MSWD = 1.4
SD-034	Guarisamey andesite member right above SD 035. Piaxtla river east of Guarisamey	105°53′10.53″	24°08′21.87″	600	Porphyritic latite basaltic lava	**31.0**	**1.10**	Tuffzirc average	MSWD = 0.59. Mean of the 4 younger grains. Large xenocrystic population at ~43 to 45 Ma. Three Late Cretaceous xenocrysts.
SD-035	First volcanic unit above sedimentary unit. Piaxtla river east of Guarisamey	105°53′9.43″	24°08′13.25″	595	Reddish ignimbrites with plag, san, qz	**31.5**	**0.80**	Tuffzirc average	MSWD = 1.9. Mean of 6 the younger grains. Probable antecrystic population at ~32 Ma
Volcano-sedimentary unit									
SD-029	Camichin unit, road Tayoltita to Guarisamey	105°54′20.58″	24°07′19.07″	975	Lithic tuff	**43.2**	**2.30**	Max deposition age, mean of the 2 younger zircons.	One peak at 56 Ma. 20 zircons in the range 53–68 Ma, one at 140 Ma and two > 500 Ma
SD-031	Palmas Formation, road Tayoltita to Guarisamey	105°54′16.28″	24°07′26.96″	965	Lithic arkose	**52.1**	**1.40**	Max deposition age, mean of the 5 younger zircons.	Two peaks at 56 and 65 Ma. 99 Zircons in the range 52–82 Ma. One at 95 Ma.
Lower Volcanic Complex									
Piaxtla intrusive suite									
SD-023	"Santa Rita"-type dike cutting Piaxtla batholith, 3 km west of Tayoltita	105°56′50.26″	24°05′08.30″	543	Porphyritic andesite with plag, hb, bio and qz	**45.0**	**0.51**	Tuffzirc average	MSWD = 0.25. Mean of 24 grains of the dominant population
SD-032	"Bolaños"-type dike cutting Piaxtla batholith, road to Guarisamey, 3 km east of Tayoltita	105°54′08.25″	24°07′43.96″	790	Porphyritic dacite with qz, plag, hb	**45.4**	**0.66**	Tuffzirc average	MSWD = 0.41. Mean of 21 grains of the dominant population
SD-040	Piaxtla batholith, San Francisco tunnel	105°55′49.24″	24°06′36.25″	463	Fine grained granite with qz, plag, bio, hb, px	**45.2**	**0.85**	Tuffzirc average	MSWD = 1.5. Mean of 27 grains of the dominant population
SD-101	Piaxtla batholith, riverbed at La Puerta	106°00′29.15″	24°04′17.85″	417	White, coarse grained granodiorite with qz, plag, feld, hb, px, bio	**47.0**	**0.75**	Tuffzirc average	MSWD = 1.4. Mean of 29 grains of the dominant population
SD-079	Porphyritic andesite, "Santa Rita" dike, Santa Rita mine near entrance fo the main tunnel.	105°54′16.77″	24°07′11.02″	800	Porphyritic rhyodacite	**47.5**	**0.93**	Tuffzirc average	MSWD = 4.9. Mean of 27 grains of the dominant population
SD-065(1)	Porphyritic andesite, "Santa Lucia" dike, San Luis tunnel between Santa Lucia and San Salvador veins	105°58′21.58″	24°0811.27″	799	Porphyritic rhyodacite	**48.0**	**0.67**	Tuffzirc average	MSWD = 1.4. Mean of 20 grains of the dominant population
SD-080	Porphyritic andesite, "Santa Lucia" dike, San Luis tunnel between Santa Lucia and San Salvador veins	105°58′21.58″	24°0811.27″	799	Porphyritic quartzomonzonite	**48.0**	**0.46**	Tuffzirc average	MSWD = 1.3. Mean of 24 grains of the dominant population
SD-016	Piaxtla batholith, "El Cristo" facies, near entrance of the tunnel. Intrusive contact with Socavón member	105°56′15.30″	24°05′34.96″	573	Fine grained granite with qz, alk feld, plag, hb	**49.0**	**0.43**	Tuffzirc average	MSWD = 0.25. Mean of 35 grains of the dominant population. 9 xenocrysts in the range 74–65 Ma (age of Tarahumara Fm)

(*continued on next page*)

Table 1 (*continued*)

Sample	Geologic unit and location	Long. W (datum WGS84)	Lat. N (datum WGS84)	Elevation (m asl)	Rock type	Age (Ma)	Error (Ma)	Age type	Comments
SD-104	Piaxtla batholith, riverbed 7 km west of La Puerta	106°03′44.40″	24°02′20.50″	350	Medium to fine grained granodiorite with plag, qz, bio, hb	**49.1**	**0.94**	Tuffzirc average	MSWD = 0.94. Mean of 21 grains of the dominant population
San Ignacio batholith									
SD 107	San Ignacio batholith, 16 km east of San Ignacio. Locally completely altered to unconsolidated sand	106°16′9.50″	23°57′17.83″	253	Medium grained granodiorite	**64.2**	**0.90**	Tuffzirc average	MSWD = 3.2. Mean of 25 grains of the dominant population
Tarahumara formation									
SD-049	Portal member. San Jose tunnel, recess 598	105°59′53.92″	24°07′26.12″	878	Lithic rhyodacite ignimbrite	**69.0**	**1.70**	Tuffzirc average	MSWD = 0.92. Mean of 4 grains of the dominant population
SD-014(2)	Buelna member, 4 km SSW of San Dimas	105°58′15.89″	24°07′05.51″	665	Porphyritic andesitic lava	**69.0**	**0.85**	Tuffzirc average	MSWD = 3.6. Mean of 16 grains of the dominant population
SD-056	Porphyry intrusion within the Socavón member, stream at the Sinaloa-Durango border	105°59′50.07″	24°06′51.79″	620	Porphyry rhyodacite	**73.0**	**1.50**	Tuffzirc average	MSWD = 1.7. Mean of 14 grains of the dominant population
SD-004	Socavón member, Tayoltita to San Dimas road	105°55′49.12″	24°08′08.39″	1176	Lithic porphyritic rhyolitic lava	**75.0**	**0.77**	Tuffzirc average	MSWD = 1.02. Mean of 19 grains of the dominant population
SD-020	Socavón member, near Piaxtla river 2 km west of Tayoltita	105°56′49.18″	24°05′23.49″	570	Quartz latite lava	**75.4**	**0.80**	Tuffzirc average	MSWD = 0.57. Mean of 20 grains of the dominant population
MN-14_24b	Mala Noche drillhole. This rock is observed intruding the whole drilling	105°44′47.981″	23°54′15.923″	1038	Px-rich porphyritic quartz latite	**75.5**	**1.00**	Lower intercept	MSWD = 4.7
MN-14_24	Mala Noche drillhole.	105°44′47.95″	23°54′15.906″	950	Andesitic lava	**76.1**	**0.63**	Tuffzirc average	MSWD = 4.6. Mean of 28 grains of the dominant population
CAU-16_001	Causitas drillhole. This rock includes clast of the whole sequence. Dated as detrital	105°4656.21″	24°058.24	2358	Lithic rhyodacite lava	**76.5**		Peak in PDD	91 zircones in the range 70–83 Ma, one at 91 Ma and one at 131 Ma
CS-01	Lava hosting the an epithermal vein at Causita.	105°46′58.50″	24° 0′59.08″	2518	Rhyodacite ignimbrite	77.5		Peak in probability density diagram	93 zircons in the range 71–84 Ma, one at 90.5 Ma and four at 132–139 Ma
						77.7	**0.88**	Tuffzirc average	MSWD = 5.3. Mean of 31 grains of the dominant population

Preferred ages in bold.

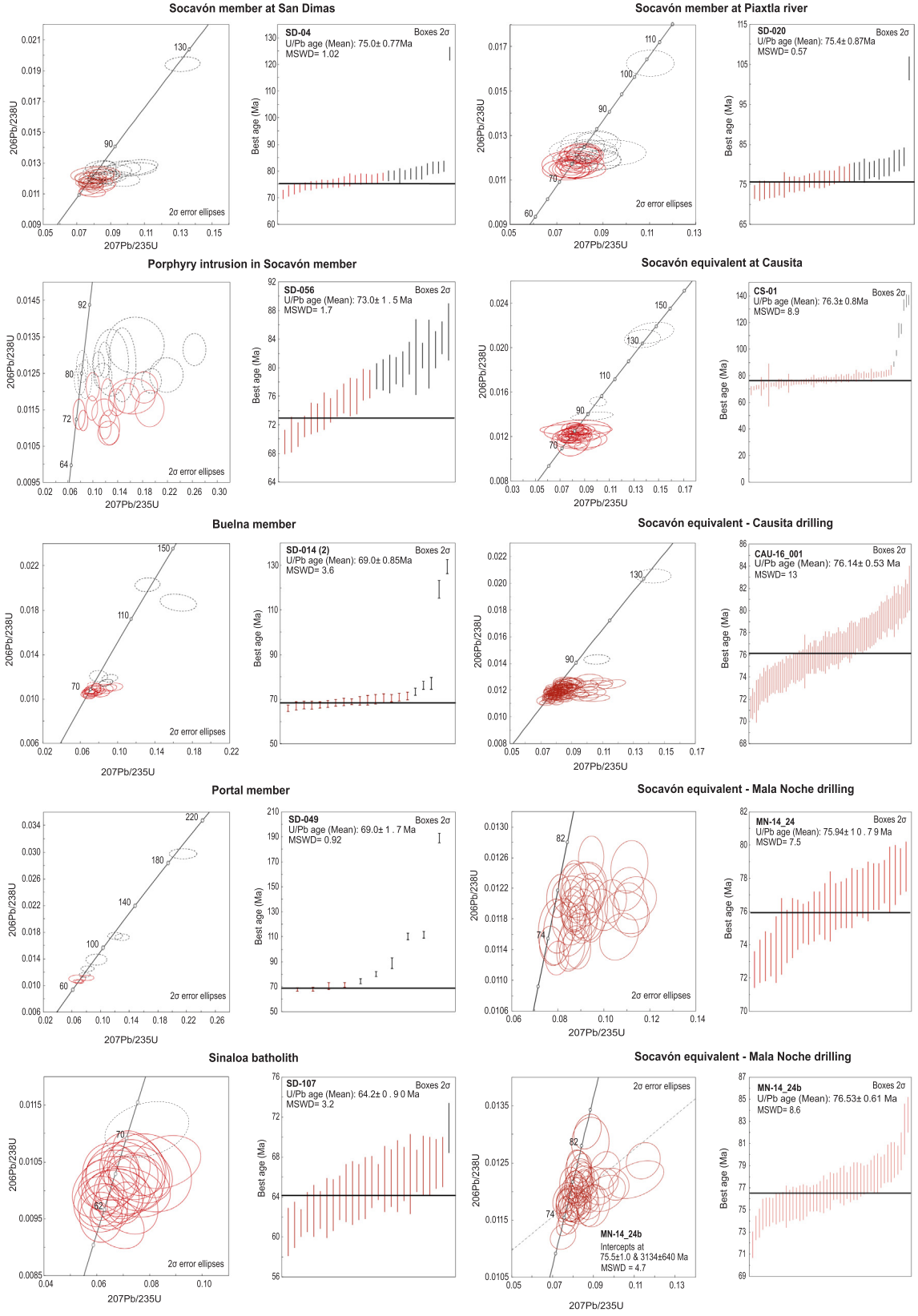

Fig. 5. Histograms and concordia diagrams of U-Pb ages for zircons of the Lower Volcanic Complex. Errors in calculated ages are 2σ. Black ellipses are data points not used in calculating the weighted mean.

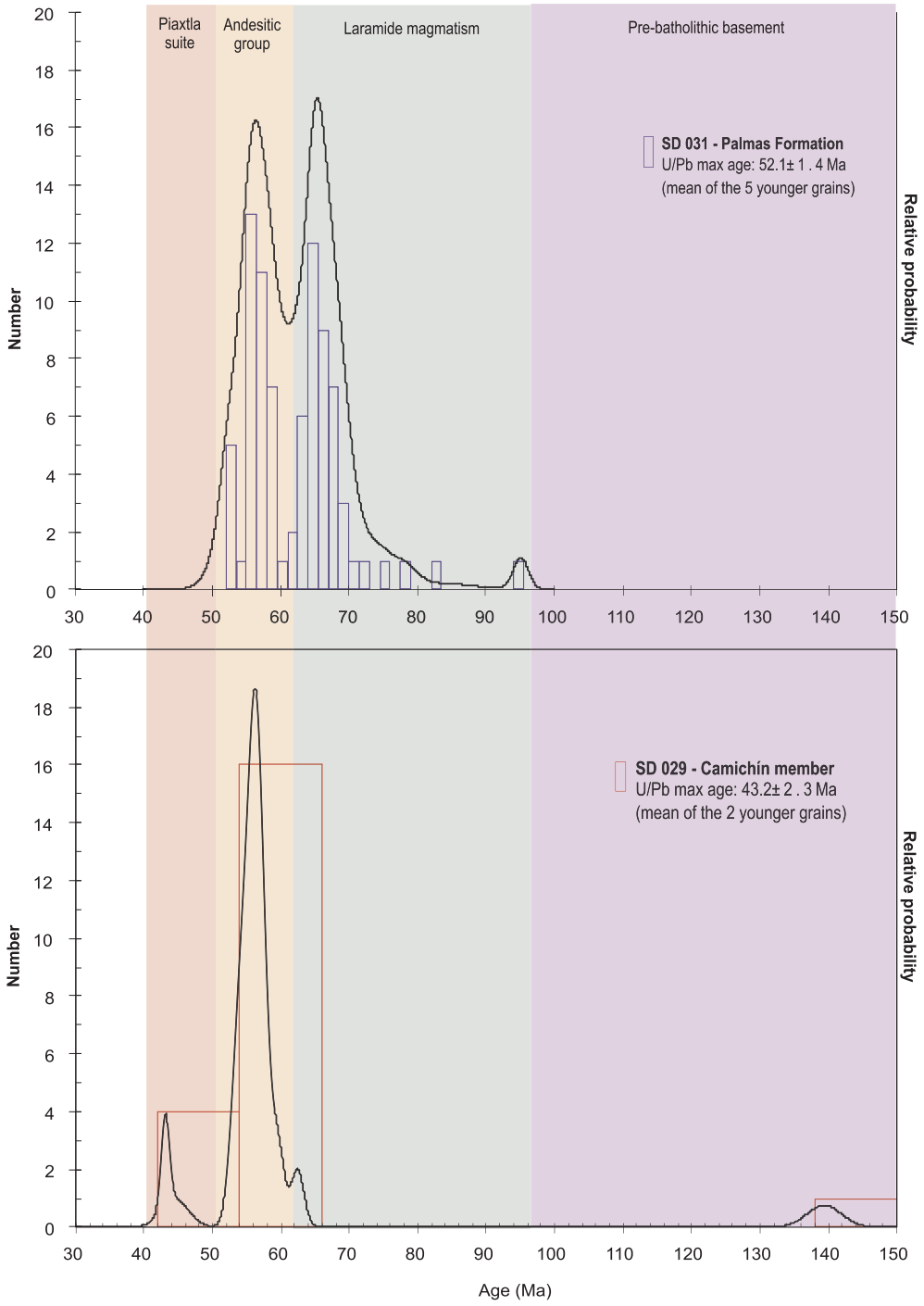

Fig. 6. Histograms and concordia diagrams of U-Pb ages for zircons of the Piaxtla intrusive suite. Errors in calculated ages are 2σ. Black ellipses are data points not used in calculating the weighted mean.

the Las Palmas and Camichín continental sedimentary deposits, and 5) the Oligocene to early Miocene silicic ignimbrites, rhyolite domes and mafic lavas belonging to the UVS.

It is important to note that a large part of the district was affected by hydrothermal alteration, mainly in the form of propylitization (chlorite–epidote–calcite–pyrite). This alteration is pervasive at a local scale, increases in intensity close to the mineralized structures and it is overprinted by phyllic alteration close to vein structures.

4.2. Lower volcanic complex

4.2.1. Late Cretaceous volcanic sequence

The oldest rocks belong to a thick volcanic succession exposed in the lower part of the valleys north of the Piaxtla River with a total thickness of approximately 2 km. The succession is composed by a series of andesitic to rhyolitic lava flows, tuffs, and breccias defined as the Socavón, Buelna and Portal members. The Socavón member consists of an alternating suite of rhyolitic and andesite lavas locally intruded by mineralized felsic porphyritic bodies. It commonly presents a porphyritic texture, reddish to gray in color, and consists of quartz > orthoclase > plagioclase > pyroxene > biotite and hornblende in a

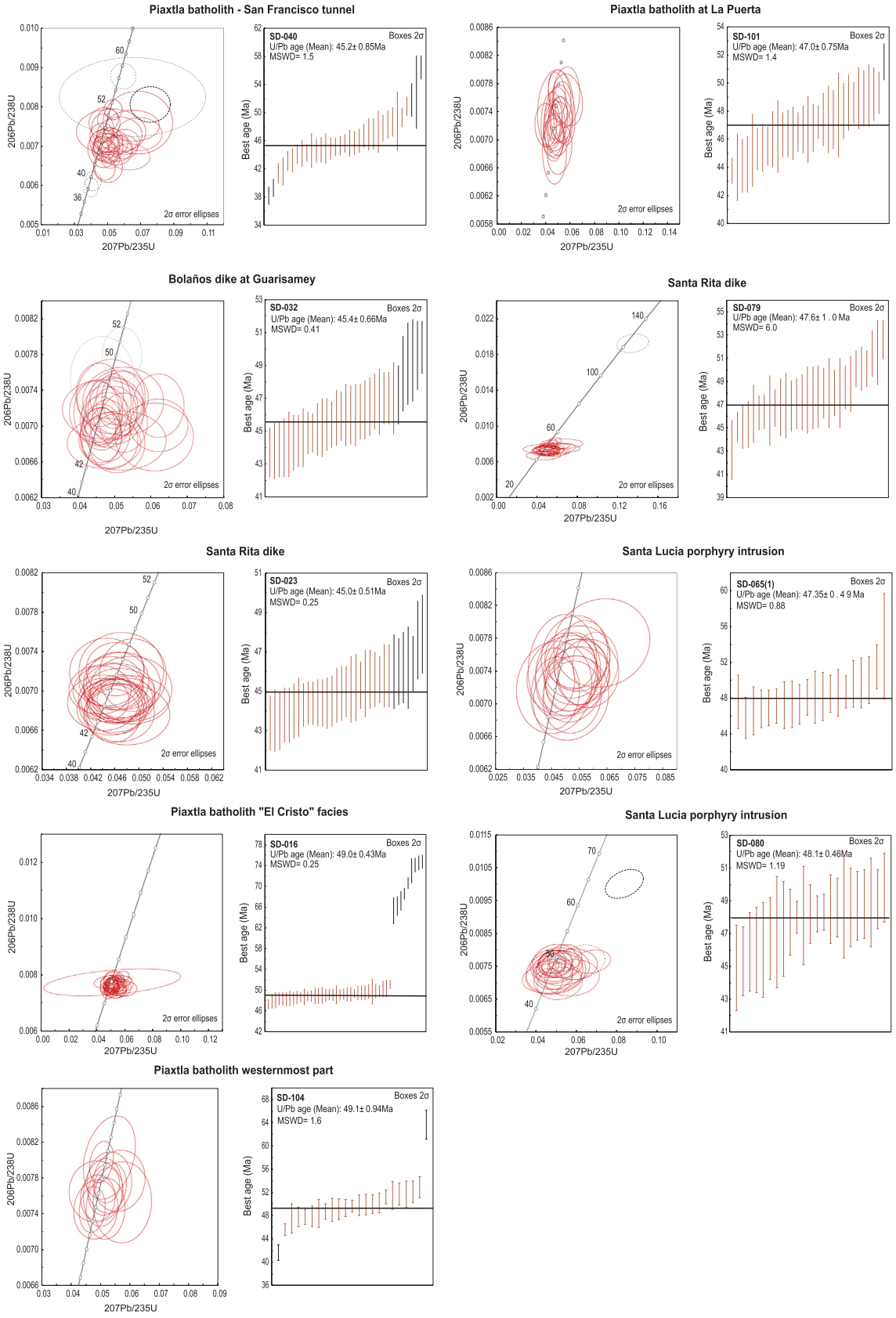

Fig. 7. Histograms and probability density diagrams for detrital zircons from the Las Palmas (upper panel) and Camichin (lower panel) continental sedimentary deposits, with indication of the main magmatic pulses in the San Dimas region.

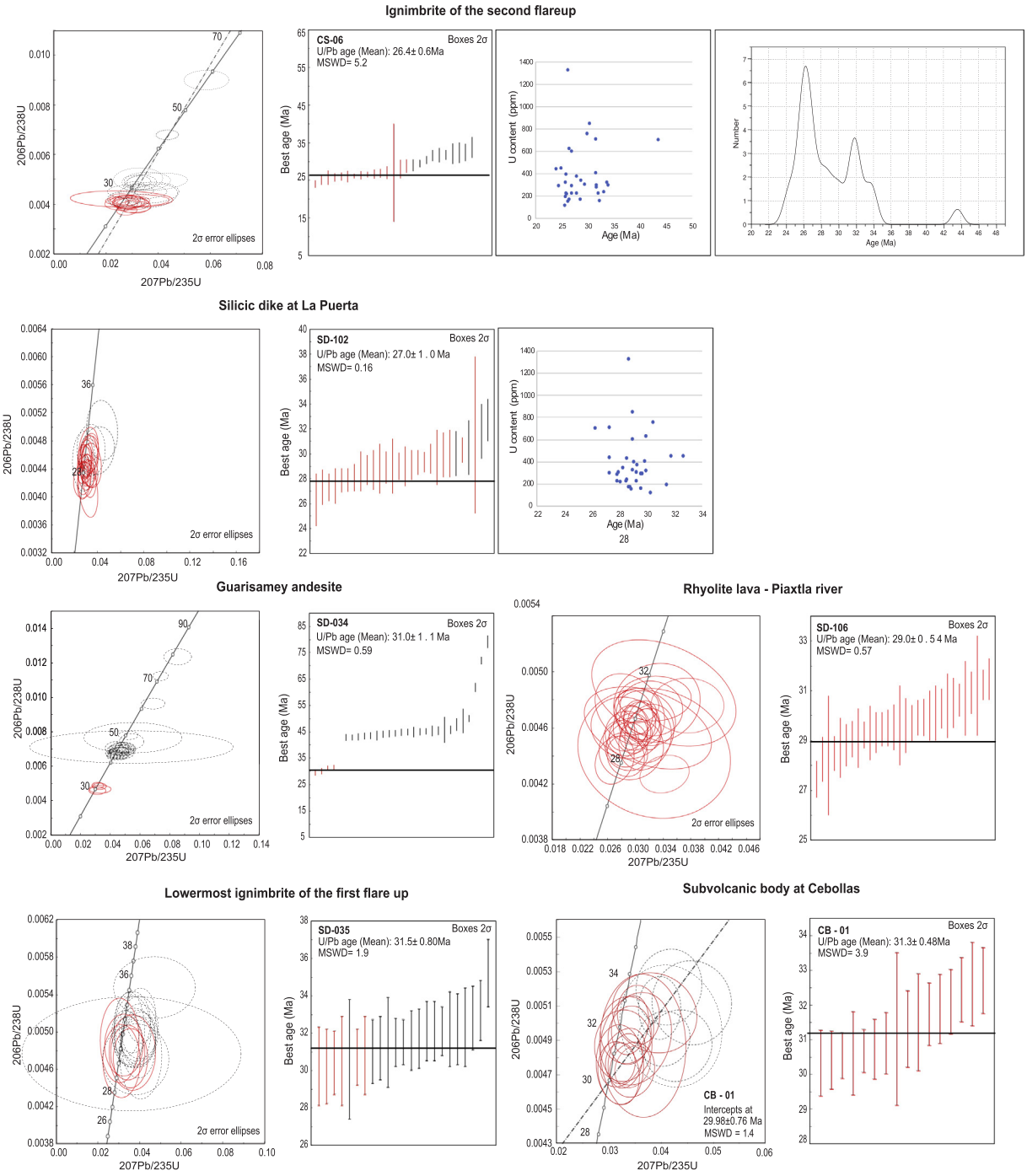

Fig. 8. Histograms and concordia diagrams of U-Pb ages for zircons of the Upper Volcanic Supergroup. Errors in calculated ages are 2σ. Black ellipses are data points not used in calculating the weighted mean.

groundmass of fine plagioclase and glass with lithic fragments at the base. This member crops out throughout the district with up to 800 m of thickness. The alteration of mineralized porphyritic bodies is associated with pervasive secondary biotite overprinted by sodic–calcic (albite–actinolite–epidote) alteration around sinuous quartz, pyrite, and chalcopyrite veins. The mineralized bodies are exposed in the western Block in the Contraestaca area (Fig. 3). We obtained two ages of 75.4 ± 0.8 and 75.0 ± 0.7 Ma for the Socavón member (SD 020 and 004) and an age of 73.0 ± 1.5 Ma for a porphyry dacitic intrusion (SD 056) (Fig. 5). The latter sample displays a wide range of grain ages from 69 to 82 Ma.

The Buelna member is a sequence of intermediate lavas characterized by porphyritic-fine texture and bedding, which commonly contain anhedral to subhedral crystals of plagioclase > quartz > hornblende > biotite in a groundmass of fine plagioclase. This member crops out throughout the district on top of the Socavón member with a thickness ranging from 20 to 100 m. One sample from the type locality yielded an age of 69.8 ± 0.85 Ma (SD 014-2) (Fig. 5).

The Portal member is a sequence of rhyolite flows and tuffs with a lithic-rich layer at the base and a thickness of 50–250 m. It contains anhedral crystals of quartz > plagioclase > biotite in a fine-grained sericitized groundmass. We obtained an age of 69.0 ± 1.7 Ma (SD 049) (Fig. 5) for a sample of the Portal member from the interior of the mine.

Volcanic rocks lithologically similar to the Socavón member were

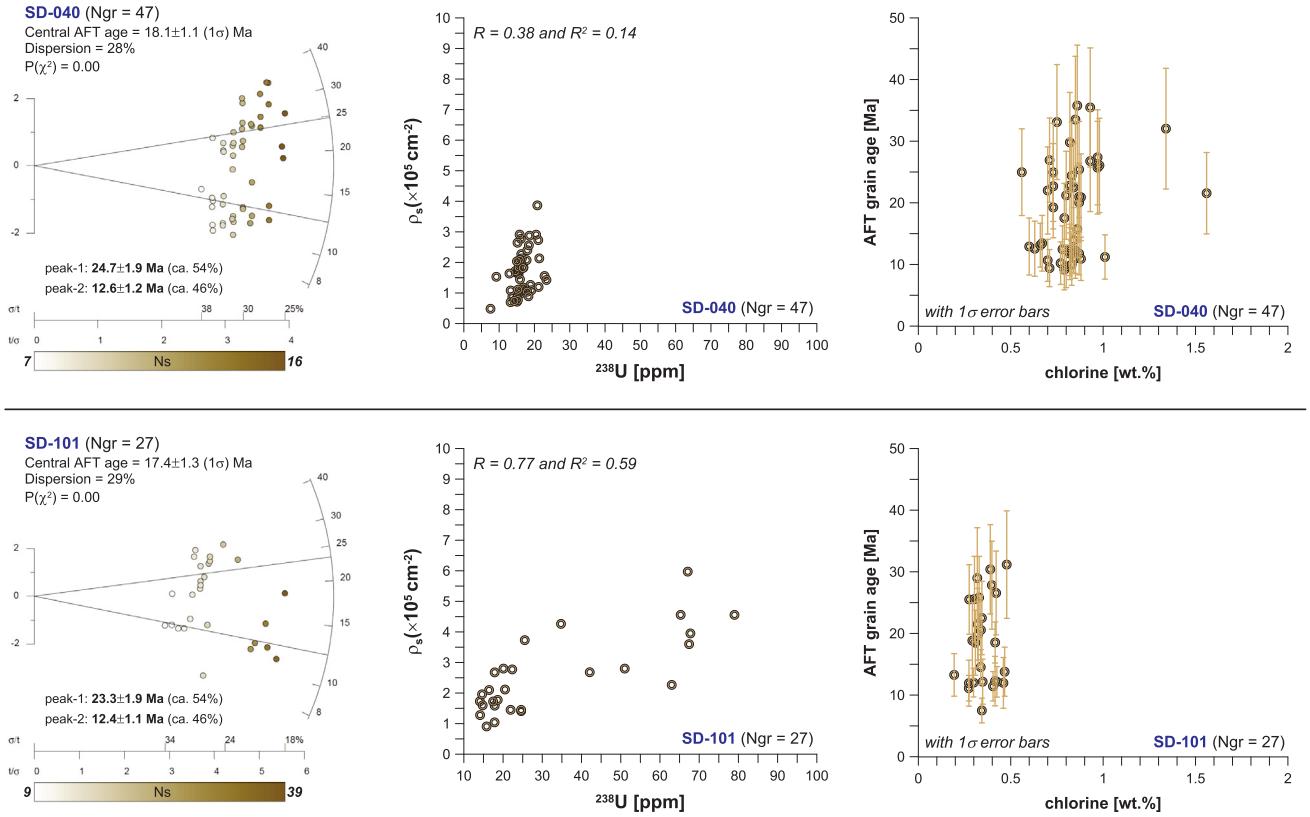

Fig. 9. Apatite fission-track results for samples SD-040 and SD-101. Radial plots were constructed using RadialPlotter of Vermeesch (2009). Ngr – number of apatite grains dated; P(χ^2) – chi-squared probability test; Ns – number of spontaneous tracks counted to calculate the track densities in individual apatites. The track density (ρ_s) versus ^{238}U concentration (analogue to isochron) and the single-grain age versus Cl content diagrams are also presents.

mapped south of the San Dimas district (Fig. 3). The main outcrops are in the creek west of Causita and in the Presidio River valley in the Mala Noche mining area. Two samples from the Causita area (CAU 16 001, CS 01) and two more from drillings in the Mala Noche area (MN 14-24, MN 14-24b) yielded tightly clustered ages comprised between 77.7 ± 0.88 and 75.5 ± 1.0 Ma (Fig. 5, Table 1), which confirm the correlation with the Socavón member.

4.2.2. San Ignacio batholith

Our new Late Cretaceous ages for the lower volcanic succession at San Dimas make them coeval with the intrusive assemblage forming the San Ignacio granodiorite as defined by Henry et al. (2003), which is exposed west of the district along the Piaxtla river in the homonymous area (Fig. 2). Along the riverbed the batholith is clearly distinguishable from the younger Piaxtla batholith for its pervasive alteration and a more mature erosional landscape. The dominant lithology is a medium-grained equigranular granodiorite which contains anhedral biotite, hornblende, and clinopyroxene. We have dated one sample from the eastern part of the batholith, 16 km east of San Ignacio obtaining an age of 64.2 ± 0.9 Ma (SD 107) (Fig. 5), which is in line with previous K–Ar ages reported by Henry et al. (2003).

4.2.3. Andesite group

Andesitic subvolcanic bodies and lava flows are found intruding and covering, respectively, the Late Cretaceous succession of the San Dimas district with a cumulative thickness comprised between 200 and 850 m. Observations in mine interior indicate that the group display a range of texture without intrusive contacts between them. The sequence commonly starts with an andesite lava agglomerate with a fine texture, rich in lithic fragments (“Productive andesite”), which passes transitionally to a porphyritic texture (“Intrusive andesite”) and then to a granular texture (“Arana diorite”). Regardless of the texture the andesite group is normally composed by plagioclase > hornblende > pyroxene > quartz ± biotite in an aphanitic groundmass (Fig. 11). Due to high hydrothermal alteration, these andesite bodies could not be dated by the ^{40}Ar–^{39}Ar method and because of their chemistry, zircon crystals are very rare. After several attempts we could separate a few zircons, which yielded a ~63 Ma age. Although insufficient to provide a statistically robust age, this value is consistent with the stratigraphic position of the Andesite group. Porphyritic andesite intrusions, composed by medium to fine crystal of plagioclase > quartz > biotite > hornblende > pyroxene and chlorite in a fine plagioclase groundmass cut the andesite group in the Santa Lucia mine. We have dated two of these bodies (SD 065-1, SD 080), which yielded indistinguishable ages of ~48 Ma. These crosscutting relationships and the few dated zircons indicate that the andesite group was emplaced in the Paleocene-early Eocene time span.

4.2.4. Piaxtla intrusive complex

Intrusive bodies of dioritic, granodioritic and granitic composition were grouped into the Piaxtla intrusive complex. This intrusive complex is part of a batholith well exposed in the Piaxtla river that intrudes the lower volcanic succession and the Andesite Group. The Piaxtla intrusive rocks present a wide range of texture, from equigranular to porphyritic (in dikes). The dominant lithology consists of medium to coarse grained granite to granodiorite. The oldest body, called “El Cristo granite”, is exposed just south of the Piaxtla River near Tayoltita (Fig. 3). El Cristo is a fine-grained granite rich in K-feldspar that yielded an age of 49.0 ± 0.43 Ma (SD 016) (Fig. 6). A similar age of 49.1 ± 0.94 Ma was obtained in the westernmost part of the batholith along the Piaxtla river (SD 104) (Fig. 6). The main Piaxtla body consists of a medium to coarse grained granite with quartz > plagioclase > feldspar > biotite, but richer in pyroxene and hornblende. Two samples taken ~8 km apart gave slightly different ages of 47.0 ± 0.75 Ma and

Table 2
Petrography summary.

Sample	Geologic unit and location	Long. W	Lat. N	Elevation (m asl)	Rock type	Age (Ma)	Petrography description
Sierra Madre Occidental silicic large igneous province – Upper Volcanic Supergroup							
CS-06	Second flare-up. First ash flow above a conglomerate covering tilted ignimbrites at Causita	105°46′45.08″	24°0′47.72″	2595	Ash flow tuff	26.2 ± 0.29	Ash flow tuff. Sequential porphyritic texture, hialocrystaline with subeuhedral crystals of quartz (84%) > plagioclase (An 9%) > feldspar (Alk + Alb 7%) > biotite in a vitreous matrix. Clasts of andesite ignimbrite with epidote alteration and andesite ignimbrites with sericite and pyrite alteration. Strong sericite alteration overpirnted by epidote and Fe oxides in clasts. Two types of pyrites are presented, fine and coarse grain less than 1%.
SD-102	Silicic dike intruded by mafic dike, riverbed near La Puerta	106°00′23.57″	24°04′4.45″	415	Silicic pyroclastic dike	27.6 ± 1.00	Dacite pyroclastic dike. Sequential porphyritic texture, hialocrystaline and anahedral crystals of quartz (53%) > biotite > plagioclase (An 32%) > feldspar (Alk + Alb 15%). Strong pervasive sericite alteration. Two types of pyrites are presented: coarse and fine grain both less than 1%.
SD-106	Silicic lava near riverbed. Road Tayoltita to San Ignacio	106°08′14.40″	23°59′31.23″	290	Porphyritic rhyolitic lava	29 ± 0.54	Rhyolitic lava with quartz "eyes". Sequential porphyritic texture, holocrystaline and subeuhedral to anahedral crystals of quartz (70%) > feldspar (Alk + Alb 17%) > plagioclase (An 13%) > biotite. Strong diseminated sericite alteration overpirnted by pervasive moderated epidote. Two types of pyrite were found: 1) palid coarse grain (< 0.01%) and fine grain (< 0.01%). Overgrown quartz textures are present
CB-01	Shallow intrusion just north of Cebollas, below ignimbrites	105°48′20.94″	24°42′46.02″	1200	Fine-grained, hb-rich syenite	31.2 ± 0.43 30 ± 0.76	Syenite. Coarse to medium grain, equigranular texture, holocrystaline and anahedral crystals of feldspar (Alk + Alb 58%) > plagioclase (An 22%) > quartz (19%) > hornblende. Strong pervasive alteration of epidote, sericite and weak chlorite and calcite. Medium grain sphalerite is presented (< 3%) with fine pyrite inclutions (< 2%), Fe oxides were also found.
SD-034	Guarisamey andesite member right above SD 035. Piaxtla river east of Guarisamey	105°53′10.53″	24°08′21.87″	600	Porphyritic latite basaltic lava	31 ± 1.1	Latite basaltic lava. Porphyritic texture, holocrystaline of subeuhedral plagioclases (An 74%) > feldspar (Alk + Alb 23%) > quartz (3%) in a microcrystaline matrix (30%) with Fe oxides. Moderated sericite and biotite alteration in crystals and weak calcite. Fine anahedral pyrite is presented less than 1%. Broken crystals of plagioclase and quartz are presented.
SD-035	First volcanic unit above sedimentary unit. Piaxtla river east of Guarisamey	105°53′9.43″	24°08′13.25″	595	Reddish ignimbrites with plag, san, qz	31.5 ± 0.80	Reddish rhyodacite ignimbrite. Porphyritic texture, hialocrystaline with anahedral crystals of feldspar (Alk + Alb 40%) > plagioclase (An 31%) > quartz (29%). Strong pervasive sericite alteration overprinted by moderated chlorite and weak calcite. Two types of pyrite are presented: 1) fine grain in matrix (< 3%) and 2) coarse grain asociated to coarse quartz (< 1%). Coarse chalcopyrite is also presented less than 1%
Volcano-sedimentary unit							
SD-029	Camichin unit, road Tayoltita to Guarisamey	105°54′20.58″	24°07′19.07″	975	Lithic tuff	43.2 ± 2.30	Lithic tuff. Lithic fragments of porphyritic andesites, traquite andesites, rhyolites and sedimentary rocks inmerse into a vitreous matrix. Strong sericite alteration in matrix. Coarse grain pyrite is presented less than 1% associated to the lithic fragments.
SD-031	Palmas Formation, road Tayoltita to Guarisamey	105°54′16.28″	24°07′26.96″	965	Lithic arkose	52.1 ± 1.40	Lithic arkose. Detritic rock with clastic texture in a feldspar cement. Sandstone grain size of feldspar > lithic fragments > quartz. Sub-rounded to rounded clasts and inmadure. Lithic fragments of porphyritic andesites, felsic intrusions, volcanic and sedimentary rocks. Strong pervasive alteration of sericite, chlorite, epidote.
Lower Volcanic Complex							
Piaxtla intrusive suite							
SD-023	"Santa Rita"-type dike cutting Piaxtla batholith, 3 km west of Tayoltita	105°56′50.26″	24°05′08.30″	543	Porphyritic andesite with plag, hb, bio and qz	45 ± 0.51	Porphyritic andesite. Porphyritic texture, holocrystaline and subeuhedral crystals of plagioclase (An 57%) > feldspar (Alk + Alb 29%) > quartz (14%) > hornblende > biotite in a microcrystaline matrix of plagioclase. Strong alteration in crystals of sericite overprinted by moderated biotite and weak calcite and chlorite. Broken coarse pyrites are less than 1%. Overgrown quartz and graphic textures are present
SD-032	"Bolaños"-type dike cutting Piaxtla batholith, road to Guarisamey, 3 km east of Tayoltita	105°54′08.25″	24°07′43.96″	790	Porphyritic dacite with qz, plag, hb	45.4 ± 0.66	Porphyritic dacite. Sequential and porphyritic texture, holocrystaline and anahedral crystals of plagioclase (An 53%) > quartz (25%) > feldspar (Alk + Alb 22%) > hornblende in a microcrystaline matrix of silice. Strong pervasive sericite

(*continued on next page*)

Table 2 (*continued*)

Sample	Geologic unit and location	Long. W	Lat. N	Elevation (m asl)	Rock type	Age (Ma)	Petrography description
							alteration overprinted by moderated chlorite in crystals. Coarse euhedral pyrite is less than 1%.
SD-040	Piaxtla batholith, San Francisco tunnel	105°55′49.24″	24°06′36.25″	463	Coarse grained granite with qz, plag, bio, hb, px	45.2 ± 0.85	Coarse grain granite. Coarse equigranular texture, holocrystaline and subeuhedral crystals of quartz (46%) > feldspar (Alk + Alb 30%) > plagioclase (An 24%) > biotite > hornblende. Two events of plagioclase and biotite are presented: 1) with alteration, 2) without alteration. Strong alteration in crystals of sericite is overprinted by moderated calcite and chlorite. Accesory minerals, apatite, zircon and opaques. Coarse euhedral pyrite and chalcopyrite are presented. Overgrown quartz and graphic textures are present
SD-101	Piaxtla batholith, riverbed at La Puerta	106°00′29.15″	24°04′17.85″	417	White, coarse grained granodiorite with qz, plag, feld, hb, px, bio	47 ± 0.75	Coarse grain granodiorite. Coarse equigranular texture, holocrystaline and subeuhedral crystals of plagioclase (An 44%) > quartz (42%) > feldspar (Alk + Alb 13%) > biotite > anfibol. Weak pervasive sericite and chlorite alteration. Coarse pyrite less than 1%. Overgrown quartz and graphic textures are presented.
SD-079	Porphyritic andesite, “Santa Rita” dike, Santa Rita mine near entrance fo the main tunnel.	105°54′16.77″	24°07′11.02″	800	Porphyritic rhyodacite	47.5 ± 0.93	Porphyritic rhyodacite. Sequential porphyritic texture, holocrystaline with anahedral crystals of plagioclase (An 38%) > quartz (31%) > feldspar (Alk + Alb 31%) > piroxene > anfibole. Strong pervasive sericite and chlorite alteration overprinted by moderated epidote and weak calcite. Coarse euhedral pyrite is less than 0.1%.
SD-065(1)	Porphyritic dacite, “Santa Lucia” dike, San Luis tunnel between Santa Lucia and San Salvador veins	105°58′21.58″	24°08́11.27″	799	Porphyritic rhyodacite	48 ± 0.67	Porphyritic rhyodacite. Sequential porphyritic texture, holocrystaline with subeuhedral crystals, from coarse to Medium grain, of quartz (54%) > feldspar (Alk + Alb 30%) > plagioclase (An 15%) > piroxene > anfibol > biotite. Strong diseminated sericite alteration overprinted by moderated chlorite, epidote alteration and weak calcite. Coarse euhedral pyrite is presented less than 5%.
SD-080	fPorphyritic andesite, “Santa Lucia” dike, San Luis tunnel between Santa Lucia and San Salvador veins	105°58′21.58″	24°08́11.27″	799	Porphyritic quartzomonzonite	48 ± 0.46	Porphyritic quartzomonzonite. Sequential porphyritic texture, holocrystaline with anahedral crystals of plagioclase (An 46%) > feldspar (Alk + Alb 35%) > quartz (18%) > biotite > piroxene > anfibole. Strong diseminated sericite and chlorite, moderated epidote and weak calcite alteration. Fine euhedral pyrite is less than 0.1%.
SD-016	Piaxtla batholith, “El Cristo” facies, near entrance of the tunnel. Intrusive contact with Socavón member	105°56′15.30″	24°05′34.96″	573	Fine grained granite with qz, alk feld, plag, hb	49 ± 0.43	Fine grain granite. Fine equigranular texture, holocrystaline with crystals of quartz (40%) > feldspar (Alk + Alb 34%) > plagioclase (An 26%) > hornblende. Moderated pervasive sequndary biotite overprinted by weak sericite, chlorite and epidote. Fine and coarse pyrite are presented less than 1%. Overgrown quartz textures are presented.
SD-104	Piaxtla batholith, riverbed 7 km west of La Puerta	106°03′44.40″	24°02′20.50″	350	Medium grained granodiorite with qz, plag, bio, hb	49.1 ± 0.94	Granodiorite. Medium equigranular texture, holocrystaline with crystals of quartz (49%) > plagioclase (An 36%) > feldspar (Alk + Alb 16%) > biotite > anfibole. Weak pervasive chlorite, sericite and calcite alteration. Coarse euhedral pyrite was found less than 0.3%.
Sinaloa batholith							
SD-107	Sinaloa batholith, 16 km east of San Ignacio. Locally completely altered to unconsolidated sand	106°16′9.50″	23°57′17.83″	253	Medium grained granodiorite	64.16 ± 0.90	
Tarahumara formation							
SD-049	Portal member. San Jose tunnel, recess 598	105°59′53.92″	24°07′26.12″	878	Lithic rhyodacite ignimbrite	69 ± 1.70	Lithic rhyodacite ignimbrite. Porphyritic texture, hialocrystaline with subeuhedral to anahedral crystals (20%) of quartz (47%) > feldspar (Alk + Alb 27%) > plagioclase (An 26%) > biotite. Angular clasts of coarse and tabular porphyritic andesites and agregates of quartz. Strong sericite in crystals, moderated calcite and weak chlorite in halos around crystals. Fine euhedral pyrite is less than 1%.
SD-014(2)	Buelna member, 4 km SSW of San Dimas	105°58′15.89″	24°07′05.51″	665	Porphyritic andesitic lava	69 ± 0.85	Porphyritic andesitic lava. Sequential porphyritic texture. Holocrystaline with anahedral to euhedral crystals (30%) of plagioclase (An 61%) > feldspar (Alk + Alb 29%) > quartz (10%) > hornblende > biotite in a afanitic matrix of tabular plagioclases (70%). Weak pervasive chlorite, sericite and epidote. Coarse Py less than 1%.
SD-056		105°59′50.07″	24°06′51.79″	620	Porphyry rhyodacite	73 ± 1.5	

(*continued on next page*)

Table 2 (*continued*)

Sample	Geologic unit and location	Long. W	Lat. N	Elevation (m asl)	Rock type	Age (Ma)	Petrography description
	Porphyry intrusion within the Socavón member, stream at the Sinaloa-Durango border						Porphyry rhyodacite. Holocrystaline with anahedral crystals (30%) of quartz (58%) > feldspar (Alk + Alb 25%) > plagioclase (An 17%) > biotite in a afanitic matrix (70%) of quartz (60%) and feldspar (10%). Strong pervasive sericite alteration in matrix, moderate turmaline and chlorite alteration in crystals and weak calcite. Two events of mineralization are presented (less than7%): 1) coarse grain of Py, Cpy, Ga, Sph and 2) fine grain of Cpy, Ga, Sph. Overgrown quartz textures are presented.
SD-004	Socavón member, Tayoltita to San Dimas road	105°55′49.12″	24°08′08.39″	1176	Lithic porphyritic rhyolitic lava	75 ± 0.77	Lithic porphyritic rhyolitic lava. Holocrystaline with anahedral to sub euhedral crystals (65%) of feldspar (Alk + Alb 57%) > quartz (31%) > plagioclase (An 12%) > hornblende > biotite in a microcrystaline matrix (35%). Rounded clast of andesites and rhyolites. Strong pervasive sericite alteration overprinted by moderate chlorite and weak calcite and turmaline. Three types of pyrite are presented: 1) broken coarse Py (less than1%), 2) fine elongate Py (less than1%) and 3) very fine anahedral Py (less than3%). Overgrown quartz textures are presented.
SD-020	Socavón member, near Piaxtla river 2 km west of Tayoltita	105°56′49.18″	24°05′23.49″	570	Quartz latite lava	75.4 ± 0.8	Quartz latite lava. Porphyritic texture, holocrystaline with medium crystals (90%) of plagioclase (An 57%) > feldspar (Alk + Alb 37%) > piroxene > anfibole > biotite > quartz (7%) in a afanitic plagioclase matrix (10%). Moderate sericite and chlorite alteration in crystals. Two types of pyrites are presented: 1) fine anahedral grains (less than1%) and 2) very fine pyrite in inclutions in the former pyrite (less than1%), coarse anahedral chalcopyrite is also presented less than 1%.
MN-14_24b	Mala Noche drillhole. This rock is observed intruding the whole drilling	105°44′47.981″	23°54′15.923″	1038	Px-rich porphyritic quartz latite	75.5 ± 1.0	Porphyritic quartz latite. Holocrystaline, medium to fine anahedral crystals of feldspar (Alk + Alb 45%) > plagioclase (An 37%) > quartz (18%) > piroxene > biotite. Strong pervasive sequndary biotite alteration overprinted by moderate pervasive calcite and sericite. Coarse anahedral pyrite is presented less than 3% and Fe oxides in pots. Quartz rapakibi texture was found.
MN-14_24	Mala Noche drillhole.	105°44′47.95″	23°54′15.906″	950	Andesitic lava	76.06 ± 0.63	Andesitic lava. Sequential porphyritic texture. Holocrystaline with sub euhedral to anahedral crystals of plagioclase (An 81%) > feldspar (Alk + Alb 13%) > quartz (7%) > hornblende in a matrix of fine anahedral plagioclase. Strong pervasive calcite alteration overprinted by moderated sericite and chlorite. Coarse anahedral pyrite is less than 4%, Fe oxides lower than 1%. Overgrown quartz textures are presented.
CAU-16_001	Causitas drillhole. This rock includes clast of the whole sequence. Dated as detrital	105°4656.21″	24°058.24	2358	Lithic rhyodacite lava	76.5	Lithic rhyodacite lava. Sequential porphyritic texture. Holocrystaline with anahedral crystals of quartz (61%) > feldspar (Alk + Alb 23%) > plagioclase (An 16%) > biotite in a microcrystaline quartz matrix. Rounded lithic fragments of andesites and quartz agregates. Strong pervasive sericite alteration is overprinted by moderate chlorite and calcite alteration. Coarse euhedral pyrite and Fe oxides are less than 2% pervasive. Overgrown quartz textures are presented.
CS-01	Lava hosting the an epithermal vein at Causita.	105°46′58.50″	24° 0′59.08″	2518	Lithic rhyodacite ignimbrite	77.73 ± 0.88	Lithic rhyodacite ignimbrite. Caotic porphyritic texture. Hialocrystaline with crystals of quartz (61%) > plagioclase (An 25%) > feldspar (Alk + Alb 15%) > biotite. Strong, pervasive sericite alteration. Rounded lithic clasts of quartz agregates. Coarse, euhedral pyrite is also present less than 1%.

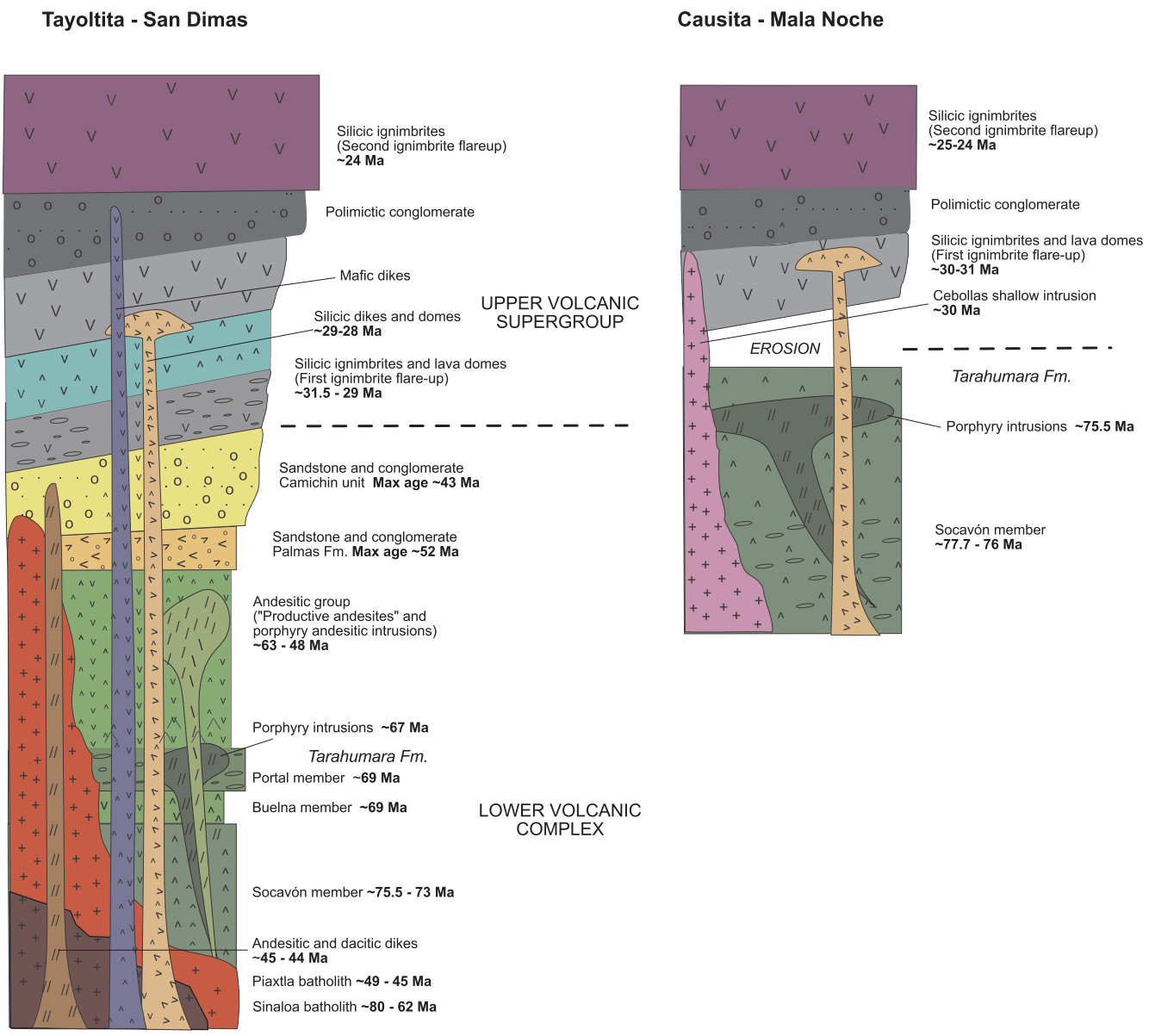

Fig. 10. New stratigraphic columns for the San Dimas and Causita-Mala Noche areas based on fieldwork and U-Pb geochronology presented in this work.

45.2 ± 0.85 Ma (SD 101, SD 040), with the older age belonging to the westernmost sample (Fig. 6).

Several dike families associated with the Piaxtla batholith cut the Late Cretaceous volcanic succession, the Andesite Group and, sometimes, the main Piaxtla body. Although they are known by different names they have similar crosscutting relationships, intermediate composition, and only differ in texture and relative mineral abundances. The Santa Lucia dikes are exposed in the Santa Rita mine intruding E-W striking fractures that crosscut a massive porphyry andesite. The dike is a porphyritic andesite, composed of medium to fine phenocrystals of plagioclase > quartz > hornblende > pyroxene and biotite in a fine plagioclase groundmass. Santa Rita dikes are found in many areas of the district also intruding E-W striking fracture. They consist of porphyry andesite with medium to coarse phenocrystals of plagioclase > quartz, but richer in pyroxene and hornblende than the Santa Lucia. The Bolaños dikes are also intruded into E–W-striking fractures, have a dacitic composition and are also rich in pyroxene and hornblende, with the latter showing coarse phenocryst texture. The U-Pb age support the field observation that all these dikes belong to the same magmatic pulse as the Piaxtla batholith, with the Santa Lucia slightly older than Santa Rita and Bolaños dikes. As mentioned before two Santa Lucia dikes yielded ages indistinguishable within the error clustered at ~48 Ma (SD 065-1, SD 080) (Fig. 6). Samples from the Santa Rita dikes and Bolaños dikes also yielded identical ages (within error) of ~45 Ma (SD 32, SD 23) (Fig. 6).

4.2.5. Sedimentary formation

Two sedimentary formations have been recognized separating the LVC from the UVS. The Las Palmas formation is composed by conglomerates, sandstones, red beds and mudstones. The Las Palmas formation lies unconformably on the Andesite Group in eastern part of the district. The Camichin formation crops out in the eastern part of the district (Santa Rita mine and Guarisamey area), ranging in thickness between 50 and 300 m. It has been described as an alternating sequence of andesitic tuffs and volcano-sedimentary deposits, but in the field, we only observed the latter lithology. We have dated detrital zircons from both units (Fig. 7). For the Las Palmas formation (SD 031) we obtained a maximum age of deposition of 52.1 ± 1.4 Ma with peaks at ~56 and ~64 Ma. A sample from the Camichín formation previously mapped as a tuff turned out to be a sandstone (SD 029), which yielded a maximum

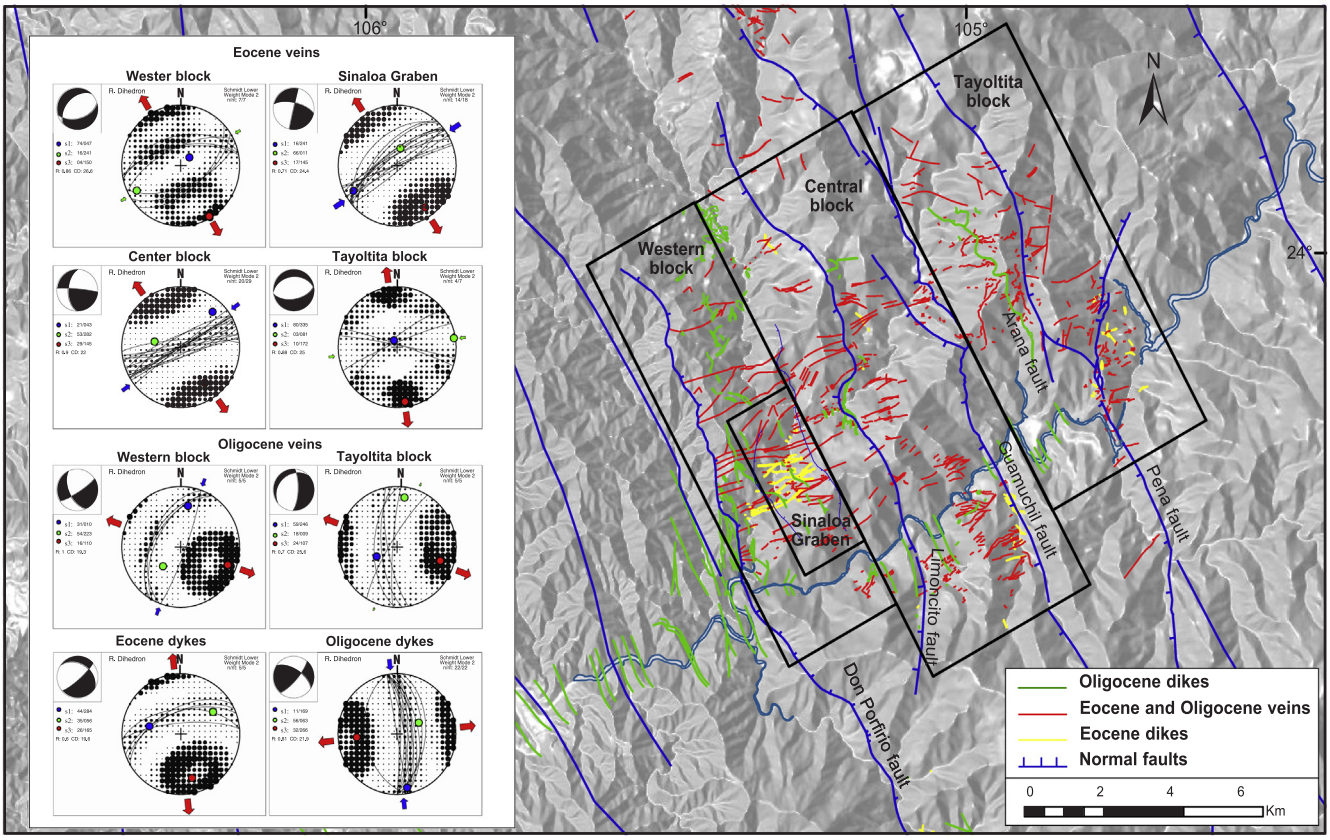

Fig. 11. Structural map of San Dimas mining district showing the mains fault systems, veins, and dikes, with stereograms showing their orientation (lower hemisphere).

depositional age of 43.2 ± 2.3 Ma with a major peak at ~56 Ma. These peaks in detrital zircons age at the beginning and end of Paleocene point to important magmatic pulses that will be discussed later.

4.2.6. *Upper volcanic supergroup*

Unconformably covering the continental sedimentary formations and the Andesite Group are two packages of silicic ignimbrites and domes, with intercalation of minor amount of mafic lavas, fed by dikes of bimodal composition. A volcanic conglomerate and an angular unconformity separate the two packages. The base of the UVS is clearly exposed along the Piaxtla River near Guarisamey, where the homonymous member it is composed by a rhyolitic ignimbrite and a series of andesitic lavas. The ignimbrite contains feldspar > plagioclase > quartz as the main crystals in the glassy matrix. The andesite lavas have a holocrystalline porphyritic texture with subhedral plagioclase phenocrystals and rare quartz. We obtained an age of 31.5 ± 0.8 Ma for the first ignimbrite capping the sedimentary formation (SD 035) and an age of 31.0 ± 1.0 Ma for the andesite agglomerate that lies just above (SD 034). This latter unit displays a large population of zircons with ages of the Piaxtla intrusive suite, which were considered as inherited xenocrystals (Fig. 8). Despite being based on four crystals only, we consider our U/Pb age reliable since the andesite flow lies in direct contact with the ignimbrite dated 31.5 Ma and no paleosoil was observed in between. The difference with the ~24 Ma K–Ar age reported by Enríquez and Rivera (2001b) for this unit is likely due to the fact that the andesite is highly altered, which may have resulted in Ar loss. A shallow granitic intrusion 10 km to the SSE of Guarisamey yielded an age of 31.3 ± 0.50 Ma (CB 01), which suggests it represents an intrusive equivalent of the first ignimbrite package. Henry et al. (2003) reported similar K–Ar dates on biotite for a granodiorite and a quartz diorite dike about 10 km to the north, in the Piaxtla river valley. Rhyolitic domes that cover the flat-lying ignimbrite succession NE of San Dimas are undated. However, we have dated a rhyolite flow that rest unconformably over the San Ignacio batholith west of the district at 29 ± 0.54 Ma, an age very similar to that obtained by K-Ar by McDowell and Keizer (1977) and by U/Pb by Ferrari et al. (2013) for the massive rhyolite dome of Las Adjuntas, located 55 km southeast of San Dimas.

NNW–SSE-striking felsic and mafic dikes cut most of the succession of the district. The felsic dikes are locally known as “Rebo” and consists of pyroclastic intrusions rich in quartz > plagioclase > biotite in a glassy matrix. These dikes are particularly abundant in the proximity of the fault system at the western limit of the district (Don Porfirio fault) at La Puerta (Fig. 11). A sample from one of these dikes at this location yielded an age of 27.0 ± 1.0 Ma (SD 102) (Fig. 8). The mafic dikes are locally known as “San Luis” and consist of basaltic lavas with porphyritic texture and plagioclase phenocrystals in a microlithic groundmass. The K-Ar age of 29.5 ± 0.7 Ma reported by Henry and Fredrikson (1987) for an andesitic dike west of the district is probably representative for these intrusions. For the ignimbrite succession that cover the Oligocene ignimbrites in angular unconformity we obtained an age of 26.2 ± 0.29 Ma. For this sample, we exclude a Pb loss as there is no correlation between higher U content and younger ages (Fig. 8). In addition, this sample belongs to an ignimbrite overlaying a conglomerate and lays in angular unconformity with the first ignimbrite package. The slightly older age obtained with respect to the correlative El Salto-Espinazo del Diablo succession (24–23.5 Ma; McDowell and McIntosh, 2012) may be due to subtle zircon inheritance in the form of antecrysts, as it is quite common for this ignimbrite package in other part of the Sierra Madre Occidental (Bryan et al., 2008; Ferrari et al., 2013). Enríquez and Rivera (2001b) report a K–Ar age of 20.3 ± 0.8 Ma for the uppermost ignimbrite of the capping sequence

NW of Guarisamey (Fig. 3). This age, obtained on plagioclase, is uncommon for the region, where the second ignimbrite flareup only consist of the 24–23.5 Ma El Salto–Espinazo del Diablo succession. The younger age can be due to Ar loss, taking into account that the closure temperature of plagioclase can be as low as 200 °C (e.g. Cassata and Renne, 2013).

5. Tectonics

As described in Section 2.2, the tectonic setting of the San Dimas district is dominated by major tilted blocks separated by NNW striking normal fault system that expose the mineralization (Fig. 10). The Limoncito, Guamuchil, and the Arana faults, located in the central and eastern part of the district, dip to the WSW with inclination varying from 80° to 55°, the Don Porfirio fault dip toward the ENE with a high angle and the Peña fault is almost vertical. Rocks in the Tayoltita and Central blocks are typically tilted 30–35° to the ENE, whereas in the Western block they are tilted 10–15° to the WSW. Most mineralized veins (61 mapped structures) strikes E–W to ENE–WSW, with only a few in the easternmost part of the district (Tayoltita block) striking ~N–S (5 mapped structures) and in the western block striking NNE–SSW (5 mapped structures) (Fig. 10).

The E–W to ENE–WSW striking veins formed before the Oligocene, as they do not cut the UVS and are exposed by the NNW striking normal fault systems. However, they almost did not change their inclination because are approximately orthogonal to the tilting. These veins cut the Late Cretaceous volcanic succession and the Andesite group, and some also cut the oldest part of the Piaxtla batholith (El Cristo granite) dated at ~49 Ma. Based on these crosscutting relations the veins can be limited to the late Eocene. Our ~45 Ma ages for the "Santa Rita" and "Bolaños" dikes (Table 1), whose strike is parallel to the veins, suggest that they could be part of the same episode. Recent Ar–Ar dating of adularia (Enriquez et al., 2018) points to a slightly younger age of ~41 Ma. The associated stress regime would have been characterized by NW–SE σHmin and NE-SW σHmax, with a possible transtensional deformation regime in some areas, as observed by Horner and Enriquez (1999) (Fig. 10).

NNW striking normal faults and block tilting post-date the first ignimbrite package of the UVS. However, the angular unconformity and the conglomerate that separate it from the second ignimbrite package indicate that faulting occurred between ~30 and ~24 Ma, as it has documented in several areas of Sinaloa (Ferrari et al., 2013). This is also confirmed by the 27.0 ± 1.0 Ma age we obtained for a felsic dike intruded parallel to and in proximity of the NNW striking Don Porfirio fault system (Fig. 10) (SD 102, Table 1). Taking into account this age, the crosscutting relations, and the fact that they are only moderately tilted, we consider NNW–SSE to N–S striking veins and dikes as emplaced during the initial stage of the Oligocene extension. Assuming that the veins and dikes were the result of a pure extensional opening, they would indicate an ~E–W to WNW–ESE extension regime (Fig. 10) that have been also reported for the western SMO at the beginning of the Gulf of California rift (Ferrari et al., 2013, 2017; Duque-Trujillo et al., 2015). Further west, the ignimbrite package of the second ignimbrite flareup is also tilted (Henry, 1989; Henry and Fredrikson, 1987; Henry and Aranda-Gómez, 2000), implying that a second extensional episode affected this area.

The result of AFT dating on two samples at different altitudes of the Piaxtla batholith provide further support to this multiple-stage extensional history (Fig. 9). The dated samples show consistent cooling ages with a first group of ages at the end of Oligocene (24.7 ± 1.9 and 23.3 ± 1.9 Ma) and a second one at the end of middle Miocene (12.6 ± 1.2 and 12.4 ± 1.1 Ma).

On a larger scale, our new mapping and absolute dating south of the district point to a major structure roughly parallel to the Piaxtla river. In fact, the Late Cretaceous volcanic succession lies at a maximum of ~1500 m of elevation in the San Dimas area whereas it crops out at ~2600 m in the Causita area to the SSE (Fig. 3). The easiest explanation for a difference of ~1100 m of elevation between the San Dimas and Causita blocks is the presence of a major ENE–WSW striking and NNW dipping normal fault system running somewhere in the Piaxtla river valley, here named Piaxtla fault zone. A structure with this orientation but opposite dip (i.e. down to the SSE) is drawn some km south-southeast of the river in the geologic map of Henry and Fredrikson (1987) but not described. In the field, no clear fault zone is observed in Piaxtla riverbed, which between Tayoltita and San Ignacio is always cut into the Piaxtla granite. We infer that this fault system is older than the ~32 to 30 Ma ignimbrites and thus buried beneath them. In Fig. 3 we draw this inferred normal fault system along the trace drawn by Henry and Fredrikson (1987) but we assume that it has an opposite displacement.

In the Tayoltita area the intrusion contact of the Piaxtla batholith in the NNW side of the valley has a lower elevation with respect to the SSE side, which suggest that the batholith may have intruded into a pre-existing normal fault zone. If extended toward the west the Piaxtla fault zone would limit a WSW-ENE trending horst of the pre-Laramide basement that crop out along the coast between Mesa Cacaxtla and Mazatlán but not to the north and to the south (Fig. 2). On a regional scale is very possible that other fault systems orthogonal to the Gulf of California may exists and controlled the segmentation of the rift in the following extensional stage. This structural grain may be inherited from even older deformation episodes. Henry (1986) reported ENE trending folds and thrust faults, orthogonal to the paleo-subduction zone in Jurassic to Early Cretaceous rocks in Sinaloa, that would have formed by oblique convergence prior to 100 Ma.

6. Discussion and conclusion

6.1. Revision of the San Dimas district stratigraphy

Our new ages and geologic observations provide tighter constraints on the magmatic and mineralization pulses in the San Dimas district and allow to correlate its stratigraphy with other regions of the SMO. One of the main contributions is the recognition of the presence of a Late Cretaceous volcanic activity in the area. Previous studies were unable to date the LVC succession. Some workers suggested that it was older than the Piaxtla intrusive complex (Henshaw, 1953; Nemeth, 1976; Henry and Fredrikson, 1987; Enríquez and Rivera, 2001b) but mostly Eocene in age, by correlation with andesites dated at 51.6 Ma south of Durango by McDowell and Keizer (1977). The ages of the Socavón, Buelna, and Portal members obtained in this work clearly demonstrate that these rocks are part of the Late Cretaceous magmatic episode of the so-called Laramide arc. In particular, they share the same time span, lithology and composition of the Tarahumara formation of Sonora (Wilson and Rocha, 1949; McDowell et al., 2001). As in Sonora this Late Cretaceous volcanic succession is exposed to the east of the age-equivalent Laramide batholiths (Fig. 2), which suggest a wider volcanic arc that was eroded toward the coast.

For the following Andesite group Enríquez and Rivera (2001b) reported ages between 38.8 and 36.6 Ma using the K–Ar method. Based on these ages, the authors linked the andesitic magmatism with the epithermal mineralization events, which produced similar ages (38.5–31.9 Ma). Given the widespread alteration of these rocks these ages are unreliable and contradicts our new U-Pb ages and crosscutting relations. In fact, we obtained a few zircons of early Paleocene age for the "Intrusive andesite" and, more importantly, two reliable U-Pb ages of ~48 Ma for intrusive bodies that cut the Andesite group. Therefore, we have relocated this group in the Paleocene to Early Eocene. In this context we consider that the K-Ar ages of Enríquez and Rivera (2001b) were the result of partial resetting of the dated minerals.

We observed that the Piaxtla intrusive complex intrude the whole LVC from the base to the top and was formed by different magmatic pulses, separated based on texture, composition and age. Our U/Pb age

confirm earlier K–Ar and U/Pb ages (Enríquez and Rivera, 2001b; Henry et al., 2003) and show that the development of the batholith took place in several millions of years from ~49 to ~44 Ma. A novel contribution is the dating of the "Santa Rita" and "Bolaños" intermediate dikes, that were previously thought to be somewhat younger than the Piaxtla suite but turned out to be concurrent with the last intrusion stage. These ages are relevant because document a period of ~13 Ma without any magmatic activity in the area, during which previous authors suggested the occurrence of a mineralization event.

The occurrence of the continental sedimentary Las Palmas and Camichín formations points to an early stage of extension with the formation of intermontane basins in the Eocene. The rock fragments and different zircon populations indicate that these clastic units were mostly derived from volcanic edifices (domes and compound volcanoes) that form the Andesite Group and, to a lesser extent, the Piaxtla intrusive suite, most likely the Santa Rita and Bolaños dikes. A continental sedimentary deposits lithologically equivalent to the Las Palmas formation and in the same stratigraphic position is reported south of the San Dimas district in the Mala Noche area (Servicio Geológico Mexicano, 2002), where it is called "Palmarito conglomerate". At a regional level it can be correlated with many discontinuous continental sedimentary deposits that mark a period of the erosion and low volcanic activity between the bulk of LVC and the UVS (McDowell and Keizer, 1977; McDowell and Clabaugh, 1979; Ferrari et al., 2007).

The new U/Pb ages for the base of the ignimbrite succession at San Dimas are consistent with those of the Durango sequence, whose Ar–Ar ages range from 31.7 to 29.9 Ma (McDowell and McIntosh, 2012). A slightly older age of 32.5 Ma was obtained by Ferrari et al. (2013) for a tilted ignimbrite sequence east of Mala Noche. This confirms that the eastward prolongation of the Durango sequence at least up to the Durango–Sinaloa state boundary.

6.2. Timing of igneous activity

Henry et al. (2003) interpret that igneous activity was mostly continuous between ~100 and 45 Ma in Sinaloa. Although at a regional level some ages of igneous bodies fall between ~61 and ~49 Ma and our detrital zircons show a peak in this age interval, along the Piaxtla river valley a distinction can be clearly made between the San Ignacio and the Piaxtla batholiths. Along the river, we observe a clear change in morphology (much less relief) and increase in alteration (intrusive rocks often reduced to sand) and mineral composition (mafic minerals more abundant) between the two batholiths. Ages also change rather abruptly (Fig. 2). The Piaxtla batholith is exposed for ~35 km to the northeast of the contact with ages restricted between 49.6 and 43.7 Ma, whereas the San Ignacio batholith has ages between ~67 and ~61 Ma to the southwest (Henry et al., 2003, this work). Supporting this inference, sample 199 of Henry et al. (2003), from what we mapped as the Piaxtla batholith, is a tonalite that yielded a biotite age of 49.3 ± 0.6 Ma; however, just 2 km to the south sample 152 of Henry et al. (2003) is a granodiorite that yielded a hornblende age of 67.1 ± 1.5 Ma. Interestingly, this same sample yielded a biotite age of 51.3 ± 0.6 Ma, a large difference of 16 Ma that cannot be due to normal cooling but rather to a thermal resetting of the biotite system due to the nearby Piaxtla intrusion. Our new ages also confirm a gap in igneous activity between ~43 Ma (youngest age of the Piaxtla intrusive suite) and ~32 Ma (first ignimbrite of the UVS), which is also marked by the deposition of the Las Palmas and Camichín sedimentary successions.

6.3. Implication for the mineralization events at San Dimas

A detailed structural, geochemical and geochronologic study of the vein system is the focus of a forthcoming paper. However, the data presented in this work provide some constraint on the mineralization events of the San Dimas district. San Dimas has been traditionally classified as a classic Au–Ag epithermal low sulfidation vein system developed during a single mineralization episode during in a late stage of the LVC magmatism (Henshaw, 1953; Smith and Hall 1974; Smith et al., 1982; Clarke, 1986; Clarke and Titley, 1988). Enríquez and Rivera (2001b) obtained similar Late Eocene K–Ar ages for andesitic intrusions and some of the veins, which led them to associate the two events and conclude that the mineralization occurred in the ~38 to 32 Ma time span. However, the minerals dated by these authors were adularia and feldspar, whose closure temperature for the K– Ar system (~150 to 200 °C; Love et al., 1998) is well below the temperature of the hydrothermal fluids circulating in the district (~260 °C; Clarke and Titley, 1988). This means that the late Eocene ages of Enríquez and Rivera (2001b) should be considered minimum ages, likely resulting from partial resetting.

In this work we have dated the main geologic units of San Dimas using zircon, whose closure temperature for the U/Pb system (~900 °C) is much higher than the temperature of any hydrothermal fluid. Our data place the Andesite Group into the Paleocene–early Eocene time span, as it is also confirmed by the age peaks in the continental sedimentary deposits of the Las Palmas formation. Although we did not directly date the mineralization, the most important magmatic event postdating the host rock of the Andesite Group is the Piaxtla intrusive suite, emplaced between ~49 and ~44 Ma, which we consider the most likely thermal source for the dominant ENE-WSW trending vein system. These veins occupied fractures and faults that developed before the first ignimbrite flare up of the UVS that may have also controlled the emplacement of the Piaxtla batholith. Recently, Enriquez et al. (2018) obtained Ar–Ar ages of 41 ± 0.2 and 37.8 ± 0.2 Ma on adularia from two veins of the E–W system with high Ag/Au ratio. The first age confirms the K–Ar age of 40.9 Ma on adularia from an undefined mine at Tayoltita obtained by Henry et al. (2003). The new Ar–Ar ages show a well-defined plateau, and indicate that at least part of the Ag/Au mineralization occurred ~3 to 6 Ma after the emplacement of the Piaxtla intrusive suite.

On the other hand, NNW–SSE to N–S veins emplaced in the eastern part of the district must be associated with the similarly oriented normal faults responsible for the block tilting in the San Dimas area. As mentioned in the previous section, these extensional faults are partly coeval with the silicic volcanism of the flare up dated at ~32 to 29 Ma. If this is the case, the NNW–SSE to N–S veins should differ from the rest of the district in term of Ag/Au ratio and other structural and chemical features. In conclusion, the data presented in this work show that the San Dimas district was developed during multiple mineralization events tied to magmatic and tectonic pulses that affected the central part of the Sierra Madre Occidental.

Acknowledgements

This research is part of the PhD project of the first author at Universidad Nacional Autónoma de México (UNAM) Postgraduate Program and was funded by Consejo Nacional de Ciencias y Tecnología (CONACYT), Mexico, Grant CB 237745-T to L. Ferrari. We thank Primero Mining (presently First Majestic Silver Corp.) for sharing unpublished information and for logistical support. We thank Chris Henry for his thorough review that contribute to clarify several aspects of the work and two anonymous reviewers that helped to improve its presentation. A special thanks to Nicolas Landón for his strong support in the initial phase of the research and to Miguel Pérez for sharing his knowledge of the ore geology of the central SMO. We also thank Luigi Solari and Carlos Ortega for assistance with U-Pb datings and Juan Tomás Vazquez for the elaboration of thin sections.

Appendix A. Supplementary data

Supplementary data to this article can be found online at https://doi.org/10.1016/j.oregeorev.2018.12.020.

References

Abdullin, F., Solari, L., Ortega-Obregón, C., Solé, J., 2018. New fission-track results from the northern Chiapas Massif area, SE Mexico: trying to reconstruct its complex thermo-tectonic history. Rev. Mex. Cienc. Geol. 35 (1), 79–92.

Albinson, T., Norman, D.I., Cole, D., Chomiak, B., 2001. Controls on formation of low sulfidation epithermal deposits in Mexico: constraints from fluid inclusion and stable isotope data. In: New Mines and Discoveries in Mexico and Central America 8. Society of Economic Geology Special Publication, pp. 1–32.

Ballard, S., 1980. Structural geologic controls at the San Luis mines, Tayoltita, Durango, Mexico (Unpublished M.A. Thesis).

Bonneau, M., 1970. Una nueva área Cretácica fosilífera en el estado de Sinaloa. Bol. Soc. Geol. Mexic. 32, 159–167.

Bryan, S., Ferrari, L., 2013. Large igneous provinces and silicic large igneous provincies: progress in our understanding over the last 25 years. Geol. Soc. Am. Bull. 125, 1053–1078.

Bryan, S.E., Ferrari, L., Reiners, P.W., Allen, C.M., Petrone, C.M., Ramos-Rosique, A., Campbell, I.H., 2008. New Insights into crustal contributions to large-volume rhyolite generation in the mid-Tertiary Sierra Madre Occidental Province, Mexico, revealed by U-Pb geochronology. J. Petrol. 49, 47–77.

Camprubí, A., 2013. Tectonic and Metallogenic History of Mexico. Soc. Econ. Geol. Spec. Publ. 17, 201–243.

Camprubí, A., Albinson, T., 2007. Epithermal deposits in México — update of current knowledge, and an empirical reclassification. Geol. Soc. Am. Spec. Pap. 422, 377–415.

Cassata, W.S., Renne, P.R., 2013. Systematic variations of argon diffusion in feldspars and implications for thermochronometry. Geochim. Cosmochim. Acta 112, 251–287.

Clarke, M., 1986. Hydrothermal geochemistry of Ag-Au veins in the Tayoltita and the San Dimas mining district, Durango and Sinaloa, Mexico (Unpublished Ph.D. dissertation). p. 151.

Clarke, M., Titley, S., 1988. Hydrothermal evolution in the formation of silver-gold veins in the Tayoltita mine, San Dimas district, Mexico. In: New Mines and Mineral Discoveries in Mexico and Central America 8. Society of Economic Geologists Special Publications, pp. 1830–1840.

Campa, M.F., Coney, P.J., 1983. Tectono-stratigraphic terranes and mineral resource distributions in Mexico. Can. J. Earth Sci. 20, 1040–1051.

Damon, P.E., Shafiqullah, M., Clark, K.F., 1981. Evolución de los arcos magmáticos en México y su relación con la metalogénesis. Rev. Mexic. Cienc. Geol. 5, 223–238.

Damon, P., Shafiqullah, M., Clark, K., 1983. Geochronology of the porphyry copper deposits and related mineralization in Mexico. Can. J. Earth Sci. 20, 1052–1071.

Davidson, S., 1932. Geology and ore deposit of Tayoltita, district of San Dimas, Durango, Mexico (Unpublished PhD thesis). p. 172.

Donelick, R.A., O'Sullivan, P.B., Ketcham, R.A., 2005. Apatite fission-track analysis. Rev. Mineral. Geochem. 58 (1), 49–94.

Duque-Trujillo, J., Ferrari, L., Orozco-Esquivel, T., López-Martínez, M., Losndale, P., Bryan, S., Kuesner, J., Piñero-Lajas, D., Solari, L., 2015. Timing of rifting in the southern Gulf of California and its conjugated margins: insight from the plutonic record. Geol. Soc. of Am. Bull. 127, 702–736.

Enriquez, E., Rivera, R., 2001a. Geology of the Santa Rita Ag-Au Deposit, San Dimas District, Durango, Mexico. In: New Mines and Mineral Discoveries in Mexico and Central America 8. Society of Economic Geologists Special Publication, pp. 39–58.

Enríquez, E., Rivera, R., 2001b. Timing of magmatic and hydrothermal activity in the San Dimas District, Durango, Mexico. In: New Mines and Mineral Discoveries in Mexico and Central America 8. Society of Economic Geologist Special Publication, pp. 33–38.

Enriquez, E., Iriondo, A., Camprubí, A., 2018. Geochronology of Mexican mineral deposits. VI: the Tayoltita low-sulfidation epithermal Ag-Au district, Durango and Sinaloa. Bol. Soc. Geol. Mexic. 70, 531–547.

Ferrari, L., Rosas-Elguera, J., 2000. Late Miocene to Quaternary extension at the northern boundary of the Jalisco block, western Mexico: the Tepic-Zacoalco rift revised. Geol. Soc. Am. Spec. Pap. 334, 41–64.

Ferrari, L., López-Martínez, M., Rosas-Elguera, J., 2002. Ignimbrite flareup and deformation in the southern Sierra Madre Occidental, western Mexico-implications for the late subduction history of the Farallon Plate. Tectonics 21, 1035 10.1029/2001TC001302.

Ferrari, L., López-Martínez, M., Orozco-Esquivel, T., Bryan, S.E., Duque-Trujillo, J., Lonsdale, P., Solari, L., 2013. Late Oligocene to Middle Miocene rifting and synextensional magmatism in the southwestern Sierra Madre Occidental, Mexico: the beginning of the Gulf of California rift. Geosphere. https://doi.org/10.1130/GES00925.1.

Ferrari, L., Orozco-Esquivel, T., Bryan, S., Lopez-Martínez, M., Silva Fragoso, A., 2017. Cenozoic extension and magmatism in western Mexico: linking the Sierra Madre Occidental Silicic Large Igneous Province and the Comondú Group with the Gulf of California rift. Earth-Sci. Rev. 183, 115–152.

Ferrari, L., Valencia-Moreno, M., Bryan, S., 2007. Geology of the western Mexican volcanic belt and adjacent Sierra Madre Occidental and Jalisco block. Geol. Soc. Am. Spec. Pap. 334, 65–83.

Folk, R.L., 1974. Petrology of Sedimentary Rocks. Hemphill Publishing Company, Texas.

Gans, P., 1997. Large-magnitude Oligo-Miocene extension in southern Sonora: implications for the tectonic evolution of northwest Mexico. Tectonics 16, 388–408.

Gastil, P., 1975. Plutonic zones in the Peninsular Ranges of southern California and northern Baja California. Geology 3, 361–363.

Goldoff, B., Webster, J.D., Harlov, D.E., 2012. Characterization of fluor-chlorapatites by electron probe microanalysis with a focus on time-dependent intensity variation of halogens. Am. Mineral. 97, 1103–1115.

González León, C.M., McIntosh, W.C., Lozano-Santacruz, R., Valencia-Moreno, M., Amaya-Martínez, R., Rodríguez-Castañeda, J.L., 2000. Cretaceous and Ter- tiary sedimentary, magmatic, and tectonic evolution of north-central Sonora (Arizpe and Bacanuchi quadrangles), northwest Mexico. Geol. Soc. Am. Bull. 112, 600–610.

Hasebe, N., Barbarand, J., Jarvis, K., Carter, A., Hurford, A.J., 2004. Apatite fission-track chronometry using laser ablation ICP-MS. Chem. Geol. 207 (3–4), 135–145.

Henry, C., 1975. PhD Dissertation In: Geology and geochronology of the granitic batholithic complex, Sinaloa, Mexico. University of Texas at Austin, pp. 158.

Henry, C.D., 1986. East-northeast–trending structures in western Mexico: Evidence for oblique convergence in the late Mesozoic. Geology 14 (4), 314.

Henry, C.D., 1989. Late Cenozoic Basin and range structure in western Mexico adjacent to the Gulf of California. Geol. Soc. Am. Bull. 101 (9), 1147–1156.

Henry, D., Fredrikson, G., 1987. Geology of southern Sinaloa adjacent to the Gulf of California. Geol. Soc. Am. Map Chart Ser. 14.

Henry, C.D., Aranda-Gómez, J.J., 2000. Plate interactions control middle-late Miocene proto-Gulf and Basin and Range extension in the southern Basin and Range. Tectonophysics 318, 1–26.

Henry, C., McDowell, F., Silver, L., 2003. Geology and geochronology of granitic batholithic complex, Sinaloa, México: implications for Cordilleran magmatism and tectonics. Geol. Soc. Am. Spec. Pap. 374, 237–273.

Henshaw, P.C., 1953. Geology and Ore Deposit of the San Dimas District, Sinaloa and Durango. Private document. p. 531.

Horner, J., Enriquez, E., 1999. Epithermal precious metal mineralization in a strike-slip corridor: the San Dimas District, Durango, Mexico. Econ. Geol. 94 (8), 1375–1380.

Hurford, A.J., 2019. An historical perspective on fission-track thermochronology. In: Fission-Track Thermochronology and its Application to Geology. Springer, Cham, pp. 3–23.

Le Bas, M.J., Streckeisen, A.L., 1991. The IUGS systematics of igneous rocks. J. Geol. Soc. 148, 825–833.

Le Maitre, R.W., Streckeisen, A., Zanettin, B., Le Bas, M.J., Bonin, B., Bateman, P., et al., 2002. In: Igneous Rocks. A Classification and Glossary of Terms: Recommendation of the International Union of Geological Science, Subcommission on the Systematic of Igneous Rocks, Second ed. Cambridge University Press, pp. 236.

Locke, A., 1918. Unpublished report In: Geologic atlas, San Dimas mining district, Mexico. San Luis Mining Company, Tayoltita, pp. 10.

Love, D.A., Clark, A.H., Hodgson, C.J., Mortensen, J.K., Archibald, D.A., Farrar, E., 1998. The timing of adularia-sericite-type mineralization and alunite-kaolinite-type alteration, Mount Skukum epithermal gold deposit, Yukon Territory, Canada; ^{40}Ar-^{39}Ar and U-Pb geochronology. Econ. Geol. 93, 437–462.

Ludwig, K.R., 2008. Useŕs manual fro Isoplot 3.7. A geochronological toolkit for Microsoft Excel. Berkeley Geochronol. Center Spec. Publ. 4, 77.

McDowell, F.W., Clabaugh, S.E., 1979. Ignimbrites of the Sierra Madre Occidental and their relation to the tectonic history of western Mexico. Geol. S. Am. S. 180, 113–124.

McDowell, F., Keizer, R., 1977. Timing of mid Tertiary volcanism in the Sierra Madre Occidental between Durango City and Mazatlán, Mexico. Geol. Soc. Am. Bull. 88, 1479–1487.

McDowell, F., Roldán-Quintana, J., Amaya-Martínez, R., 1997. Interrelationship of sedimentary and volcanic deposits associated with Tertiary extension in Sonora, Mexico. Geol. Soc. Am. Bull. 109, 1349–1360.

McDowell, F., McIntosh, W., 2012. Timing of intense magmatic episodes in the northern and central Sierra Madre Occidental, western. Geosphere 8, 1505–1526.

McDowell, F., Roldán-Quintana, J., Connelly, J., 2001. Duration of Late Cretaceous-early Tertiary magmatism in east-central Sonora, Mexico. Geol. Soc. Am. Bull. 113, 521–531.

Montoya-Lopera, P., Levresse, G., Ferrari, L., Orozco-Esquivel, T., Hérnandez-Quevedo, G., Mata, L., submitted for publication. New geological, geochronological and geocemical characterization of the telescoped Eocene-Oligocene Ag/Au San dimas epithermal deposit, Mexico. Ore Geol. Rev.

Murray, B.P., Busby, C.J., Ferrari, L., Solari, L.A., 2013. Synvolcanic crustal extension during the mid-Cenozoic ignimbrite flare-up in the northern Sierra Madre Occidental, Mexico: evidence from the Guazapares Mining District region, western Chihuahua. Geosphere 9, 1201–1235.

Nemeth, K.E., 1976. Petrography of the Lower Volcanic Group, Tayoltita-San Dimas District, Durango, Mexico (Unpublished M.A. thesis). p. 141.

Nourse, J., Anderson, T., Silver, L., 1994. Tertiary metamorphic core complexes in Sonora, northwestern Mexico. Tectonics 13, 1161–1182.

Ortega-Gutiérrez, F., Elías-Herrera, M., Morán-Zenteno, D.J., Solari, L., Luna-González, L., Schaaf, P., 2014. A review of batholiths and other plutonic intrusions of Mexico. Gondwana Res. 26 (3–4), 834–868.

Ortega-Obregón, C., Solari, L., Gómez-Tuena, A., Elías-Herrera, M., Ortega-Gutiérrez, F., Macías-Romo, C., 2014. Permian-Carboniferous arc magmatism in southern Mexico: U-Pb dating, trace element and Hf isotopic evidence on zircons of earliest subduction beneath the western margin of Gondwana. Int. J. Earth Sci. 103 (5), 1287–1300.

Paton, C., Hellstrom, J., Paul, B., Woodhead, J., Hergt, J., 2011. Iolite: Freeware for the visualisation and processing of mass spectrometric data. J. Anal. At. Spectrom. 26 (12), 2508–2518.

Petrus, J.A., Kamber, B.S., 2012. VizualAge: A novel approach to laser ablation ICP-MS U-Pb geochronology data reduction. Geostand. Geoanal. Res. 36 (3), 247–270.

Salas, G.P., 1994. Economic geology of Mexico. In: Salas, G.P. (Ed.), Economic Geology, Mexico. Geological Society of America, Geology of North America, P-3, Boulder, Colorado, pp. 1–6.

Servicio Geológico Mexicano, 2002. Carta geológico-minera Borbollones, F13 – A17, escala 1:50,000, estados de Durango y Sinaloa (Technical Report). p. 54.

Smith, D.M., Hall, D.K., 1974. In: Geology of the Tayoltita mine, Durango, Mexico. Society of Mining Engineers of A.I.M.E, pp. 48.

Smith, D., Albinson, T., Sawkins, F., 1982. Geologic and fluid inclusion studies of the Tayoltita silver-gold vein deposit, Durango, Mexico. Soc. Econ. Geol. 1120–1145.

Solari, L.A., Gómez-Tuena, A., Bernal, J.P., Pérez-Arvizu, O., Tanner, M., 2010. U-Pb zircon geochronology by an integrated LA-ICPMS microanalytical workstation: achivements in precision and accuracy. Geostand. Geoanal. Res. 34, 5–18.
Staude, J.M.G., Barton, M.D., 2001. Jurassic to Holocene tectonics, magmatism, and metallogeny of northwestern Mexico. Geol. Soc. Am. Bull. 113 (10), 1357–1374.
Valencia, V., Righter, K., Rosas-Elguera, J., Lopez-Martinez, M., Grove, M., 2013. The age and composition of the pre-Cenozoic basement of the Jalisco Block: implications for and relation to the Guerrero composite terrane. Contrib. Miner. Petrol. 166 (3), 801–824.
Vermeesch, P., 2009. RadialPlotter: a Java application for fission track, luminescence and other radial plots. Radiat. Meas. v. 44, 409–410.
Vermeesch, P., 2017. Statistics for LA-ICP-MS based fission track dating. Chem. Geol. 456, 19–27.
Vermeesch, P., 2018. IsoplotR: a free and open toolbox for geochronology. Geosci. Front. https://doi.org/10.1016/j.gsf.2018.04.001.
Wiedenbeck, M., Alle, P., Corfu, F., Griffin, W.L., Meier, M., Oberli, F., Spiegel, W., 1995. Three natural zircon standards for U-Th-Pb, Lu-Hf, trace element and REE analyses. Geostand. Newslett. 19 (1), 1–23.
Wilson, F.O., Rocha, S., 1949. Coal deposits of the Santa Clara distric near Tónichy, Sonora, Mexico. U.S. Geol. Surv. Bull. 962A, 80.
Wong, M.S., Gans, P.B., Scheier, J., 2010. The 40Ar/39Ar thermochronology of core complexes and other base- ment rocks in Sonora, Mexico: Implications for Ceno- zoic tectonic evolution of northwestern Mexico. J. Geophys. Res. 115 (B7), B07414.

Capítulo 3: **New geological, geochronological and geochemical characterization of the San Dimas mineral system: evidence for a telescoped Eocene-Oligocene Ag/Au deposit in the Sierra Madre Occidental, Mexico**

Ore Geology Reviews 118 (2020) 103195

Contents lists available at ScienceDirect

Ore Geology Reviews

journal homepage: www.elsevier.com/locate/oregeorev

New geological, geochronological and geochemical characterization of the San Dimas mineral system: Evidence for a telescoped Eocene-Oligocene Ag/Au deposit in the Sierra Madre Occidental, Mexico

Paula Montoya-Lopera[a], Gilles Levresse[a,*], Luca Ferrari[a], Teresa Orozco-Esquivel[a,b], Gabriela Hernández-Quevedo[a,b], Fanis Abdullin[c], Luis Mata[d]

[a] Centro de Geociencias, Universidad Nacional Autónoma de Mexico, Campus Juriquilla, 76230 Querétaro, Qro, Mexico
[b] Laboratorio Interinstitucional de Geocronología de Argón (LIGAR), Campus UNAM Juriquilla, Querétaro, Mexico
[c] CONACyT-Centro de Geociencias, Universidad Nacional Autónoma de Mexico, Campus Juriquilla, 76230 Querétaro, Qro, Mexico
[d] First Majestic Silver Corp., San Dimas, Dgo., Mexico

ARTICLE INFO

Keywords:
Telescoped deposits
^{40}Ar-^{39}Ar dating
U-Pb dating
Titanite fission track dating
Zircon trace elements
Sierra Madre Occidental

ABSTRACT

The San Dimas district is a historical world class Ag/Au epithermal deposit located in the Sierra Madre Occidental (SMO) of western Mexico. San Dimas has been classified as a classic low to intermediate sulfidation Ag/Au epithermal deposit (quartz + adularia + sericite type) developed during a single hydrothermal pulse of ~10 Ma, associated to the emplacement of intermediate intrusive bodies of Eocene K-Ar ages. However, this metallogenetic model includes several ambiguities, such as K-Ar cooling ages incompatible with the local and regional magmatic pulses, as well as wide differences in Ag-Au ratios between individual veins, which were also emplaced in two different structural systems. Based on a detailed study of mineralized veins, including new petrographic observations, new geochronological data (zircon U-Pb, adularia ^{40}Ar/^{39}Ar, and titanite fission track ages, FT), zircon trace-element composition, and geochemistry of gold and silver minerals, we demonstrate that San Dimas exhibits multiple mineralization events developed during different magmatic and tectonic episodes from Late Cretaceous to early Oligocene. The earliest episode is represented by Late Cretaceous copper – gold porphyry mineralization associated with fertile and oxidized magmas during the development of the Laramide arc. The second, most abundant ore mineralization is represented by a Ag-dominant vein system (adularia + rhodochrosite type), which developed into east-west striking fractures. New ^{40}Ar/^{39}Ar ages on adularia as well as new titanite FT ages for this mineralization event, together with one published ^{40}Ar/^{39}Ar age indicate the formation of Ag rich veins at ~41–40 Ma, shortly after the final emplacement of the Piaxtla batholith (~45 Ma), which formed from multiple fertile and oxidized magma intrusions in an extensional environment. The third mineralization episode is represented by Au-dominant epithermal veins (quartz sericite type), which were emplaced at ~31 Ma into north-south to NNE-SSE striking fractures. At regional scale these fractures also host rhyolitic domes associated with the first silicic ignimbrite flare up of the SMO in an extensional setting. The formation of the San Dimas district with its exceptionally rich Ag-Au mineralization is interpreted to be related to an extension-related late Eocene-early Oligocene regional uplift that allowed the overprinting of originally deeper Ag veins by a shallower Au mineralizing event.

1. Introduction

Mexico has a special place in the precious metals mining industry as it is presently the largest silver producer in the world (Silver Institute, 2017). The size of the Mexican silver and gold anomaly is illustrated by the outstanding role of Mexico mining during XVI and XVII centuries and its position during last ten years as the largest silver (200 Moz/year) and eighth largest gold (125 ton/year) producer worldwide. Most of this production comes from localities within the Sierra Madre Occidental province (SMO; Fig. 1). The timing of formation of epithermal deposits coincides with the distribution of the products of the three main Cenozoic volcanic pulses of the SMO, which record a broad migration from the northwest to the southeast, where the last ignimbrite flare-up occurred (Ferrari et al., 2007; Ramos-Rosique et al., 2011;

* Corresponding author.
E-mail address: glevresse@geociencias.unam.mx (G. Levresse).

https://doi.org/10.1016/j.oregeorev.2019.103195
Received 29 March 2019; Received in revised form 18 October 2019; Accepted 22 October 2019
Available online 28 October 2019
0169-1368/

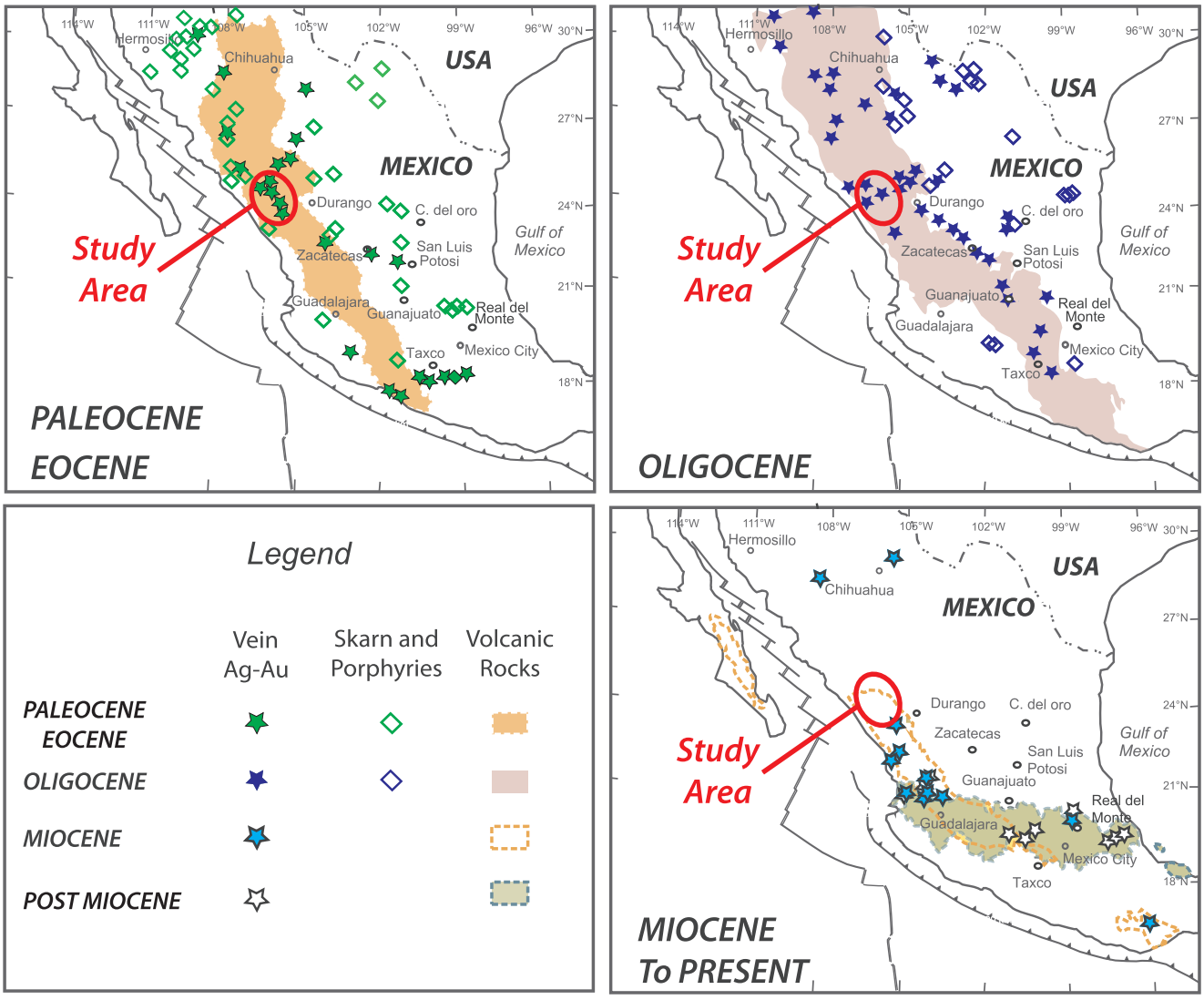

Fig. 1. Distribution of dated Mexican hydrothermal, skarn, porphyries and orogenic gold deposits from Eocene to recent (modified from Camprubi, 2013). Color shadows indicate the distribution of volcanic rocks of Paleocene-Eocene, Oligocene, early Miocene and recent ages (modified from Ferrari et al., 2012).

Fig. 1). The most fertile magmatic ore-forming events range in age from 36 to 28 Ma and include all the giant Ag-Au-Sn and IOCG mining districts (Camprubí et al., 2003). The increasing comprehension of the genesis of historical Ag/Au districts in the SMO (e.g., San Dimas) is modifying several concepts central to the epithermal mineralization topic, such as the formation of Ag/Au deposits (Hayba et al., 1985; Simmons, 1991; Sillitoe, 1993), the classification into high, intermediate, and low sulfidation deposits (Sillitoe, 1993; Arribas et al., 1995; Camprubi and Albinson, 2007), and the existence of long-living hydrothermal events (Enriquez and Rivera, 2001; Camprubí et al., 2003; Velador et al., 2010; Enríquez et al., 2018), among others. The Mexican epithermal deposits are characterized by extremely variable Ag/Au ratios. These variations are observed from regional (i.e., among districts) to local scale, and might be even found within a single mineralized structure (Buchanan, 1980; Hayba et al., 1985; Sillitoe, 1993; Velador et al., 2010; Camprubí et al., 2003; Hall et al., 2014). At a regional scale, this variation has been interpreted to be related to crustal thickness (Camprubi and Albinson, 2007). At a local scale, authors agree that Ag/Au ratio variations in epithermal deposits are mainly controlled by boiling and water/rock interaction. The latter physicochemical processes lead to changes in temperature, pH, fS_2 and/or fO_2 over time, which affect the transportation and deposition of gold and silver in hydrothermal fluids (Hynes, 1999; Enriquez and Rivera, 2001a; 2001b; Camprubi and Albinson, 2007; Velador et al., 2010; Moncada et al., 2012; Camprubí et al., 2003; Mango et al., 2014; Hall et al., 2014; Enríquez et al., 2018). However, Cole and Drummond (1986) estimated that the Ag/Au ratio variation related to boiling process ranges from 10 to 100, which, despite being conservative, cannot explain Ag/Au ratio variations within a single structure.

A widely used classification divides epithermal deposits of Mexico into subtypes with different sulphidation state (Albinson and Camprubí, 2007). The geologic context of low sulfidation and high sulfidation Ag-Au epithermal deposits is well characterized and their relationship with rhyolitic domes or porphyries is also well established (Arribas et al., 1995; Sillitoe, 1999; Hedenquist et al., 1999; Sillitoe and Hedenquist, 2003; Einaudi et al., 2003; Simmons et al., 2005). However, a number of Mexican Ag/Au deposits are classified as of intermediate sulfidation. Their geological framework does not fit easily into the simple genetic/chronological model proposed so far, and some have been already revised and reclassified in Levresse et al. (2017) and Zamora-Vega et al. (2018), who showed that their magmatic and mineralization history is more complex, and that some Ag-Au- districts, such as Ag-Zacatecas and Au-Plomosas, might be the result of telescoping of various mineralization events.

The San Dimas district is a historical world class Ag/Au epithermal deposit located in the SMO, in the westernmost part of Durango State

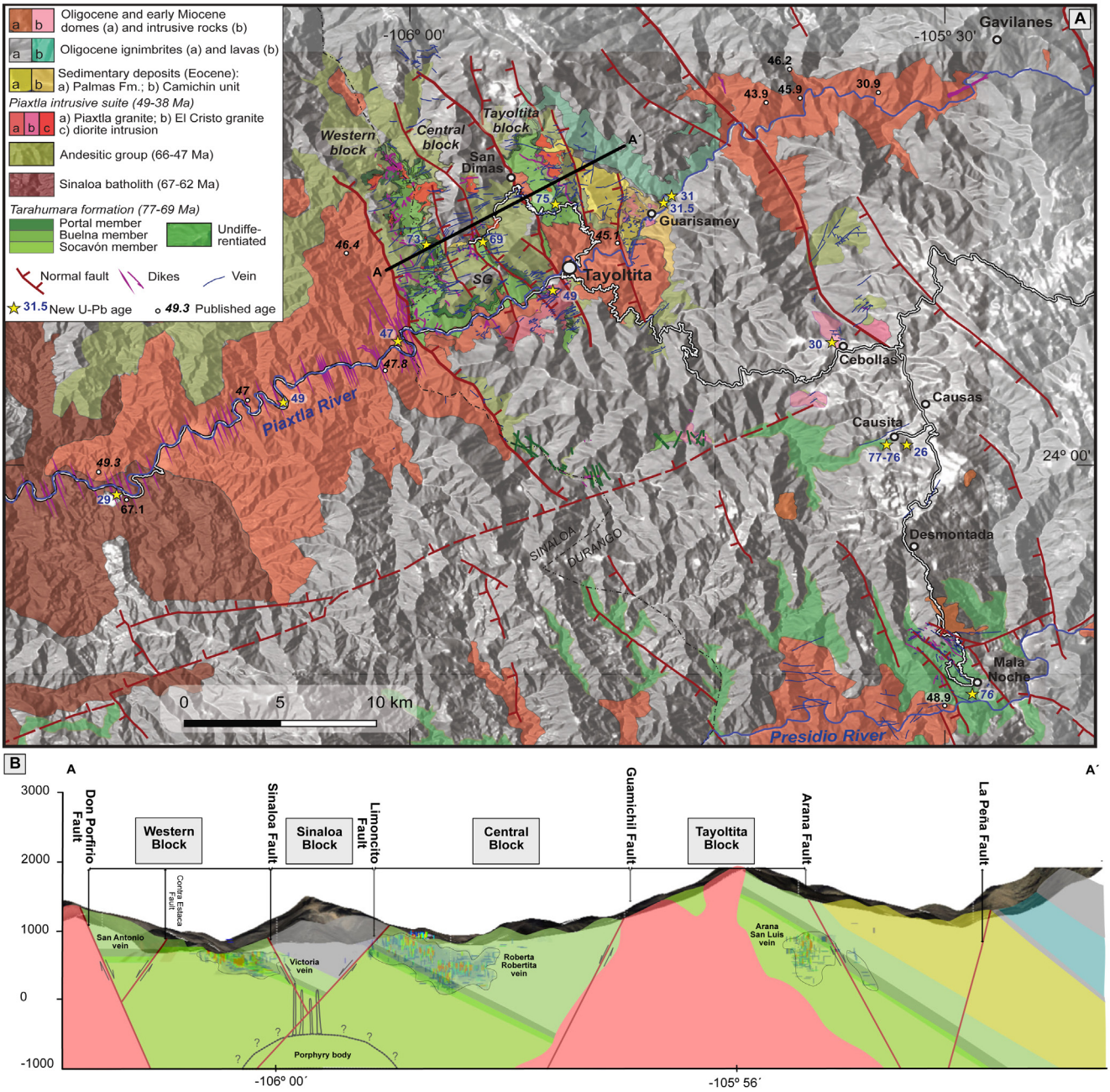

Fig. 2. (A) Geologic map of San Dimas mining district and Causita-Mala Noche areas, with location of published ages (from Montoya-Lopera et al., 2019). (B) Simplified geological cross-section of the Ag/Au San Dimas district.

near the boundary with Sinaloa State (Fig. 1). San Dimas is a good example for the geological complexity of the Mexican Ag/Au epithermal deposits. Currently, this deposit has been considered to represent a long-lived intermediate to low sulfidation epithermal deposit (Enríquez et al., 2018). The metallogenic model is based on underground observations of a limited portion of the district (Tayoltita Block mainly; Fig. 2) and presents unresolved problems that need attention, such as unreliable K-Ar and ^{40}Ar-^{39}Ar cooling ages in an area affected by pervasive and widespread potassic alteration and, more importantly, differences in gangue minerals between individual veins (Henshaw, 1953), which were emplaced in two different structural systems (Horner and Enriquez, 1999), during an unusually long single epithermal event (~41 to 31 Ma, Enríquez et al., 2018) that does not match with the local and regional magmatic pulses (Ferrari et al., 2018a; Montoya-Lopera et al., 2019).

In this paper we present the results of a new detailed study of the Ag/Au mineralization of the San Dimas district. New petrographic and geochronological data (zircon U-Pb, adularia ^{40}Ar/^{39}Ar and titanite fission track ages), zircon trace-element composition, gold and silver geochemistry led to an improved model of the world-class San Dimas epithermal systems in relation to the geodynamic evolution of the SMO.

2. Regional geological setting

The San Dimas mining district is located in the central part of the Sierra Madre Occidental (SMO), near the Sinaloa-Durango state border (Fig. 1). As a physiographic province, the SMO comprises a high plateau with an average elevation exceeding 2000 m above sea level, extending from the Mexico-US border to the Trans-Mexican Volcanic Belt (Fig. 1). As an igneous province, the SMO includes Late Cretaceous to early

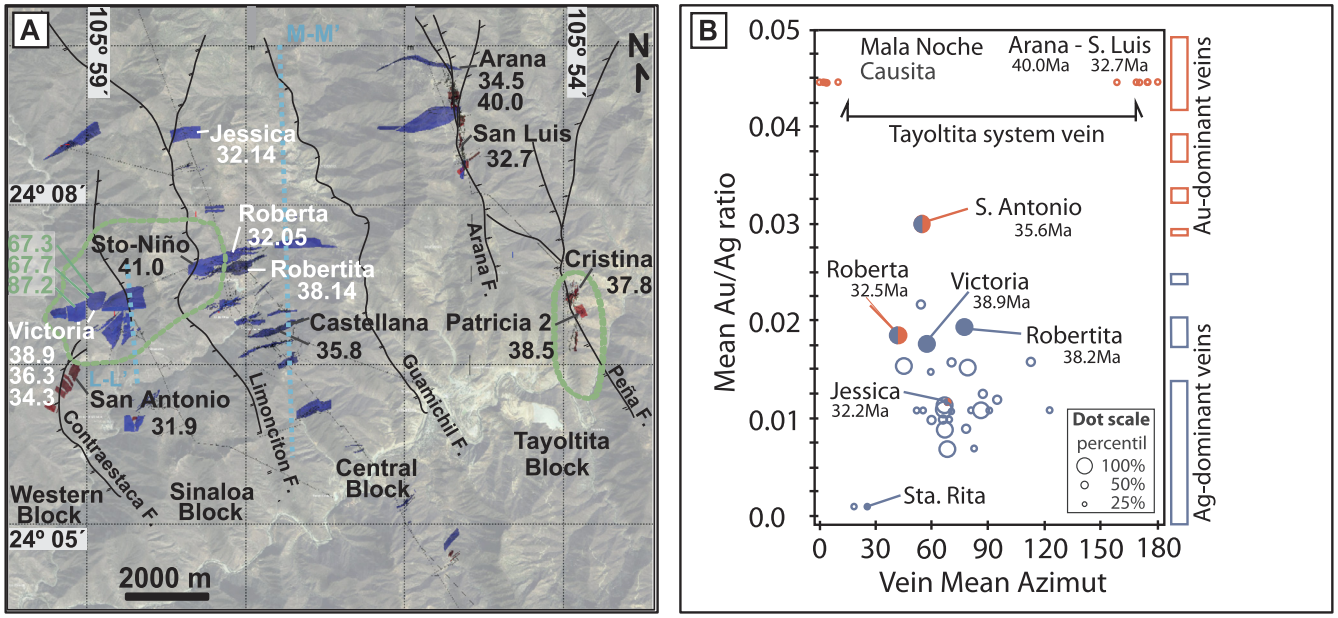

Fig. 3. (A) Au/Ag veins distribution and ages in the San Dimas mining district. Ages in black: K-Ar and $^{40}Ar/^{39}Ar$ in adularia and sericite from Enríquez et al., 2018; Ages in white: $^{40}Ar/^{39}Ar$ in adularia this study; Ages in green: U/Pb on zircon crystal LAICPMS, this study; (B) Discrimination diagram of Au/Ag in whole ore samples versus vein azimuth. Red: Au-dominant veins. Blue: Ag-dominant veins. (For interpretation of the references to color in this figure legend, the reader is referred to the web version of this article.)

Miocene rocks formed during two main periods of continental magmatic activity (Ferrari et al., 2018a). The first period produced a dominantly intermediate intrusive suite and its volcanic counterpart, the so-called Laramide magmatic arc, which developed during east-verging subduction of the Farallon plate beneath the North America continent between ~100 and 50 Ma (Gastil, 1975; Henry et al., 2003; McDowell et al., 2001; Ortega-Gutiérrez et al., 2014; Valencia-Moreno et al., 2017). These rocks are traditionally grouped within the Lower Volcanic Complex (LVC; McDowell and Keitzer, 1977). After a transitional period that lasted until the late Eocene (Ferrari et al., 2018a), volcanism became markedly silicic and then bimodal, making the so-called Upper Volcanic Supergroup (UVS; McDowell and Keitzer, 1977). Silicic ignimbrites represent the overwhelming component of this volcanism, which makes the SMO one of the largest silicic volcanic provinces on Earth (Bryan and Ferrari, 2013). Most of these rocks were emplaced in two ignimbrite flare up episodes at ~35–29 Ma along the entire province and at ~24–20 Ma in the southern SMO (Ferrari et al., 2002, 2007; McDowell and McIntosh, 2012). Mafic lavas, often with an intraplate affinity, are found intercalated within the ignimbrite successions since 33 Ma (Ferrari et al., 2018a; 2018b).

3. Local geological setting

Since the eighteen century, the San Dimas district has been managed by different mining companies. The last one is First Majestic Silver Corp., which acquired the operation and exploration in 2017. Historical production of San Dimas has been estimated in 11 million ounces of gold and 745 million ounces of silver.

The San Dimas stratigraphic column can be divided into two major igneous successions that correspond to the LVC and UVS, separated by erosional and depositional unconformities. A detailed description of the lithology, petrography and geochronology of the stratigraphic column is given in Montoya-Lopera et al. (2019) and is briefly summarized here. The Late Cretaceous to Eocene LVC, is composed of four members locally named "Socavón *rhyolite*", "Buelna *andesite*", and "Portal *rhyolite*" (Henshaw, 1953) and by the Andesitic Group as defined in Montoya-Lopera et al. (2019) (Fig. 2). The Socavón member consists of an alternating suite of rhyolitic and andesite lava flows dated at ~ 77–75 Ma locally intruded by mineralized felsic porphyritic bodies (~75–73 Ma) (Montoya-Lopera et al., 2019). The Buelna member is a sequence of andesitic lava flows and the Portal member is a sequence of rhyolite lava flows and tuffs, both dated at ~69 Ma (Montoya-Lopera et al., 2019). Based on lithology and age, Montoya-Lopera et al. (2019) correlated these three members with the Tarahumara formation defined by Wilson and Rocha (1949) and McDowell et al. (2001), which is widely exposed in Sonora state and represent the volcanic counterpart of the Laramide arc. The Andesite Group has a thickness of over 800 m and is formed by intermediate lava flows, tuffs, dikes and hypabyssal intrusions of Paleocene and early Eocene ages (Montoya-Lopera et al., 2019). The entire LVC volcanic column is crosscut and locally assimilated by the late Eocene Piaxtla batholith. The oldest intrusive bodies of the Piaxtla batholith (locally named El Cristo at Tayoltita) are fine-grained granites rich in K-feldspar that yielded ages of 49.1 and 49.0 Ma (Henry et al., 2003; Montoya-Lopera et al., 2019). The main body consists of a coarse- to medium-grained granodiorite with U-Pb ages of 49.1 to 47.0 Ma and a medium- to fine-grained granite dated at 45.2 Ma (Henry et al., 2003; Montoya-Lopera et al., 2019). The transition between the LVC and the UVS is marked by the Las Palmas and Camichin continental conglomerates, sandstones, red beds and mudstones, with a maximum age of deposition of ~ 52 and ~ 43 Ma, respectively (Montoya-Lopera et al., 2019). The UVC unconformably covers the La Palmas and Camichin continental sedimentary formations, the Piaxtla batholith or/and the Andesite Group. It is composed by two successions of silicic ignimbrites with ages of ~31.5 to 29 Ma and ~ 24 Ma respectively, with intercalations of minor amount of mafic lavas and continental conglomerate (Montoya-Lopera et al., 2019; Fig. 2). The lower ignimbrite succession is intruded by rhyolitic domes dated at ~29 Ma (Ferrari et al., 2013) and crosscut by dykes of bimodal composition (Montoya-Lopera et al., 2019).

4. Previous model of the mineralization of San Dimas Ag-Au district

The Ag/Au epithermal veins can be grouped into two sets striking E-W to WSW-ENE and NW-SE (Horner and Enriquez, 1999; Montoya-Lopera et al., 2019; Fig. 2). Both sets of veins pinch out, swell, bifurcate

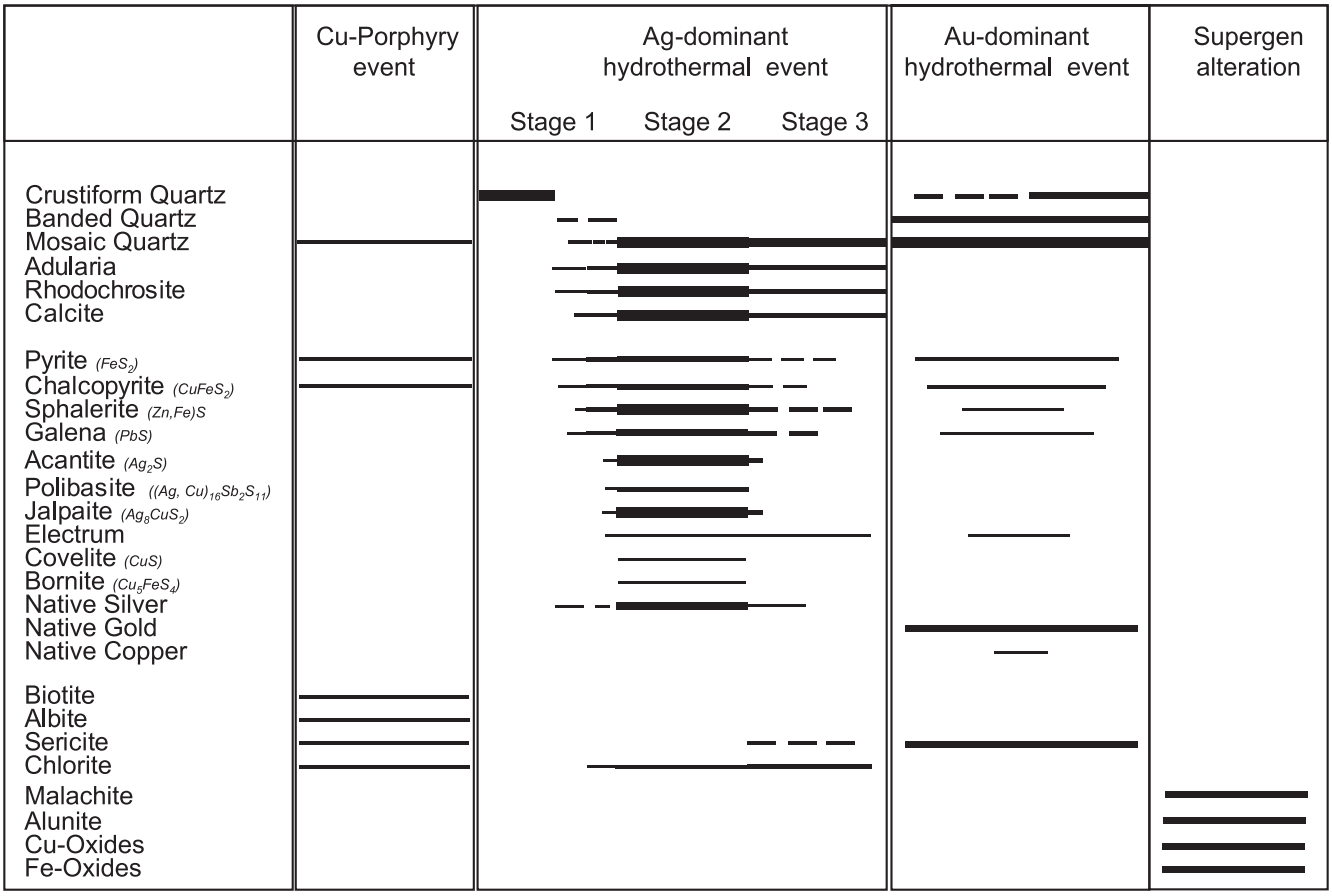

Fig. 4. Paragenetic sequence of the San Dimas mineralization events (see text for details).

and exhibit horse-tailing and sigmoid structures (Figs. 2 and 3; Horner and Enriquez, 1999). They are emplaced within the Paleocene to Eocene LVC volcanic and plutonic units, with the UVC considered barren and postdating the mineralization (Henshaw, 1953). Veins vary from less than a centimeter to fifteen meters in width, with an average of 1.5 m. Ore shoots are 150 m along the strike and 200 m down-dip on average (Henshaw, 1953; Enriquez and Rivera, 2001a). Mean Au/Ag ratios vary from vein to vein (from 0.0002 to 0.5812) and the vertical Au/Ag ratio variation within the structure can be normal or inverse (Smith et al., 1982). Vein texture and paragenesis are comparable within the district (Fig. 2; Davidson, 1932; Henshaw, 1953; Smith and Hall, 1974; Keller, 1974; Smith et al., 1982; Clarke, 1986; Clarke and Titley, 1988; Enriquez and Rivera, 2001a and 2001b; note that until 2000, production was limited to the Tayoltita and Guarisamey blocks).

Previous authors (Davidson, 1932; Henshaw, 1953; Smith et al., 1982; Clarke, 1986; Enriquez and Rivera, 2001a,b) divided the paragenetic sequence in three major mineralization stages: (1) early stage, (2) ore stage, and (3) late quartz stage. The early stage is characterized by light to dark crystalline and microcrystalline quartz with or without coarsely crystalline sphalerite, fine-grained galena and chalcopyrite with or without minor Ag-Au values (Enriquez and Rivera, 2001a,b). The ore stage is divided into three distinct sub-stages (a) quartz-chlorite-adularia, (b) quartz-rhodonite, and (c) quartz-calcite (Henshaw, 1953, Enriquez and Rivera, 2001a,b; Enríquez et al., 2018) with base metal sulphides (Cu-Fe-PbS) limited to the quartz-rhodonite stage. Finally, the late quartz stage is identified by milky and amethystine quartz, with small amounts of pearceite, native silver, chalcopyrite, calcite, and zeolites (Henshaw, 1953, Smith et al., 1982). Alteration aureoles are represented by albite-adularia-sericite, overprinted by a pervasive propylitic alteration (chlorite + epidote + pyrite + calcite). Fluid inclusion studies from stage 2 and 3 indicate that Ag-Au ore were deposited at a minimum temperature ranging from 250 to 320 °C, with petrographic evidence of boiling, and apparent NaCl salinities ranging from 3.3 to 9.7 NaCl equivalent. Mineralization precipitation depths were estimated at approximately 500 m below the paleo-phreatic level (Albinson, 1978; Smith et al., 1982; Clarke and Titley, 1988; Conrad et al., 1992). Composition of gas in fluid inclusions indicates that water constituted over 99.5 mol percent of the liquid and gas phases, with CO_2 accounting for most of the remainder (Smith et al., 1982). Finally, quartz $\delta^{18}O$ values for stage 2 and 3 in the range from +3.9 to +4.8‰ indicate that meteoric water dominated the hydrothermal system (Smith et al., 1982).

Dating the mineralization has been attempted in different veins (n = 7; Fig. 2) using both K-Ar and ^{40}Ar-^{39}Ar step heating techniques on adularia or sericite. The cooling ages obtained are distributed more or less continuously from 41.01 ± 0.23 Ma to 31.9 ± 0.8 Ma (Henry, 1975; Enriquez and Rivera, 2001a; Enríquez et al., 2018). Taking this age range as reliable, Enriquez et al. (2018) suggested that epithermal mineralization occurred during a ~10 Ma-long time span, which would represent the longest epithermal mineralization episode in a Mexican deposit. Since the ~41 to ~31 Ma ages overlap with the K-Ar ages of subvolcanic andesitic intrusions (38.1 and 36.6 Ma) a potential genetic relationship was suggested (Enriquez and Rivera, 2001b; Enríquez et al., 2018). This genetic interpretation is now challenged by the more reliable U-Pb ages for the subvolcanic andesitic intrusions and the whole Andesitic Group (~63 to ~48 Ma) recently published by Montoya-Lopera et al. (2019). Dating of the complete San Dimas stratigraphic column by these authors revealed that the previously reported mineralization ages correspond to a magmatic lull in the region, casting doubt on their geologic meaning.

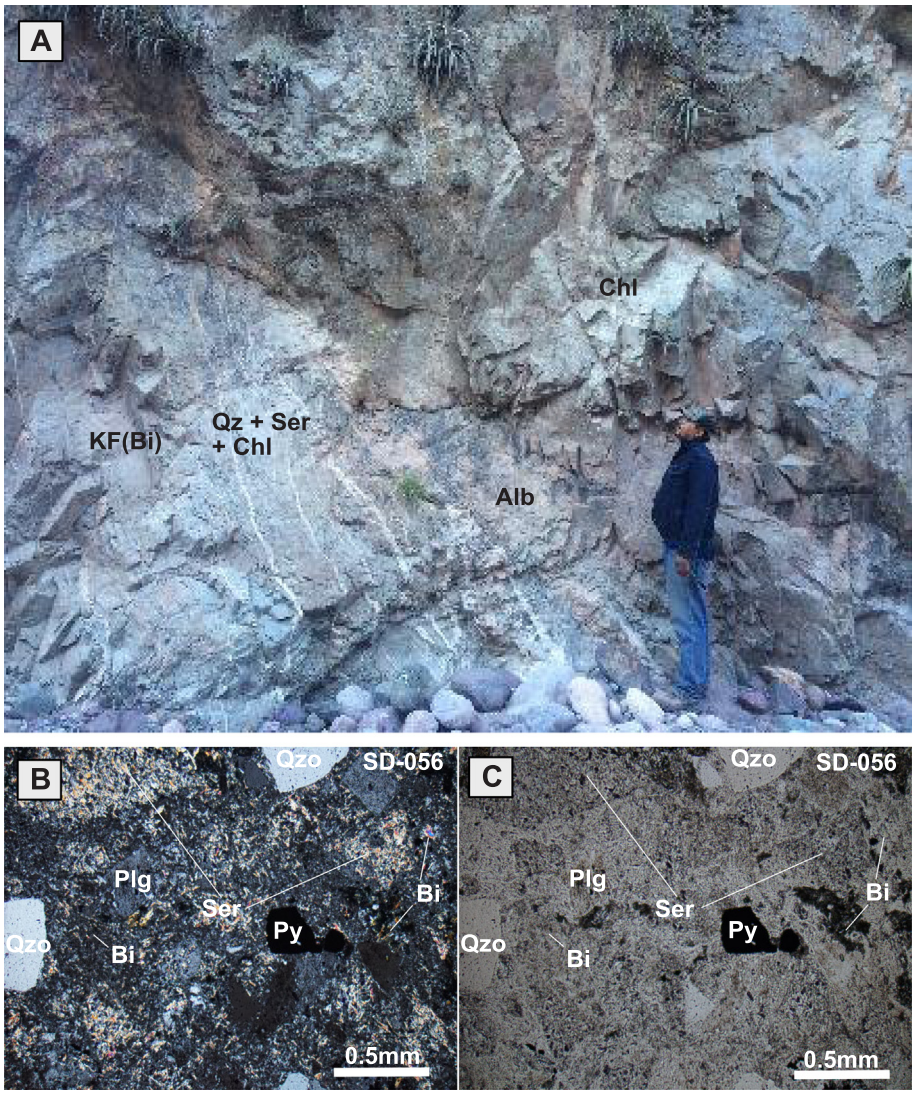

Fig. 5. Mineral associations of the Cu-porphyry mineralization event. (A) Porphyry subvolcanic Cu-Au mineralized intrusion outcropping in the Contraestaca area (Western Block); (B) and (C) petrographic thin sections of andesite porphyry mineralized intrusion (phenocrystals ≪ matrix) with dominant strong biotite (Bi) potassic alteration overprinted by subordinate patches of albite (Alb) + sericite (Ser) and traces of epidote (Ep) + chlorite (Chl) veinlets. (H) Andesite porphyry intrusion (matrix > phenocrystals) with dominant subordinate biotite potassic alteration overprinted by strong pervasive albite alteration and trace of chlorites and thin quartz veinlets.

5. Results

A complete description of methods and techniques used to obtain the data reported in this paper can be found in the electronic supplementary material. Fieldwork, vein chemistry and petrographical descriptions allowed to clearly differentiate three mineralization types within the San Dimas district: (1) Cu-Au porphyry type; (2) Ag-dominant hydrothermal type with quartz-adularia-rhodochrosite associated to the E-W trending vein system, and (3) Au-dominant hydrothermal type with quartz-sericite associated to the N-S trending vein system (Figs. 3 to 7). In the following section we describe in detail the main characteristics of mineralization textures and paragenesis of each event.

5.1. Mineralization structures and their distribution

Here we focus on the mineralized structures of the modern district, whose size has increased significantly in the past two decades. Within the district, 61 mapped structures have been recognized so far. They crosscut the whole LVC, the Piaxtla batholith and the upper unit of the Las Palmas continental sedimentary formation (maximum age of deposition ~43 Ma; Montoya-Lopera et al., 2019). To analyze the chemical variations within the mineralized structures, we compiled a database of over 43,000 chemical assays from drill holes and vein channel samples from the whole the San Dimas district (First Majestic mining company, exploration and production database). The statistical distribution of the Au/Ag ratios in veins at the district scale point to two different families: 1) Ag-dominant veins (Au/Ag < 1/25), mainly associated to E-W structures with larger volume size (Fig. 3B); and 2) Au-dominant veins (Au/Ag > 1/25) associated to the N-S structures at the eastern and western sides of the district, with lower volume size (Fig. 3A and B). A few E-W striking large volume Ag-dominant structures show significant Au enrichment toward deeper levels (Victoria, San Antonio, Roberta-Robertita veins; Fig. 3A and B) suggesting potential telescoping mineralization. In both sets, the Au/Ag ratios increase with depth. Finally, in the Sinaloa and Western blocks the Ag-dominant veins are characterized by higher Cu concentrations. Throughout the district a single economic horizon has been long recognized between ~950 and ~258 m asl, roughly sub-parallel to the LVC stratigraphic upper contact and presenting the same general dip of ~35° to the east (Fig. 2).

5.2. Geological and petrographic characteristics of mineralization types

5.2.1. Cu-Au porphyry mineralization type

In the Contraestaca area (Western Block; Figs. 2, 4 and 5A) we recognized for the first time subvolcanic porphyry Cu-Au mineralized bodies intruding the LVC Socavón member (Figs. 2, 3 and 5). Such porphyry mineralization is also observed as clasts in hydrothermal breccias of the Victoria vein roots, within the Andesite Group (Sinaloa Block). Samples of these hypabyssal intrusions are characterized by a

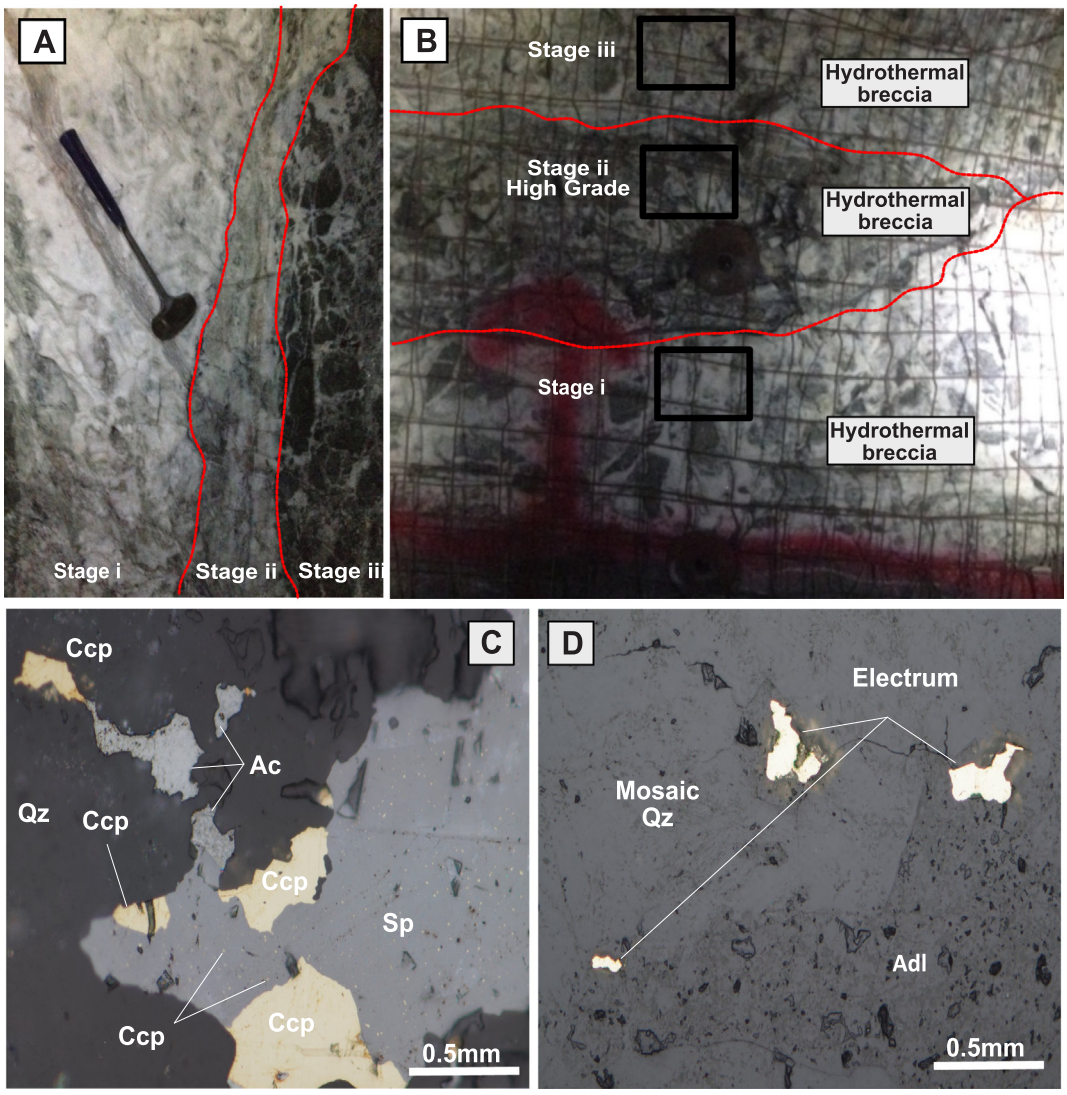

Fig. 6. Mineral associations of the Ag-dominant mineralization event. (A) and (B) Outcrops of vein textures of different stages at Victoria vein, Sinaloa Block. (A) Succession of crustiform and massive crowded quartz (stage i) in a crosscutting relationship with banded base metals (stage ii) and hydrothermal breccia (stage iii). (B) Three different hydrothermal breccias in a crosscutting relationship. (C) reflected light photomicrographs of replacement texture of sphalerite (Shp) in chalcopyrite (Ccp) and filling open space of acanthite (Ac) at stage i (Victoria vein, Sinaloa Block). (D) reflected light photomicrographs of anhedral electrum crystals filling open space fractures in mosaic quartz and coarse adularia at stage i (Victoria vein, Sinaloa Block).

porphyritic texture with discrete refractory quartz. They are dacite to andesite in composition and reddish to gray in color. Mineral paragenesis consists of quartz > orthoclase > plagioclase > pyroxene > biotite and hornblende phenocrysts in a groundmass of fine plagioclase and glass (Fig. 5 B and C). Three alteration processes were identified (1) a pervasive potassic alteration, mainly represented by secondary biotite replacing ferromagnesian phenocrysts and matrix minerals; (2) a sodic-calcic alteration with albite + actinolite ± epidote nidus, patches or halos around pyrite, and chalcopyrite and thin veinlets stockwork (Fig. 5 B and C); and (3) a late propylitic alteration with chlorite + epidote + calcite + pyrite overprinting the previous events. Mineralization is dominated by pyrite and chalcopyrite in thin veinlets disseminated into the groundmass and magnetite veinlets from < 1 mm to 10 cm in width.

5.2.2. Ag dominant hydrothermal mineralization type

The most significant mineralization event in San Dimas district is the Ag-dominant hydrothermal vein mineralization (Fig. 3). These veins are developed in three different stages, called opening, filling and closing. The filling stage is the main mineralization event with the highest Ag values (Fig. 6A). Main hydrothermal textures observed, in all stages, are hydrothermal breccias and banding with gangue composed by mosaic quartz with undulatory extinction with less adularia-rhodochrosite carbonate. The alteration intensity varies from weak and pervasive. Alteration mineral assemblage is represented by coarse grains of chlorite and less sericite. Base metal sulphides are the earliest phases; they can be found disseminated in the breccia fragments and rimming and overgrown on fragments, in bands alternating with quartz and carbonate or in pots into the quartz matrix. Monosulphides are rare and they occur mostly as aggregates or as xenomorphic areas (Fig. 6B); they are, in decreasing abundance, pyrite–arsenopyrite, sphalerite, galena and chalcopyrite. They are corroded by native silver, sulphides and sulphosalts. Silver sulphides (acantite, jalpeite and less polibasite) and electrum grains are also found free, filling fractures in quartz, adularia, and chlorite (Fig. 6C). Oxidation is scarce and locally limited to the very upper levels of the deposit. Locally in the Western and Sinaloa blocks, when the veins crosscut the Late Cretaceous porphyry intrusions, the mineralization is enriched in copper and bornite, with covelite and copper oxide completing the paragenesis.

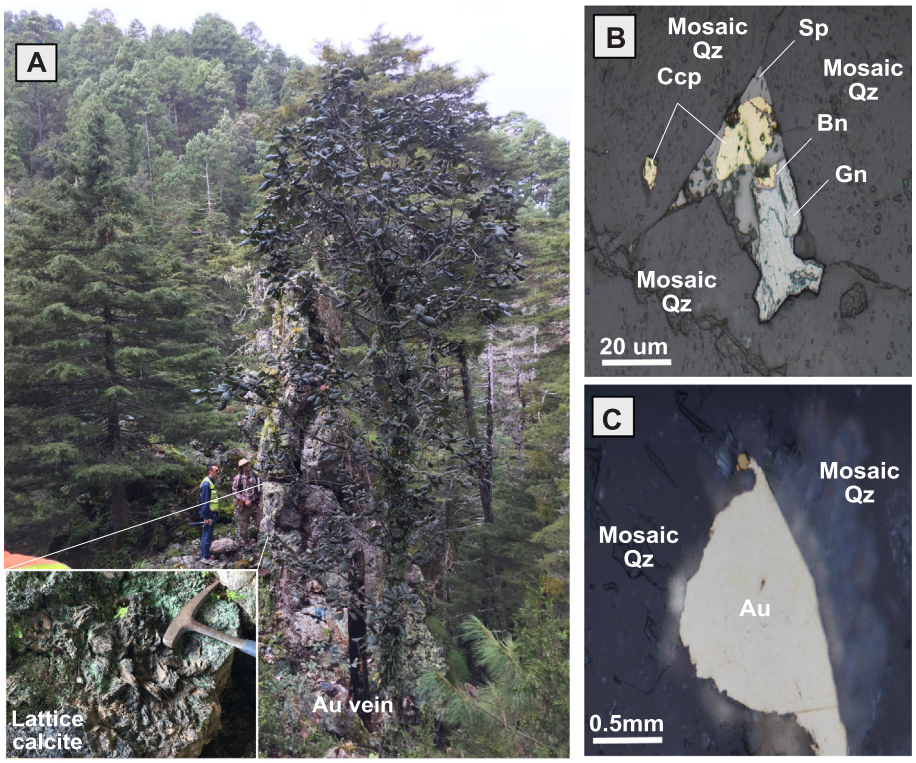

Fig. 7. Mineral associations of the Au-dominant mineralization event. (A) Field view of the Causitas Au vein, with zoom to lattice calcite texture developed at a late stage of mineralization. (B) Reflected light photomicrograph showing the paragenetic association of base metals, replacement textures of sphalerite in chalcopyrite and galena and reaction rims on chalcopyrites due to galena. These minerals fill open space fractures into mosaic quartz (San Luis Vein, Tayoltita Block). (C) Reflected light photomicrograph of a native gold crystal filling a fracture in mosaic quartz (San Luis vein, Tayoltita Block).

5.2.3. Au-dominant hydrothermal mineralization type

Six of the most representative Au-dominant vein structures were mapped in detail: San Luis and Arana veins in the Tayoltita Block, San Antonio and Guadalupe veins in the Western Block, and Mala Noche and Causitas veins in the prospecting area south of the district (Figs. 2 and 7A). These veins are typically symmetrically banded. Lattice texture comprises platy calcite and barite and its quartz pseudomorphs filling fractures (Fig. 7A). These veins show typical interbanded and discontinuous layers of base metal mineralization ± native Cu, the latter increasing toward the Western Block (Fig. 7B). A weak to pervasive sericite alteration is present throughout the veins. Gangue is represented by crustiform and mosaic euhedral quartz texture with undulatory extinction. The mineral abundance is pyrite > sphalerite > galena > chalcopyrite ± bornite ± native Cu in euhedral to anhedral coarse grains. Fig. 7B illustrate the copper reaction rims between chalcopyrite and galena. Overgrowths of pyrite on sphalerites represent the late mineral within the base metals sequence. Free electrum grains are found filling fractures as anhedral coarse crystals that show medium to fine grain sizes (Fig. 7C).

5.3. Trace element abundances and correlations in electrum, native silver, and silver sulphides from Au- and Ag-dominant veins

Electron microprobe analyses (n = 98) of electrum, native silver and silver sulphide minerals from mineralized veins were conducted to detect potential chemical variations. Samples were collected from structures that record Ag- and Au-mineralization events of different intensity: Victoria Ag-dominant vein, and San Luis, San Antonio and Mala Noche Au-dominant veins. Results for 12 major elements of the ore suite (Supplementary Table S2) are presented as Principal Component Analysis (PCA) in Fig. 8.

Mineralogy and elemental relationships in the Ag- and Au-dominant mineralization events in all structures are broadly comparable. Silver is related to arsenic and base metals (Cu, Zn, Fe), and gold is preferentially associated with bismuth and mercury (Fig. 8). However some chemical differences are noted. In Ag-dominant structures, silver mineralization is associated to tellurium, and gold mineralization positively correlates with antimony. In Au-dominant structures, silver mineralization is relatively depleted in tellurium and enriched in antimony (Supplementary Table S2), and silver positively correlates with both antimony and tellurium (Fig. 8). Besides, the Au/Ag ratio in electrum significantly increases in the Au-dominant structures (Supplementary Table S2).

5.4. Geochronology of the porphyry and epithermal mineralization events

5.4.1. Cu-Au porphyry event

In an attempt to date the Cu porphyry mineralization found in the LVC, suitable exploration drill hole core samples were collected from the Victoria vein roots (VIC16-PC-1 and VIC13-PC-2; Figs. 2 and 3) in the Sinaloa block, and from two mineralized clasts (PM-1 and PM-2) from the first stage hydrothermal breccia of the Victoria vein (Fig. 6 A).

Thirty-nine analyses performed on zircon crystals from VIC16-PC-1 mineralized porphyry sample yielded $^{206}Pb/^{207}Pb$ ages ranging from 64.1 ± 2.5 Ma to 893.0 ± 17.0 Ma. Five analyses were discarded due to their high sigma errors. Within the remaining thirty-four concordant ages, twenty-two analyses form a tight cluster with a distribution tail towards the younger ages, and a weighted mean crystallization age (Ludwig, 2008) of 67.4 ± 1.1 Ma. (n = 22; MSWD = 1.16; Fig. 9, Supplementary Table S3). Thirty-four analyses performed on zircon crystals from VIC13-PC-2 mineralized porphyry sample yielded $^{206}Pb/^{207}Pb$ ages ranging from 63.0 ± 1.9 Ma to 456.0 ± 10.0 Ma. Five analyses were discarded due to their high sigma errors. Within the remaining twenty-nine concordant ages, twenty-one analyses form a tight cluster with a weighted mean crystallization age (Ludwig, 2008) of 67.6 ± 1.2 Ma. (n = 21; MSWD = 0.36; Fig. 9 Supplementary Table S3).

The two mineralized clasts (M−1 and PM-2) show a porphyry texture and are interpreted to correspond to the Andesite Group host rock. Eleven (PM-1) and five (PM-2) zircon crystals were analyzed in these barren samples, respectively. Three analyses in both samples were discarded due to their high sigma errors. The remaining eight analyses in the PM-1 sample form a tight cluster and yield $^{206}Pb/^{207}Pb$ ages ranging from 64.0 ± 2.3 Ma to 68.5 ± 2.9 Ma with a weighted mean

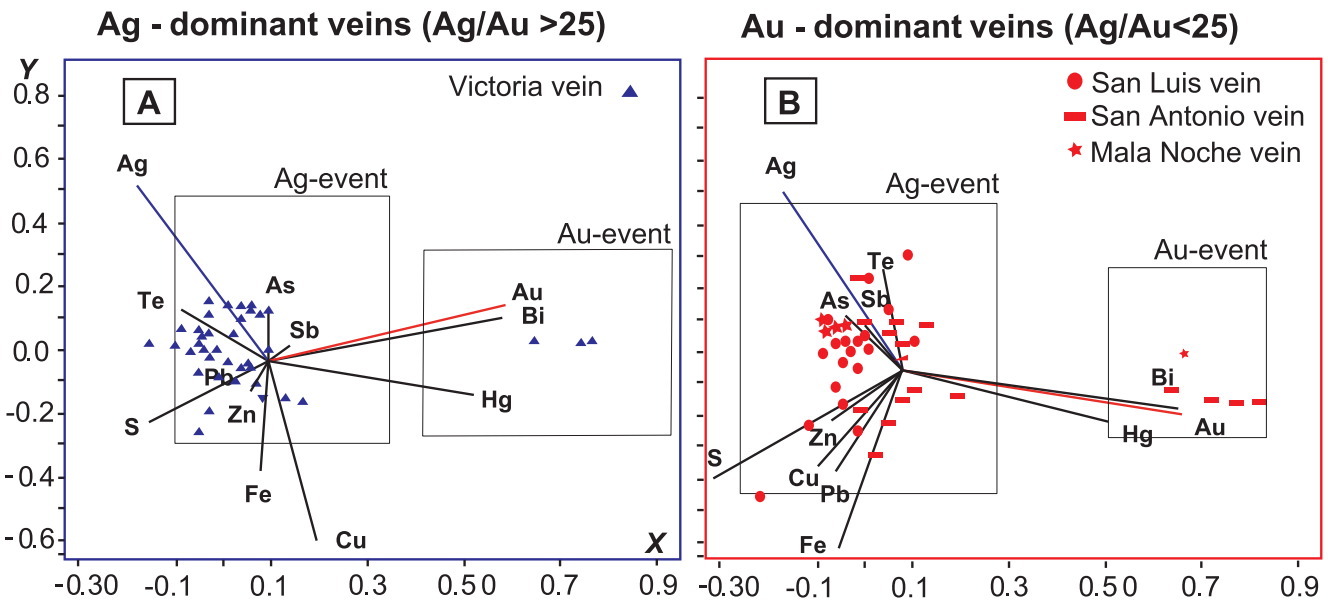

Fig. 8. Principal component analysis for 12 major elements determined in electrum, silver and silver sulphide grains from the (A) Ag-dominant mineralization event, and (B) Au-dominant mineralization event.

crystallization age of 66.1 ± 1.8 Ma (n = 8; MSWD = 1.15; Fig. 9, Supplementary Table S3). The remaining two analyses of sample PM-2 yield $^{206}Pb/^{207}Pb$ ages of 65.7 ± 2.7 Ma and 70.0 ± 4.0 Ma (Fig. 9, Supplementary Table S3).

As a whole, U-Pb dating of Cu-porphyry and related clasts in veins indicate a coherent period of magmatic intrusion ranging from 67 to 63 Ma. The presence of porphyry clasts in Ag-dominant veins suggest a spatial overlap of the two mineralizing events and explains the increased Cu content in the silver mineralization in these specific areas of the district.

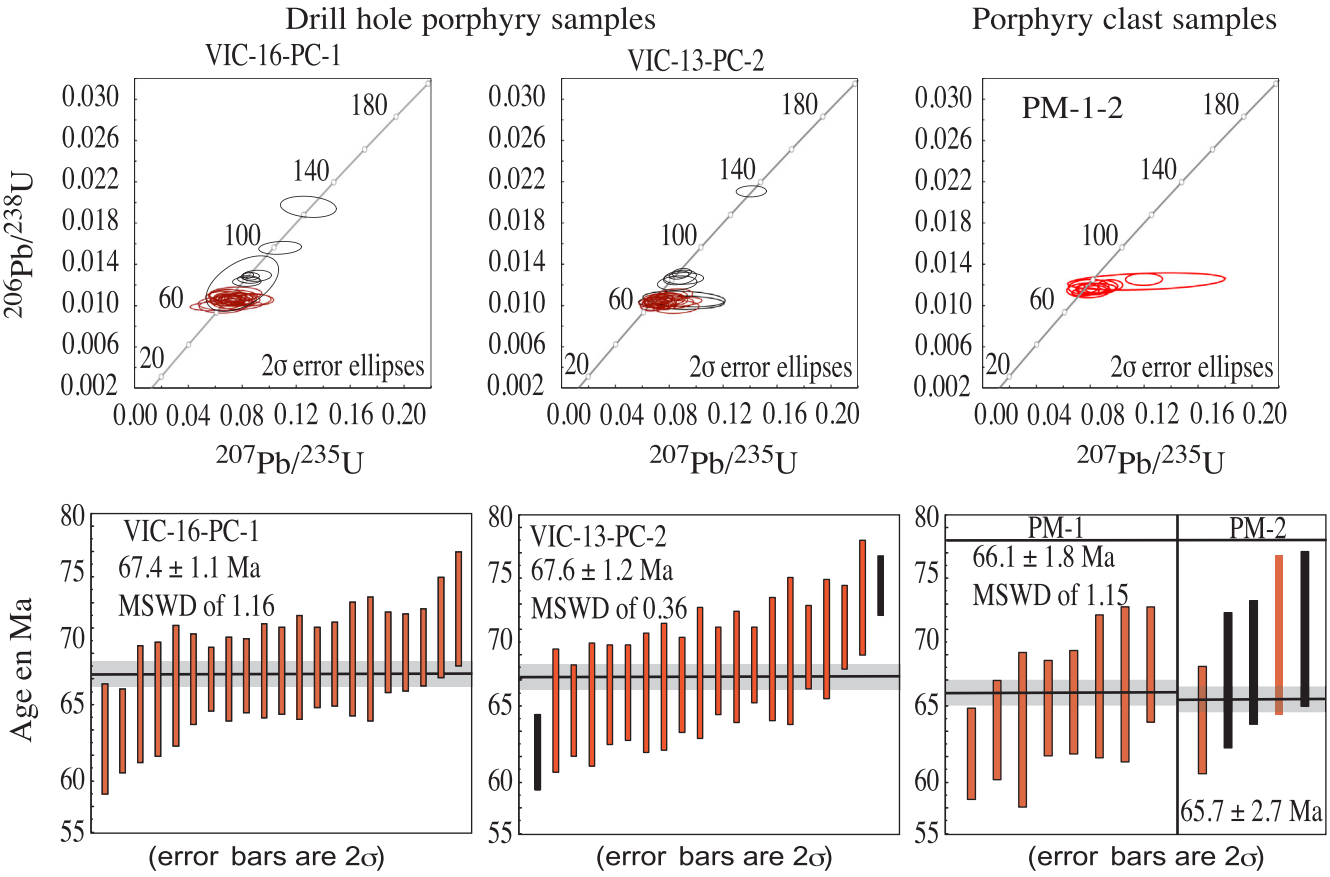

Fig. 9. U-Pb concordia diagrams and weighted mean U-Pb ages for zircons from two drill hole porphyries and two mineralized porphyry clasts (PM-1 and PM-2) from the Victoria vein. Errors in calculated ages are 2σ. Black ellipses and black bars are data not used in calculating the ages.

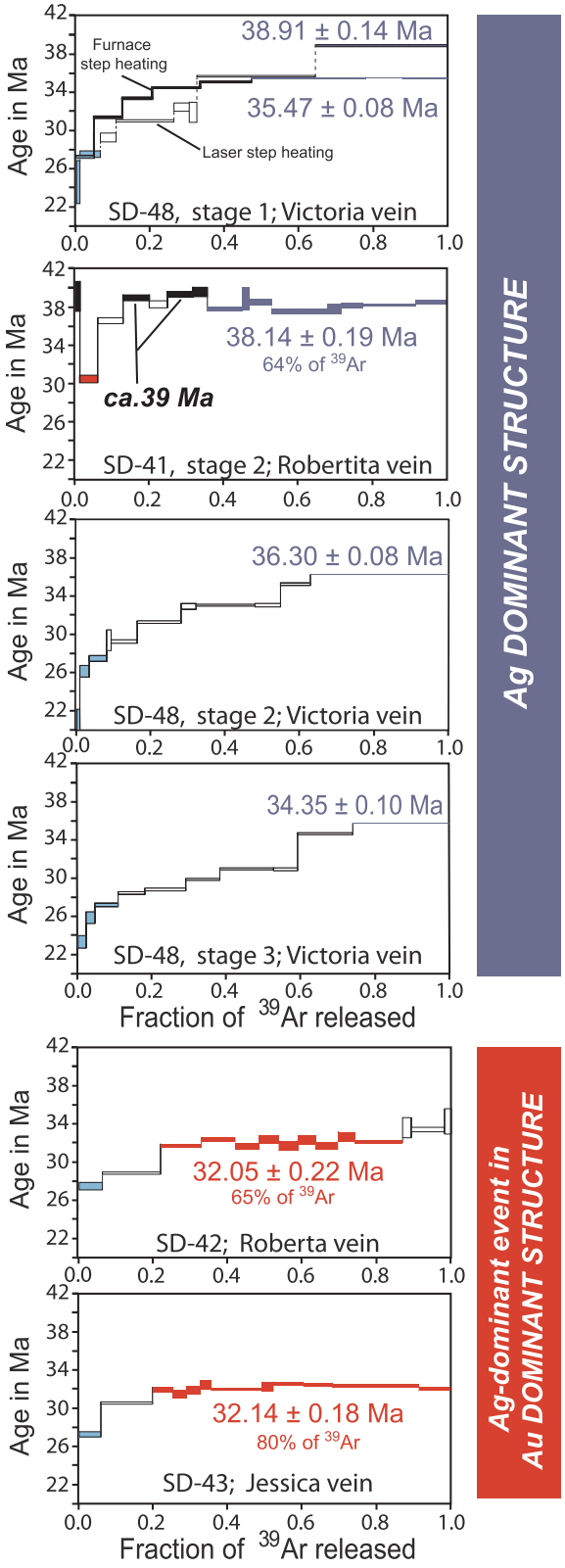

Fig. 10. Step heating $^{40}Ar/^{39}Ar$ spectra for adularia crystals separated from Victoria, Roberta, Robertita and Jessica veins. Spectra of all samples display variable degrees of perturbation with low temperature steps indicating argon loss. Plateau ages include the % of released ^{39}Ar, other ages correspond to single steps. Age errors are 95% confidence intervals. tp: plateau age; tc: inverse isochron age; Wm: weighted mean.

5.4.2. Ag- and Au-dominant mineralization events

Minerals suitable for dating of both the Ag- and Au-dominant mineralization events were identified in the petrographic study. Adularia is characteristic of the silver mineralization event, and sericite content increases in the gold-enriched veins structures. However, the separation and $^{40}Ar/^{39}Ar$ dating of pure hydrothermal sericite was technically too complicate because of the fine size and the alteration of the crystals. For adequate dating of both events, we sampled and dated the best-preserved adularia crystals most distant from the sericite aureole of the Ag-dominant structures, and the best-preserved adularia crystals in the more strongly altered sericite aureole in telescoped Ag-Au-mineralized structures.

Adularia separated from Victoria (n = 3), Robertita (n = 1), Roberta (n = 1), and Jessica (n = 1) veins was dated using the ^{40}Ar-^{39}Ar step-heating technique. The paragenetic position and the purity of all dated adularia were initially evaluated by cathodoluminescence and petrographic studies. The new ^{40}Ar-^{39}Ar ages are synthesized in Supplementary Table S4 and Fig. 10, and in Fig. 12 together with the available literature data.

All analyzed adularia samples display staircase-shaped age spectra from the lowest to the highest temperature step. In three experiments an apparent slight age decrease is observed at mid temperature steps (SD-41 stage 2, SD-42 and SD-43; Fig. 10 and Supplementary Table S4). Four experiments meet the criteria for a plateau crystallization age. In these cases, the inverse isochron ages are indistinguishable at the 95% confidence interval from the plateau ages (Fig. 10; Supplementary Table S4). Nevertheless, the steps in the inverse isochron diagrams concentrate at high $^{39}Ar/^{40}Ar$ values with little spread, which result in poorly defined $^{36}Ar/^{40}Ar$ intercepts and larger age errors. On these grounds, the plateau age is taken as the preferred age.

For adularia related to the Ag-dominant event (sample SD-41; Robertita vein) a plateau age of 38.14 ± 0.19 Ma (95% conf.) was obtained, whereas adularia from the Au-dominant event in the Roberta and Jessica veins, (samples SD42 and SD-43, respectively) yielded plateau ages of 32.05 ± 0.22 Ma (95% conf.) and 32.14 ± 0.18 Ma (95% conf.) (Fig. 10). In three experiments from Victoria vein (SD-48 stage 1–2-3), the staircase shape is too pronounced to determinate plateau ages. In these cases, isochron ages are not well defined neither and we interpret the higher temperature ages steps as minimum crystallization ages of 34.35 ± 0.10 to 38.91 ± 0.14 Ma (2σ). The oldest age from sample SD-48 stage 1 is comparable to the plateau age determined for adularia from Robertita vein and with the oldest $^{40}Ar/^{39}Ar$ ages reported in literature (ca. 40 Ma; Enríquez et al., 2018; Figs. 10 and 12). The younger plateau ages at ~ 32 Ma obtained for adularia from the Roberta and Jessica veins are also comparable to the K-Ar and $^{40}Ar/^{39}Ar$ ages reported in the literature (~32 Ma; Enríquez et al., 2018 and references therein; Figs. 10 and 12 and Supplementary Table S4). Finally, in all the seven experiments, the low temperature steps ages point to effects of argon loss at ages of 22 to 26 Ma. These ages coincide with a regional extensional event, contemporary with a major ignimbrite flare up, which might have led to a crustal thermal anomaly (Ferrari et al., 2013, 2018a; Montoya-Lopera et al., 2019).

5.5. Titanite fission-track thermochronology

To better constrain the Ag-dominant mineralization event, titanite fission-track dating was performed on a sample from the Eocene Piaxtla granite (SD-16), assuming that the hydrothermal event likely had an effect on the thermochronologic record of the batholith. Sample SD-040 was previously dated using U-Pb zircon geochronology revealing an age of ~ 49 Ma (Montoya-Lopera et al., 2019). The results show a very a high $P(\chi^2)$ value of 0.95, compatible with a single and short-lived thermal event. The model ages distribution ranges from ~45 to ~35 Ma, with a very well-defined Gaussian maximum at 40.3 ± 1.1 Ma (Fig. 11).

Fission track length modification occurs in titanite below ~310 °C

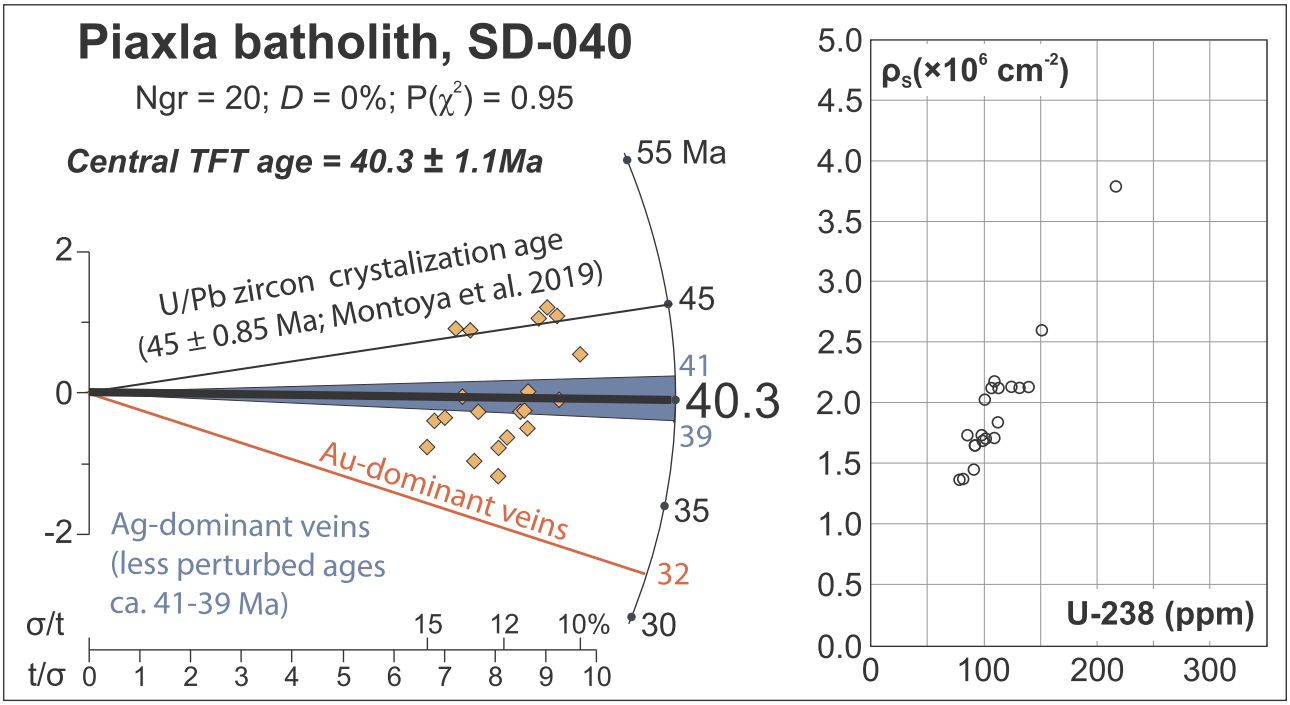

Fig. 11. Titanite fission track radial plot for sample SD-040 from the Piaxtla granite. The blue band represents the age of the Ag-dominant hydrothermal mineralizing event. The ρ_s versus ^{238}U graph indicates the confidence of the single event age determination. The U-Pb zircon crystallization age of the Piaxtla batholith and the age of Au-dominant veins are showed for comparison. (For interpretation of the references to color in this figure legend, the reader is referred to the web version of this article.)

(Coyle and Wagner, 1998). The hydrothermal FT reset age on titanite from the Piaxtla granite is in good agreement with the $^{40}Ar/^{39}Ar$ ages on adularia for the Ag-dominant event. By contrast, the Au-dominant hydrothermal event is not recorded in the FT age of titanite, suggesting lower hydrothermal temperatures for this event. In conclusion, the integration of our new $^{40}Ar/^{39}Ar$ ages on adularia and FT ages on titanite pin-point the occurrence of the Ag-mineralizing event at 40 ± 1.1 Ma (Fig. 11), well separated from the Au-dominant event that occurred in the early Oligocene.

5.6. Zircon geochemical signatures

In this section, the evolution through time of the chemistry of zircon crystals in the local stratigraphic column (Montoya-Lopera et al., 2019) is used to establish possible correlations between magma chemistry and the Eocene and Oligocene mineralizing events dated at ~40 Ma and ~32 Ma (this study), respectively. Within the local stratigraphy, the hydrothermal events occur at the beginning and at the end of a ca. 10 Ma magmatic lull. As proposed for other regions worldwide (Ballar et al., 2002; Dilles et al., 2015; Lu et al., 2016), the zircon trace element chemistry can be used to identify periods of fertile magmatism and to define potential time relationships between magmatic and hydrothermal/mineralization events through the use of Eu/Eu* and (Ce/Nd)/Y) versus U/Pb zircon ages plots (Ballar et al., 2002; Dilles et al., 2015; Lu et al., 2016). Zircon U/Pb ages (Montoya-Lopera et al., 2019) and trace element compositions (this study; Supplementary Table S5) from Late Cretaceous to late Oligocene volcanic and sedimentary units in the district are presented in Fig. 12.

The evolution of the zircon Eu/Eu* and (Ce/Nd)/Y) ratios through time strongly point to the occurrence of three fertile magmatic events: (1) a hydrated and oxidized event related to Late Cretaceous arc magmatism; (2) a hydrated and oxidized event associated to Eocene magmatism (from 50 to 43 Ma; Eu/Eu* > 0.3 and (Ce/Nd)/Y > 0.01), which is characterized by a gradual increase in the Eu/Eu* ratio with time and correspond to the construction of the Piaxla batholith; (3) a hydrated and reduced event (Eu/Eu* > 0.3 and (Ce/Nd)/Y < 0.01) corresponding to the emplacement of early Oligocene UVS rhyolitic ignimbrites and domes (Fig. 12).

Zircon chemistry clearly illustrates the most likely magmatic sources for the hydrothermal pulses and thus brackets the age of the mineralization events. It also allows identifying the chemical differences between the Eocene and Oligocene events that favored the Ag- or the Au-mineralization style. The Eocene fertile period with hydrated and oxidized magmatism favored the transport and concentration of silver metals. The continuous increase of Eu/Eu* and (Ce/Nd)/Y ratios during the formation of the Piaxla batholith suggests that the age of the silver mineralizing event may be bracketed between the last zircon age of ~43 Ma and the first hydrothermal mineral age (adularia) at ~41 Ma. On the other hand, the Oligocene chemical anomaly confirms the field relationship between rhyolitic domes and gold veins. The zircon chemistry of early Oligocene volcanics suggests a hydrated and reduced magma, favoring the transport and concentration of gold metals.

6. Discussion and conclusions

The first mineralization event recognized in San Dimas district is related to Cu-porphyries intrusions associated with the formation of the Laramide magmatic arc during Late Cretaceous to early Paleocene times. Two different pulses are recognized, the first at ~73–75 Ma (Montoya-Lopera et al., 2019) and the second, more intense, at ~67 to 63 Ma. These ages coincide with the ages of the Cu-porphyry deposits of northwest Mexico (Sonora state) and southwestern U.S.A (Arizona, New Mexico) (Valencia-Moreno et al., 2017 and references therein). The Cu-porphyry stocks are probably associated with subduction-related Laramide batholiths, well exposed to the west in Sinaloa. The porphyries recognized at San Dimas probably represent the southeastern most Cu-porphyries intrusions of the Cordilleran belt. In Sinaloa, Cu-porphyry intrusions are generally scarce, and geographically restricted to the coastal area (e.g. the Cosalá and La Azulita deposits Valencia-Moreno

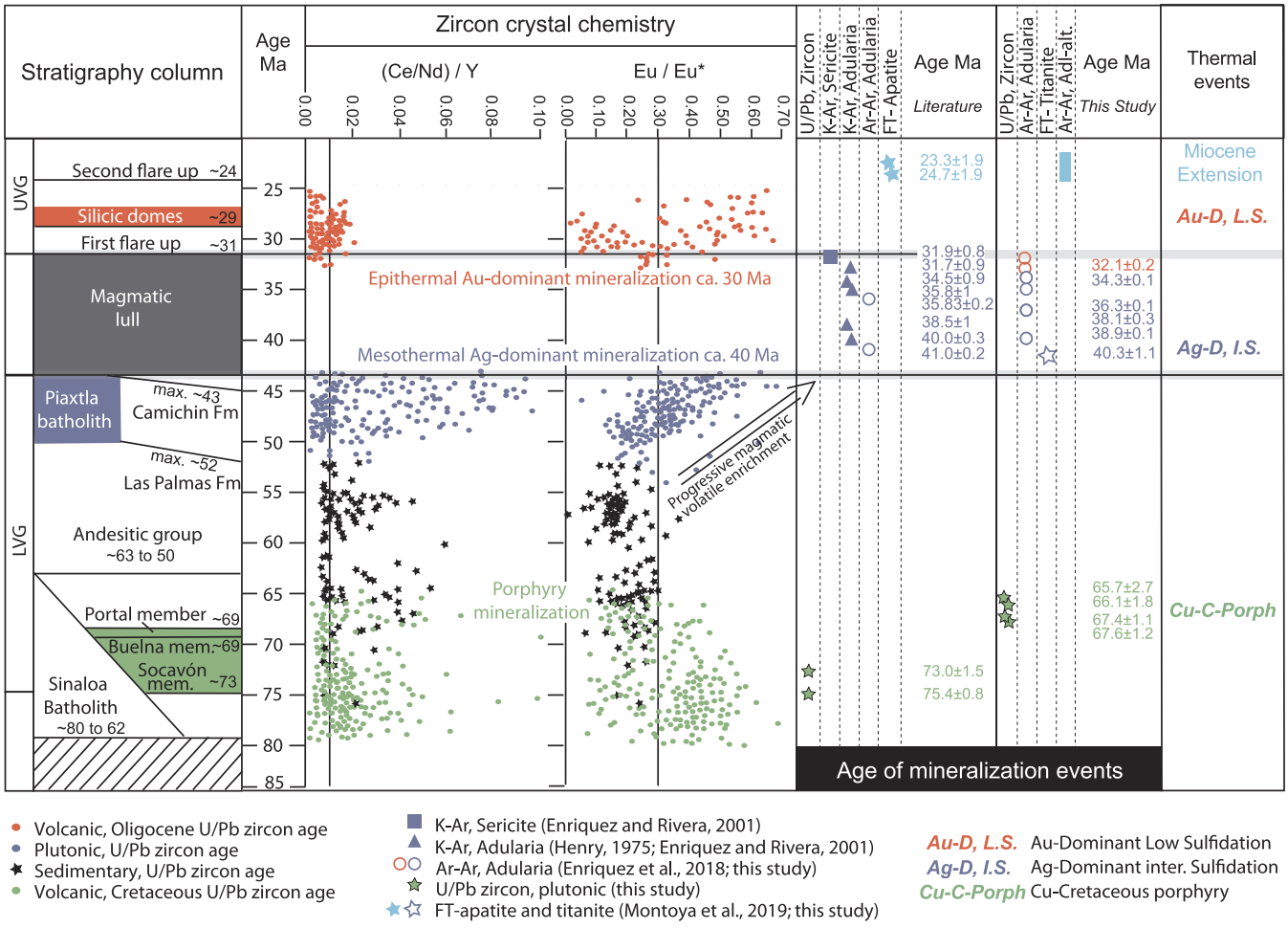

Fig. 12. Synthesis diagram of the trace elements variation in zircon crystals through time. ^{238}U-^{206}Pb ages of single zircon crystals from Montoya-Lopera et al. (2019); K-Ar and $^{40}Ar/^{39}Ar$ ages from Enríquez et al. (2018) and this study; apatite and titanite fission tracks data from Montoya-Lopera et al. (2019) and this study. Local stratigraphic column from Montoya-Lopera et al. (2019).

et al., 2017). The discovery of Cu-porphyry intrusions in San Dimas extends the exploration targets to the east, below the Oligocene volcanic cover.

The following mineralization events, the Ag and Au hydrothermal events, were distinguished and characterized on the basis of a detailed petrographic, geochemical and geochronologic study of the vein systems. Detailed geological field work indicates strong structural control on metal deposition, which exhibit a wide range of Au/Ag ratios, ranging from Ag-dominant to Au-dominant mineralized structures (Figs. 2, 3, 6 and 7). Ag- and Au-mineralization types were emplaced in two different structural systems (Horner and Enriquez, 1999). Ag-dominant mineralization structures are mainly hosted in E-W sigmoidal tension gashes and geographically distributed in proximity to the Eocene Piaxtla batholith. Au-dominant mineralization structures are mainly hosted in N-S faults systems that have undergone multiple reactivations and are geographically associated with Oligocene rhyolitic domes. The Ag- and Au-dominant events are characterized by different vein texture, mineralogy, and Au-Ag ratios. The Ag-dominant veins are composed by various quartz and breccia events and are characterized by adularia and rhodochrosite alteration. The Au-dominant veins are monogenetic and characterized by intense sericitization. In both Ag- and Au-dominant events, trace element chemistry show distinct metals affinities suggesting different metal sources and/or P-T-fO_2 mineralizing fluids conditions. Ag- and Au-dominant veins present comparable metal associations in two different patterns: a) silver sulphide minerals associated to base metals, and b) electrum gold grains with As, Sb, Hg signature. Strong negative correlations between silver and base metals illustrate the chemical evolution of fluids during the Ag hydrothermal event, which is in good agreement with the petrographic observations. The Au epithermal event is clearly disconnected from the Ag event regarding metal association. The presence of tellurium in the silver association points to a connection to subduction processes and mantle wedge enrichment (Sanders and Brueseke, 2012). The Au, Hg, Sb, and Bi association is commonly related to shallow epithermal systems (Gray et al., 1991; Bornhorst et al., 1995). The increase of Sb in the Ag-dominant veins suggests a more distal position from the thermal source. This last observation is corroborated by the geographic distribution of the veins (Figs. 2 and 3). With increasing distance of the mineralized structure from NNW structural trend that bounds to the east the San Dimas district, a more pronounced Sb enrichment is observed during the Oligocene Au-epithermal event.

Although Ag and Au mineralization exhibit structural, petrographic and chemical differences, “pure” veins (i.e., belonging only to one of these events) are uncommon. Most of the mineralized veins present a “mix or sum” of the two events characteristics. Therefore, they could represent two end-members of a continuum process as claimed by several authors (Enríquez et al., 2018 and references therein) or they could represent a proportional sum of two different events.

The development of a magmatic-hydrothermal system corresponds usually to a particular stage(s) of a more complex magmatic evolution (Simmons and Brown, 2006; Buret et al., 2016; Richards, 2018), including the evolution of magma in deep crustal intrusion zones, crustal melting processes, and emplacement of batholiths in higher crustal levels. These hydrothermal stage(s) could be unique, pulsatile, or

continuous over hundred thousand of years (Arribas et al., 1995; Garwin, 2002). They may occur in discrete periods of time, be overprinted by subsequent hydrothermal systems, or eroded by uplift and erosional processes (Garwin, 2002). Lovett (2003) and Sanchez-Alfaro et al. (2016) showed that in extreme cases gold veins may form over seconds by seismic depressurization. Metal precipitation may be so efficient that a giant epithermal gold deposit such as Ladolam (> 42 Moz) might have been formed in < 55,000 years (Simmons and Brown, 2006). In general, the occurrence of long-living hydrothermal systems is not a precondition for the genesis of large hydrothermal deposits.

The application of different geochronology methods to primary and secondary minerals represents a reliable tool to decipher the genesis of complex deposits. Such studies allow to understand and highlight the relationship between local/regional magmatic events and the hydrothermal systems. Furthermore, reliable geochronological data is essential to understand the geodynamic context and evolution of a deposit. Magmatic events are relatively easy to date by routine geochronological methods such as U/Pb zircon dating. However, dating of hydrothermal events is not straightforward and is often done by isotopic analysis of minerals with relatively low closure temperature (230 to 300 °C for K-Ar and $^{40}Ar/^{39}Ar$ in adularia and sericite) which are easily perturbed or may undergo recrystallization as in the case of hypogene alunite under supergene acidic conditions (Arribas et al., 1995; Lozano et al., 2018). This isotopic closure temperature range (lower than 300 °C) corresponds to most of the known epithermal systems in Mexico and worldwide (Hayba et al., 1985; Simmons, 1991; Sillitoe, 1993; Arribas et al., 1995; Hedenquist and Arribas, 1999; Sillitoe and Hedenquist, 2003; Einaudi et al., 2003; Simmons et al., 2005; Camprubí and Albinson, 2007). Within a polyphase hydrothermal system, long-lived or overprinted, older ages related to the initial mineralization event can be easily perturbed by subsequent hydrothermal fluids, which may blur temporal distinctions between discrete and spatially related hydrothermal systems. One of the consequences could be an apparent long-lived hydrothermal system, rather than one characterized by superposed systems that may have acted episodically over a period of time. To be able to distinguish a long-lived, albeit pulsatile, hydrothermal system from time-discrete overlapping hydrothermal systems, the mineralizing hydrothermal system must be studied in terms of its source, the conducts transferring the metals and the trap, all occurring in a unique geological episode. Any mineralized system presenting significant internal differences in chemistry, structures or ages would be the result of overlapping hydrothermal events.

Based on our sampling methodology, the petrography of the San Dimas veins and the shape of the $^{40}Ar/^{39}Ar$ step heating experiments we infer that all studied samples present a variable grade of isotopic resetting. The oldest ages, being plateau ages or higher temperature steps, are interpreted as a minimum age of the Ag-mineralization event at ~ 39–40 Ma. The younger plateau ages do not show a complete isotopic resetting and are interpreted as a maximum age of the Au-mineralization event at ~ 32 Ma. All the $^{40}Ar/^{39}Ar$ experiments yielding ages in the range 40 to 32 Ma show the highest spectra perturbation, so we conclude that they have no geological significance. Magmatic zircon U/Pb ages and trace element ratios distribution allow linking the corresponding magmatic and mineralizing hydrothermal events at ~41–40 Ma and ~30–29 Ma.

The Eocene-Oligocene magmatic evolution of the SMO and of most of central Mexico is comparable in age and chemistry and matches with the mineralization events. Eocene ages of mineralization, like those identified at San Dimas, are reported for other epithermal deposit in the SMO (~44 Ma K-Ar age for the Ag-Pb-Zn Topia deposit, Loucks, 1991; Loucks et al., 1988; Loucks and Petersen, 1988), and epithermal and skarn deposits of central Mexico (~47 Ma U-Pb age for the Zn-Ag Charcas deposit, Levresse et al., 2015; 42.36 ± 0.18 Ma, $^{40}Ar/^{39}Ar$ age for the Ag-Pb-Zn Zacatecas district, Zamora-Vega et al., 2018; 46.2 ± 1 Ma, K-Ar age for the San Martin Cu-deposit, Damon et al., 1981), which were developed along a crustal fault system that bounds the Mesa Central to the west-southwest (Nieto-Samaniego et al., 2005). With the exception of the Zacatecas district, all these deposits are genetically related to a geochemically anomalous plutonism with significant enrichment in large ion lithophile elements (LILE) and Ba (Chávez Cabello, 2005; Damon et al., 1981; González García, 2016; Mascuñano et al., 2013; Patterson, 2001; Poliquin, 2009; Rubin and Kyle, 1988; Velasco Tapia et al., 2011). The petrogenetic model proposed for these granitoids and related mineralization involves partial melting of a metasomatized mantle in a post-orogenic scenario (González García, 2016; Mascuñano et al., 2013; Velasco Tapia et al., 2011). Geodynamically, they illustrate the magmatic transition from the Cretaceous-Paleocene calc-alkaline magmatism related to normal supra-subduction arc dynamics to Oligocene-early Miocene anhydrous and bimodal magmatism related to lithospheric extension associated to a growing slab window (Ferrari et al., 2018a). In this framework, the role of the Eocene Piaxla batholith as a thermal and metal source for the Ag-dominant mineralization in the San Dimas district, strongly questions the intermediate sulfidation epithermal model previously suggested for this event.

In the San Dimas district as well as in the southern part of the SMO, the Au-dominant low sulfidation veins are clearly related to Oligocene rhyolitic domes, aligned within a long NNW-SSE extensional to transtensional corridor that marks the limit of the unextended core of the SMO (Tayoltita-Pueblo Nuevo fault system of Ferrari et al., 2013) (Fig. 2). This mineralizing event is comparable in age, structural and geological context to most of the historic Ag-mining districts in central Mexico (Ag-Au epithermal Zacatecas district: Tristán-González et al., 2012; Zamora-Vega et al., 2018; Ag-Au epithermal Fresnillo district: Velador et al., 2010; Ag-Au epithermal Guanajuato district: Moncada et al., 2012, 2017; Nieto-Samaniego et al., 2016; Angeles Moreno et al., 2017; Ag-Au epithermal Taxco district: Hernandez Vargas et al., 2017).

A succession of magmatic and tectonic events must have been superposed to create a large Ag/Au deposit like the San Dimas district. The first mineralization event associated to Cu-porphyry intrusions developed as part of the Laramide magmatic arc in Late Cretaceous to early Paleocene times, similarly to other deposits in Sonora, Arizona and New Mexico. This first mineralization is uneconomic but was likely instrumental in the development of the second and most prolific Ag-dominated mineralization event, in which silver mineralization is genetically related to the end of the Piaxtla batholith emplacement at ~43 Ma. The related hydrothermal system is structurally controlled, of relatively high temperature (up to 400 °C), neutral pH (adularia and calcite) and with intermediate sulfidation fluids. The building of the Piaxtla batholith is related to the initiation of lithospheric extension characterized by high rate of exhumation and erosion, which allowed the rapid uplift of the batholith and the related Ag mineralized veins to a shallower crustal level. The last mineralization event occurring at ~30–29 Ma resulted in what is considered a classic Mexican low sulfidation epithermal Au vein deposit. Mineralized veins are genetically related to rhyolitic domes emplaced along north-northwest transcurrent faults systems. The related hydrothermal system is structurally controlled, of relatively low temperature (up to 250 °C), low-acidic to neutral pH (alunite and sericite), with low sulfidation fluids and occurred at shallow depth. At a regional level, it coincides with the Oligocene-early Miocene synextensional voluminous bimodal volcanism of the SMO with pulses at 31–29 Ma, and 24–20 Ma (Ferrari et al., 2018a).

The detailed analysis of the classic San Dimas epithermal deposit presented in this contribution suggests that the traditional view for the formation of large polymetallic Mexican deposit need to be revised. As in San Dimas, it is very likely that the idea of a single, protracted hydrothermal system cannot resist a detailed geological and geochronological evaluation. The richness of the large silver and gold Mexican deposits could be explained by the superposition in space and time of specific geological events within a favorable geodynamic evolution. The formation of the San Dimas district with its exceptionally rich Ag-Au

mineralization resides in the late Eocene to Early Oligocene uplift that allowed the overprinting of originally deeper Ag veins by a shallower Au mineralizing event and their final exposition favored by the Oligocene-early Miocene extension that produced the erosion of the local volcanic cover. More importantly, geology and fluid geochemistry of each mineralizing event are coherent within the geodynamic evolution of the area, showing a transition from a magmatic arc to a continental extension regime.

Acknowledgments

This research is part of the PhD project of the first author at Universidad Nacional Autónoma de México (UNAM) Postgraduate Program. The research was funded by CONACYT grant CB 237745-T to L. Ferrari and DGAPA-PAPIIT grant IN106017 to G. Levresse. We thank Primero Mining (presently First Majestic Silver Corp.) for sharing unpublished information and for logistical support. Special thanks to Nicolas Landón for his strong support in the initial phase of the research and to Miguel Pérez for sharing his knowledge on the ore geology of the central SMO. We also thank Carlos Ortega for assistance with U-Pb dating, Margarita Lopez (CICESE, Mexico) for assistance with ^{40}Ar-^{39}Ar dating, A. Susana Rosas Montoya y Miguel Angel García García for sample preparation for Ar-Ar dating, Carlos Linares for assistance with the Electron Probe X-Ray Microanalyzer at Laboratorio Universitario de Petrologia, Instituto de Geofisica, UNAM, Mexico, Marina Vega for assistance at Laboratorio de Fluidos Corticales, Centro de Geociencias, UNAM, and Juan Tomás Vazquez for the elaboration of thin sections. Authors are special grateful to Seequent for sharing an academic Leapfrog Mining license and Santiago Urquiza for his help in the petrographic study of veins. We thank Peter Lightfoot, Erme Enriquez and three anonymous reviewers for their constructive comments that give us the opportunity to greatly improve the initial version.

Appendix A. Supplementary data

Supplementary data to this article can be found online at https://doi.org/10.1016/j.oregeorev.2019.103195.

References

Albinson, T.F., 1978. Fluid inclusion studies in the Tayoltita mine and related areas, Durango, Mexico. Unpublished M.S. thesis, Minnesota University, p. 90.
Angeles-Moreno, E.A., Nieto-Samaniego, A.F., Ruiz Gonzalez, F.J., Levresse, G., Alaniz-Alvarez, S.A., Moya, M.J. Paulina Olmos, Xu, S., Miranda Aviles, R., 2017. The transition between shortening and extensional regimes in central Mexico recorded in the tourmaline veins of the Comanja Granite. J. S. Am. Earth Sci. 73, 65–77.
Arribas Jr, A., Hedenquist, J.W., Itaya, T., Okada, T., Concepción, R.A., Garcia Jr, J.S., 1995. Contemporaneous formation of adjacent porphyry and epithermal Cu-Au deposits over 300 ka in northern Luzon, Philippines. Geology 23 (4), 337–340.
Ballard, J.R., Palin, J.M., Campbell, I.H., 2002. Reative oxidation states of magmas inferred from Ce(IV)/Ce(III) in zircon: application to porphyry copper deposits of northern Chile. Contribution to Mineralogy and Petrology 144, 347–364.
Bornhorst, T.J., Nurmi, P.A., Rasilainen, K., Kontas, E., 1995. Trace element characteristics of selected epithermal gold deposits of North America: Special Paper of the Geological Survey of Finland 20, 47–52.
Bryan, S., Ferrari, L., 2013. Large igneous provinces and silicic large igneous provincies: progress in our understanding over the last 25 years. Geol. Soc. Am. Bull. 125, 1053–1078.
Buchanan, L.J., 1980. Ore controls of vertically stacked deposits, Guanajuato, Mexico. American Institute of Mining Engineers 80–82.
Buret, Y., von Quadt, A., Heinrich, C., Selby, D., Walle, M., Peytcheva, I., 2016. From a long-lived upper-crustal magma chamber to rapid porphyry copper emplacement: reading the geochemistry of zircon crystals at Bajo de la Alumbrera (NW Argentina). Earth Planet. Sci. Lett. 450, 120–131.
Camprubí, A., Ferrari, L., Cosca, M., Cardellach, E., Canals, A., 2003. Ages of epithermal deposits in Mexico: regional significance and links with the evolution of Tertiary volcanism. Econ. Geol. 98, 1029–1037.
Camprubi, A., Albinson, T., 2007. Epithermal deposits in México—update of current knowledge, and an empirical reclassification. Special Paper of the Geological Society of America 422, 377–415.
Camprubi, A., 2013. Tectonic and metallogenic history of Mexico. Society of Economic Geology Special Paper Publication 17, 201–243.
Chávez Cabello, G., 2005. Deformación y magmatismo cenozoicos en el sur de la Cuenca de Sabinas, Coahuila, México. Tesis doctoral. Juriquilla, Querétaro. Centro de Geociencias, Universidad Nacional Autónoma de México p. 266.
Clarke, M., 1986. Hydrothermal geochemistry of Ag-Au veins in the Tayoltita and the San Dimas mining district, Durango and Sinaloa, Mexico. Unpublished Ph.D. thesis, p. 151.
Clarke, M., Titley, S., 1988. Hydrothermal evolution in the formation of silver-gold veins in the Tayoltita mine, San Dimas district, Mexico. Society of Economic Geologist 1830–1840.
Cole, D.R., Drummond, S.E., 1986. The effect of transport and boiling on Ag/Au ratios in hydrothermal solutions: a preliminary assessment and possible implications for the formation of epithermal precious-metal ore deposits. Journal of Geochemical Exporation 25 (1–2), 45–79.
Conrad, M.E., Petersen, U., O'Neil, J.R., 1992. Evolution of an Au-Ag-producing hydrothermal system : the Tayoltita mine, Durango, mexico. Econ. Geol. 87 (6), 1451–1474.
Coyle, D.A., Wagner, G.A., 1998. Positioning the titanite fission-track partial annealing zone. Chem. Geol. 149 (1–2), 117–125.
Damon, P.E., Shafiqullah, M., Clark, K.F., 1981. Age trends of igneous activity in relation to metallogenesis in the southern Cordillera: Arizona Geological Society Digest 14, 137–154.
Davidson, S.C., 1932. Geology and ore deposit of Tayoltita, District of San Dimas, Durango, Mexico (Ph.D. Dissertation). Harvard University, pp. 172.
Dilles, J.H., Kent, A.J.R., Wooden, J.L., Tosdal, R.M., Koleszar, A., Lee, R.G., Farmer, L.P., 2015. Zircon compositional evidence for sulfur-degassing from ore-forming arc magmas. Econ. Geol. 110, 241–251.
Einaudi, M.T., Hedenquist, J.W., Inan, E., 2003. Sulfidation state of fluids in active and extinct hudrothermal systems: transitions from porphyry to epithermal environments. Society of Economic Geologist Special Publication Series 10, 285–313.
Enriquez, E., Rivera, R., 2001a. Geology of the Santa Rita Ag-Au Deposit, San Dimas District, Durango, Mexico. Society of Economic Geologists 8, 39–58.
Enriquez, E., Rivera, R., 2001b. Timing of magmatic and hydrothermal activity in the San Dimas District, Durango, Mexico, en New Mines and Mineral Discoveries in Mexico and Central America. Society of Economic Geologist Special Publication 8, 33–38.
Enríquez, E., A. Iriondo, and A. Camprubí, A., 2018. Geochronology of Mexican mineral deposit. VI: the Tayoltita low-sulfidation epithermal Ag-Au district, Durango and Sinaloa. Boletín de la Sociedad Geológica Mexicana 70, 2, 531-547.
Ferrari, L., López-Martínez, M., Rosas-Elguera, J., 2002. Ignimbrite flareup and deformation in the southern Sierra Madre Occidental, western Mexico: Implications for the late subduction history of the Farallon Plate. Tectonics 21. https://doi.org/10.1029/2001TC001302.
Ferrari, L., Orozco-Esquivel, T., Manea, V., Manea, M., 2012. The dynamic history of the Trans-Mexican Volcanic Belt and the Mexico subduction zone. Tectonophysics 522–523, 122–149. https://doi.org/10.1016/j.tecto.2011.09.018.
Ferrari, L., Valencia-Moreno, M., Bryan, S., 2007. Geology of the western Mexican volcanic belt and adjacent Sierra Madre Occidental and Jalisco block. Geol. Soc. Am. Spec. Pap. 334, 65–83.
Ferrari, L., López-Martínez, M., Orozco-Esquivel, T., Bryan, S.E., Duque-Trujillo, J., Lonsdale, P., Solari, L., 2013. Late Oligocene to Middle Miocene rifting and synextensional magmatism in the southwestern Sierra Madre Occidental, Mexico: the beginning of the Gulf of California rift. Geosphere. https://doi.org/10.1130/GES00925.1.
Ferrari, L., Orozco-Esquivel, T., Bryan, S., Lopez-Martínez, M., Silva-Fragoso, A., 2018a. Cenozoic extension and magmatism in western Mexico: linking the Sierra Madre Occidental Silicic Large Igneous Province and the Comondú Group with the Gulf of California rift. Earth Sci. Rev. 183, 115–152.
Ferrari, L., Orozco Esquivel, T., Lopez Martinez, M., Martinez Resendiz, V., Avalos Ledesma, A., 2018b. Geochronology and isotope geochemistry of the mafic volcanism of the Sierra Madre Occidental silicic large igneous province, Mexico: implications for the Cenozoic geodynamics of western North America. 11th South American Symposium on Isotope Geology (SSAGI).
Gastil, P., 1975. Plutonic zones in the Peninsular Ranges of southern California and northern Baja California. Geology 3, 361–363.
González García, H.A., 2016. (MSc thesis). Metalogenia del skarn en Xichu, Guanajuato UNAM pp. 112.
Gray, J.E., Goldfarb, R.J., Detra, D.E., Slaughter, K.E., 1991. Geochemistry and exploration criteria for epithermal cinnabar and stibnite vein deposits in the Kuskokwim River region, southwestern Alaska. J. Geochem. Explor. 41, 363–386.
Hall, B.V., Gorzynski, G.A., Hulme, N.J., Vila-Sánchez, A.R., Díaz-Martínez, R., Cham-Domínguez, C., Limón Gallegos, F., Luis Aldana, J., 2014. Structural setting and metal zoning of the Ag-Au veins of the Real de Minas de Zacualpan District. Central Mexico, SEG meeting, Whistler.
Hayba, D.O., Bethke, P.M., Heald, P., Foley, N.K., 1985. Geologic, Mineralogic, and Geochemical Characteristics of Volcanic-Hosted Epithermal Precious-Metal Deposits. Geology and Geochemistry of Epithermal Systems. Reviews in Economic Geology 2, 129–167.
Hedenquist, J.W., Arribas Jr., A., 1999. Epithermal gold deposits: I. Hydrothermal processes in intrusion-related systems, ans II. Characteristics, examples and origin of epithermal gold deposits. Society of Economic Geologist 31, 13–63.
Henry, C.D., 1975. Geology and geochronology of the granitic batholithic complex, Sinaloa. Unpublished PhD, Mexico, pp. 159.
Henry, C., McDowell, F., Silver, L., 2003. Geology and geochronology of granitic batholithic complex, Sinaloa, México: implications for Cordilleran magmatism and tectonics. Geol. Soc. Am. Spec. Pap. 374, 237–273.
Henshaw, P.C., 1953. Geology and Ore Deposit of the San Dimas District. Sinaloa and Durango, Private document, pp. 531.
Hernandez Vargas, J.J., Martiny, B., Moran Zenteno, D.J., Perez Gutierrez, R., Lopez

Martinez, M., 2017. $^{40}Ar/^{39}Ar$ geochronology and revised stratigraphy of the late Eocene Taxco volcanic field, southern Mexico. J. S. Am. Earth Sci. 79, 40–56.
Horner, J., Enriquez, E., 1999. Epithermal precious metal mineralization in a strike-slip corridor: The San Dimas District, Durango, Mexico. Soc. Econ. Geologist 1375–1380.
Garwin, S., 2002. The Geologic Setting of Intrusion-Related Hydrothermal Systems near the Batu Hijau Porphyry Copper-Gold Deposit, Sumbawa, Indonesia. In R. J. Goldfarb, & R. L. Nielsen (Eds.), Integrated Methods for Discovery: Global Exploration in the Twenty-First Century (Denver, Colorado, USA ed., Vol. 9, pp. 333-366). Colorado, USA: Society of Economic Geologists.
Hynes, S.E., 1999. Geochemistry of Tertiary epithermal Ag-Pb-Zn veins in Taxco, Guerrero, Mexico. Sudbury, Ontario, Laurentian University, National Library of Canada, Unpublished M.Sc. thesis, pp. 158.
Keller, P.C., 1974. Mineralogy of the Tayoltita Gold and Silver Mine, Durango, Mexico. University of Texas (M.Sc. Thesis). University of Texas, pp. 123.
Levresse, G., Doberganes Bueno, J., Nieto-Samaniego, A., 2015. Magmatic Evolution of Charcas Zn Distal Skarn. 13th SGA Biennial Meeting, Proceedings. 1. Society for Geology Applied to Mineral Deposits, pp. 137–140.
Levresse, G., Villarreal-Fuentes, J., Nieto-Samaniego, A.F., Alexandre, P., Corona-Esquivel, R., Solé Viñas, J., 2017. New metallogenic model of telescoped Eocene-Miocene Au-U epithermal mineral deposit in the Placer de Guadalupe district, Chihuahua, Mexico. Ore Geol. Rev. 91, 133–152.
Loucks, R.R., 1991. Polymetallic epithermal fissure vein mineralization, Topia, Durango, Mexico: part II. Silver Mineral chemistry and high-resolution patterns of chemical zoning in vein, a reply. Econ. Geol. 86, 1120–1129.
Loucks, R.R., Lemish, J., Damon, P.E., 1988. Polymetallic epithermal vein mineralization, Topia, Durango, Mexico: Part I District geology, geochronology, hydrothermal alteration, and vein mineralogy. Econ. Geol. 83, 1499–1528.
Loucks, R.R., Petersen, U., 1988. Polymetallic epithermal fissure vein mineralization, Topia, Durango, Mexico: Part II. Silver mineral chemistry and high resolution patterns of chem- ical zoning in veins. Econ. Geol. 83, 1529–1559.
Lovett, R.A., 2003. Earthquakes make gold veins in an instant Nature, 12615.
Lozano, A., Fernández-Martínez, A., Ayora, C., Poulain, A., 2018. Local structure and ageing of basaluminite at different pH values and sulphate concentrations. Chem. Geol. 496, 25–33. https://doi.org/10.1016/j.chemgeo.2018.08.002.
Lu, Y.J., Louks, R.R., Fiorentini, M., McCuaig, C., Evans, N.J., Yang, Z.M., Hou, Z.Q., Kirkland, C.L., Parra Avila, L.A., Kobussen, A., 2016. Zircon Compositions as a pathfinder for porphyry Cu-Mo-Au deposits, Special publication 19. Society of Economic Geologist 329–347.
Ludwig, K.R., 2008. Useŕs manual fro Isoplot 3.7. A geochronological toolkit for Microsoft Excel. Berkeley Geochronology Center Special Publication 4 pp. 77.
Mango, H., Arehart, G., Oreskes, N., Zantop, H., 2014. Origin of epithermal Ag-Au-Cu-Pb-Zn mineralization in Guanajuato, Mexico. Miner. Deposita 49, 119–143.
Mascuñano, E., Levresse, G., Cardellach, E., Tritlla, J., Corona-Esquivel, R., Meyzen, C., 2013. Post-Laramide. Eocene magmatic activity in Sierra de Catorce, San Luis Potosi, Mexico: Revista Mexicana de Ciencias Geólogicas 30 (2), 299–311.
McDowell, F., Keizer, R., 1977. Timing of mid Tertiary volcanism in the Sierra Madre Occidental between Durango City and Mazatlán, Mexico. Geol. Soc. Am. Bull. 88, 1479–1487.
McDowell, F., Roldán-Quintana, J., Connelly, J., 2001. Duration of Late Cretaceous-early Tertiary magmatism in east-central Sonora, Mexico. Geol. Soc. Am. Bull. 113, 521–531.
McDowell, F., McIntosh, W., 2012. Timing of intense magmatic episodes in the northern and central Sierra Madre Occidental, western. Geosphere 8, 1505–1526.
Moncada, D., Baker, D., Bodnar, R., 2017. Mineralogical, petrographic and fluid inclusion evidence for the link between boiling and epithermal Ag-Au mineralization in the La Luz area, Guanajuato Mining District, México. Ore Geol. Rev. 89, 143–170.
Moncada, D., Mutchler, S., Nieto, A., Reynolds, T.J., Rimstidt, J.D., Bodnard, R.J., 2012. Mineral testure and fluid inclusion petrography of the epithermal Ag-Au deposits at Guanajuato, Mexico: application to exploration. J. Geochem. Explor. 114, 20–35.
Montoya-Lopera, P.A., Ferrari, L., Levresse, G., Mata, L., 2019. New insights into the geology and tectonics of the San Dimas mining district, Sierra Madre Occidental, Mexico. Ore Geol. Rev. 105, 273–294.
Nieto-Samaniego, A.F., Alaniz-Alvarez, S.A., Camprubi, A., 2005. La Mesa Central de Mexico: estratigrafía, estructura y evolución tectónica cenozoica: Boletín de la Sociedad Geólogica Mexicana 52, 3, 285–318.
Nieto-Samaniego, A.F., Baez-Lopez, J.A., Levresse, G., Alaniz-Alvarez, S.A., Ortega-Obregon, C., Lopez-Martinez, M., Noguez-Alcantara, B., Sole-Vinas, J., 2016. New stratigraphic, geochronological, and structural data from the southern Guanajuato Mining District, Mexico: implications for the caldera hypothesis. Int. Geol. Rev. 58 (2), 246–262.
Ortega-Gutiérrez, F., Elías-Herrera, M., Morán-Zenteno, D., Solari, L., Luna-González, L., Schaaf, P., 2014. A review of batholiths and other plutonic intrusions of Mexico. Gondwana Res. 26, 834–868. https://doi.org/10.1016/j.gr.2014.05.002.
Patterson, K.M., 2001. Structural controls on Minrelaization and constraints on fluid evolution at the Sacrificio Cu (Zn, Pb, Ag, Au) skarn, Durango, Mexico. The University of British Columbia, Mexico, pp. 192.
Poliquin, M.J., 2009. Geology, Geochemistry and Age of Intrusion related mineralization in Eastern Mexico (PhD dissertation). University of Exeter, pp. 408.
Ramos-Rosique, A., Bryan, S.E., Ferrari, L., López-Martínez, M., Rankin, A., Camprubí, A., Reiners, P., 2011. Chronology of mid-Cenozoic magmatism and epithermal mineralization in the Bolaños graben, southern Sierra Madre Occidental, Mexico. In 11th SGA Biennial Meeting—Let's talk ore deposits, Ediciones Universidad Católica del Norte, Antofagasta, Chile. Vol. 1, 139-141).
Richards, J.P., 2018. A Shake-Up in the Porphyry World? Econ. Geol. 113 (6), 1225–1233.
Rubin, J.N., Kyle, J.R., 1988. Mineralogy and Geochemistry of the San Martin Skarn Deposit, Zacatecas, Mexico. Econ. Geol. 83, 1742–1801.
Sanchez Alfaro, P., Reich, M., Driesner, T., Cembrano, J., Arancibia, G., Perez Flores, P., Heinrich, C.A., Tardani, D., Lange, D., Campos, E., 2016. The optimal windows for seismically-enhanced gold precipitation in the epithermal environment. Ore Geology Review 79, 463–473.
Sanders, J.A., Brueseke, M., 2012. Volatility of Se and Te during subduction related distillation and the geochemistry of epithermal ores of the western United States. Econ. Geol. 107, 165–172.
Sillitoe, R.H., 1993. Epithermal models: genetic types, geometrical controls and shallow features. In: Kirkham, R.V., Sinclair, W.D., Thorpe, R.I., Duke, J.M. (eds.), Mineral Deposit Modeling: Toronto, Geological Association of Canada, Special Paper, 40, 403-417.
Sillitoe, R.H., 1999. Styles of high-sulphidation gold, silver and copper mineralisation in porphyry and epithermal environments. In: Weber, G. (Ed.), Pacrim '99 Proceedings. Bali, Indonesia, Australasian Institute of Mining and Metallurgy, Melbourne, pp. 29–44.
Sillitoe, R., Hedenquist, J.J., 2003. Linkages between volcanotectonic settings, ore-fluid compositions, and epithermal precious-metals deposits. Special Publication. Society of Economic Geologist 10 (18), 1–73.
Silver Institute, 2017. World silver survey 2017. The Silver Institute 1112 16th Street, NW, Suite 240 Washington DC.
Simmons, S.F., 1991. Hydrologic implications of alteration and fluid inclusion studies in the Fresnillo District, Mexico. Evidence for a brine reservoir and a descending water table during the formation of hydrothermal Ag-Pb-Zn orebodies. Econ. Geol. 86, 1579–1601.
Simmons, S.F., White, N.C., John, D.A., 2005. Geological characteristics of epithermal precious and base metal deposits. Society of Economic Geologist 100th Aniversary, 485-522.
Simmons, S.F., Brown, K.L., 2006. Gold in magmatic hydrothermal solutions and the rapid formation of a giant ore deposit. Science 314, 288–291.
Smith, D.M., Hall, D.K., 1974. Geology of the Tayoltita mine. Society of Mining Engineers of A.I.M.E, Durango, Mexico, pp. 48.
Smith, D., Albinson, T., Sawkins, F., 1982. Geologic and fluid inclusion studies of the Tayoltita silver-gold vein deposit, Durango. Mexico. Economic Geology 1120–1145.
Tristán-González, M., Torres-Hernández, J.R., Labarthe-Hernández, G., Aguillón-Robles, A., Yza-Guzmán, R., 2012. Control estructural para el emplazamiento de vetas y domos félsicos en el distrito minero de Zacatecas. Boletín de la Sociedad Geológica Mexicana 64 (3), 353–367.
Valencia-Moreno, M., Camprubi, A., Ochoa Landin, L., Calmus, T., Mendivil Quijada, H., 2017. Latest Cretaceous-early Paleogene "boom" of porphyry Cu mineralization associated with the Laramide magmatic arc of Mexico. Ore Geology Review 81, 1113–1124.
Velador, J.M., Heizler, M.T., Campbell, A.R., 2010. Timing of magmatic activity and mineralization and evidence of a long-lived hydrothermal system in the Fresnillo silver district, Mexico: Constraints from 40Ar/39Ar geochronology. Econ. Geol. 105 (7), 1335–1349.
Velasco Tapia, F., Gonzalez Guzman, R., Chavez Cabello, G., Lozano Serna, J., Valencia Moreno, M., 2011. Estudio petrográfico y geoquímico del Complejo Plutónico El Peñuelo (Cinturón de Intrusivos de Concepción del Oro), noreste de México. Boletin de la Sociedad Geologica Mexicana 63, 183–199.
Wilson, F.O., Rocha, S., 1949. Coal deposits of the Santa Clara distric near Tónichy, Sonora, Mexico. U.S. Geol. Surv. Bull. 962A, 80.
Zamora-Vega, O., Richards, J.P., Spell, T., Dufrane, S.A., Williamson, J., 2018. Multiple mineralization events in the Zacatecas Ag-Pb-Zn-Cu-Au district, and their relationship to the tectonomagmatic evolution of the Mesa Central, Mexico. Ore Geol. Rev. 102, 519–561.

Capítulo 4: **Genesis of the telescoped Eocene silver and Oligocene gold San Dimas deposits, Sierra Madre Occidental, Mexico: constraints from fluid inclusions, oxygen - deuterium and noble gases isotopes.**

Ore Geology Reviews 120 (2020) 103427

Contents lists available at ScienceDirect

Ore Geology Reviews

journal homepage: www.elsevier.com/locate/oregeorev

Genesis of the telescoped Eocene silver and Oligocene gold San Dimas deposits, Sierra Madre Occidental, Mexico: Constraints from fluid inclusions, oxygen - deuterium and noble gases isotopes

Paula Montoya-Lopera[a], Gilles Levresse[b,*], Luca Ferrari[b], Andrea Luca Rizzo[c], Santiago Urquiza[a], Luis Mata[d]

[a] Posgrado en Ciencias de la Tierra, Universidad Nacional Autónoma de Mexico, Campus Juriquilla, 76230, Queretaro, Qro., Mexico
[b] Centro de Geociencias, Universidad Nacional Autónoma de Mexico, Campus Juriquilla, 76230, Queretaro, Qro., Mexico
[c] Istituto Nazionale di Geofisica e Vulcanologia, Sezione di Palermo, 90146 Palermo, Italy
[d] First Majestic Silver Corp., Tayoltita, Dgo., Mexico

ARTICLE INFO

Keywords:
San Dimas Ag–Au district
Fluid inclusions
D-O stable isotope
Noble gases
Telescoped ore deposits

ABSTRACT

The San Dimas district is a world-class Ag/Au deposit, developed as a telescoped Eocene-Oligocene Ag/Au mineralization located in the Sierra Madre Occidental (SMO) of western Mexico. San Dimas exhibits multiple mineralization events during different magmatic and tectonic episodes from Late Cretaceous to early Oligocene. The well-preserved magmatic-hydrothermal system provides an excellent opportunity to determine the source of silver and gold, the evolution of the hydrothermal fluids, and the controls on the mineralization precipitation. Mineralogical, fluid inclusions (FI), stable and noble gases isotope analyses suggest that the San Dimas deposit consist of two different mineralization styles: 1) Ag-dominant epithermal Eocene veins that occurred at temperatures up to ~350 °C developed at ca. 2–3 km depth, associated to the final stages of intrusion of the Piaxtla batholith, with FI dominated by a crustal component, and 2) epithermal low sulfidation Au-dominant Oligocene veins which were developed at 250 °C, at shallower depths (< 1 km), associated to the feeding fractures of rhyolitic domes developed at the end of the main ignimbrite flare up of the SMO, with FI showing crustal fluids variably mixed with a magmatic component. Our results highlight the importance of a multidisciplinary approach, such as field observations, geochronological and geochemical studies, to better understand the complexity of the hydrothermal magmatic processes involved in the formation of many Mexican ore deposits and their proper classification.

1. Introduction

Since the early 20th century, economic geologists have recognized epithermal deposits as being important sources of silver and gold (Lindgren, 1922). More than 6000 tons of gold (Au) resources have been proven from worldwide epithermal systems and keep growing (Kerrich et al., 2000; Chen et al., 2003, 2012; Zhang et al., 2019). In the still valid original description of Lindgren (1922, 1933), an epithermal deposit is usually defined as the "sub-aerial volcanic-hosted types". The typical characteristics of this kind of deposits are a structurally controlled extensional vein system, geographically and chronologically associated to a volcanic center (usually rhyolite domes) that formed in a shallow environment (< 1 km below the water table) and involving predominantly near neutral chloride waters (mostly of meteoric origin) at relative low temperatures (typically 150–300 °C) and low sulfidation (LS) mineralogy (Heald at al., 1987; Panteleyev, 1996; White, 2003; Pirajno, 2009). Later, Heald et al., (1987), Hedenquist (1987), and Simmons et al., (2005) among many others, described comparable mineralized structure related to deeper porphyries mineralization environments. These are characterized by acidic magmatic fluids (high temperature and salinity), deeper metals precipitation, gangue and alteration mineralogy (alunite, dickite, kaolinite) and related to high sulphidation (HS) state. These well-defined genetic models can be seen as two pure end-members of a common family, since many epithermal-like deposits do not fit in them. To solve this problem, John (1999), John et al., (1999) and Hedenquist and Arribas (2000) proposed a third epithermal class named intermediate-sulfidation (IS) type to explain and regroup the large variety of the structurally controlled deposits,

* Corresponding author.
E-mail address: glevresse@geociencias.unam.mx (G. Levresse).

https://doi.org/10.1016/j.oregeorev.2020.103427
Received 30 October 2019; Received in revised form 12 February 2020; Accepted 18 February 2020
Available online 21 February 2020
0169-1368/

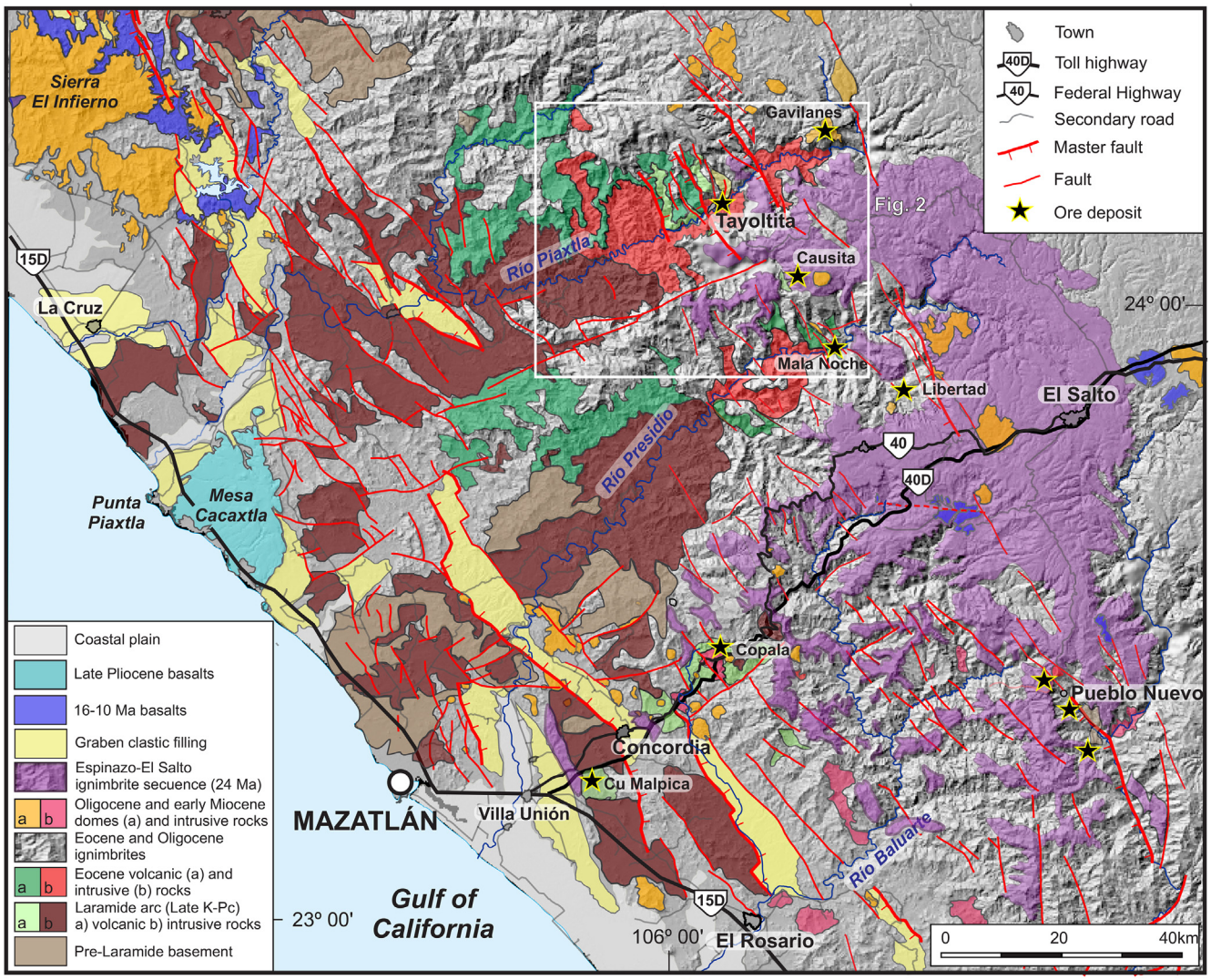

Fig. 1. Regional geologic map of central Sierra Madre Occidental showing the main post-Eocene extensional structures and the principal mining districts (modified from Henry and Fredrikson, 1987, and Ferrari et al., 2013). Insert show the spatial distribution of the Sierra Madre Occidental (SMOc) volcanic province and the San dimas district (SDD) location.

from Cordilleran polymetallic to carbonate-base metal Au deposits (Einaudi, 1992; Leach and Corbett, 1994; Wang et al., 2019 and references therein).

In Mexico, a review of epithermal deposit classification, including the classic San Dimas Au/Ag district, was proposed by Camprubi and Albinson (2007). The size of the Mexican silver and gold anomaly is illustrated by the outstanding play of Mexico mining during XVI and XVII centuries and its last ten years position as the largest silver (200 Moz/year) and eighth gold producer (125 t/year) worldwide. Most of this production comes from localities within the Sierra Madre Occidental province (SMO) and the magmatic events related to its formation. The chronological distribution of epithermal deposits coincides with the three main Cenozoic volcanic pulses of the SMO, which record a broad migration from the northwest to the southeast, where the last ignimbrite flare-up occurred (Ferrari et al., 2007, 2018; Ramos-Rosique et al., 2010; Fig. 1). The age of the most fertile events ranges from 36 to 28 Ma and includes all the giant Ag–Au–Sn and IOCG mining districts (Camprubí, 2013). Few epithermal deposits in México are known to have formed under an acid chemical regime. In fact, HS deposits were only recognized in Sonora state, in close relationship to the Cu-porphyry province (Camprubí, 2013). The recent re-evaluation of various historical Au/Ag districts (Guanajuato, Moncada et al., 2012, 2017; Fresnillo, Velador, 2010; Zacatecas, Zamora-Vega et al., 2018; San Dimas, Montoya et al., 2019b) is modifying several crucial concepts about timing, formation, and metals sources of the dominant intermediate and low sulfidation Mexican epithermal deposits. Some of them, traditionally classified as intermediate sulfidation, are now reinterpreted as telescoped deposits, formed during separate volcanic events sometimes under different geodynamic contexts (Zamora-Vega et al., 2019; Montoya-Lopera et al., 2019b).

In this study, we report on the description and geochemistry of fluid inclusions (FI) hosted in the Eocene silver-dominant and Oligocene gold-dominant mineralizing deposits found in the San Dimas district (Fig. 1). Building on recent geological, geochronological and geochemical studies (Montoya et al., 2019a; Montoya-Lopera et al., 2019b), we describe the TPX evolution of the ore-forming fluids and the ore genesis, to finally propose a new metallogenic model for the San Dimas Ag/Au deposit.

2. San Dimas local geology and mineralization settings

The San Dimas stratigraphic column can be divided into two major igneous successions that correspond to the Lower Volcanic Complex (LVC) and Upper Volcanic Supergroup (UVS) of the SMO, separated by

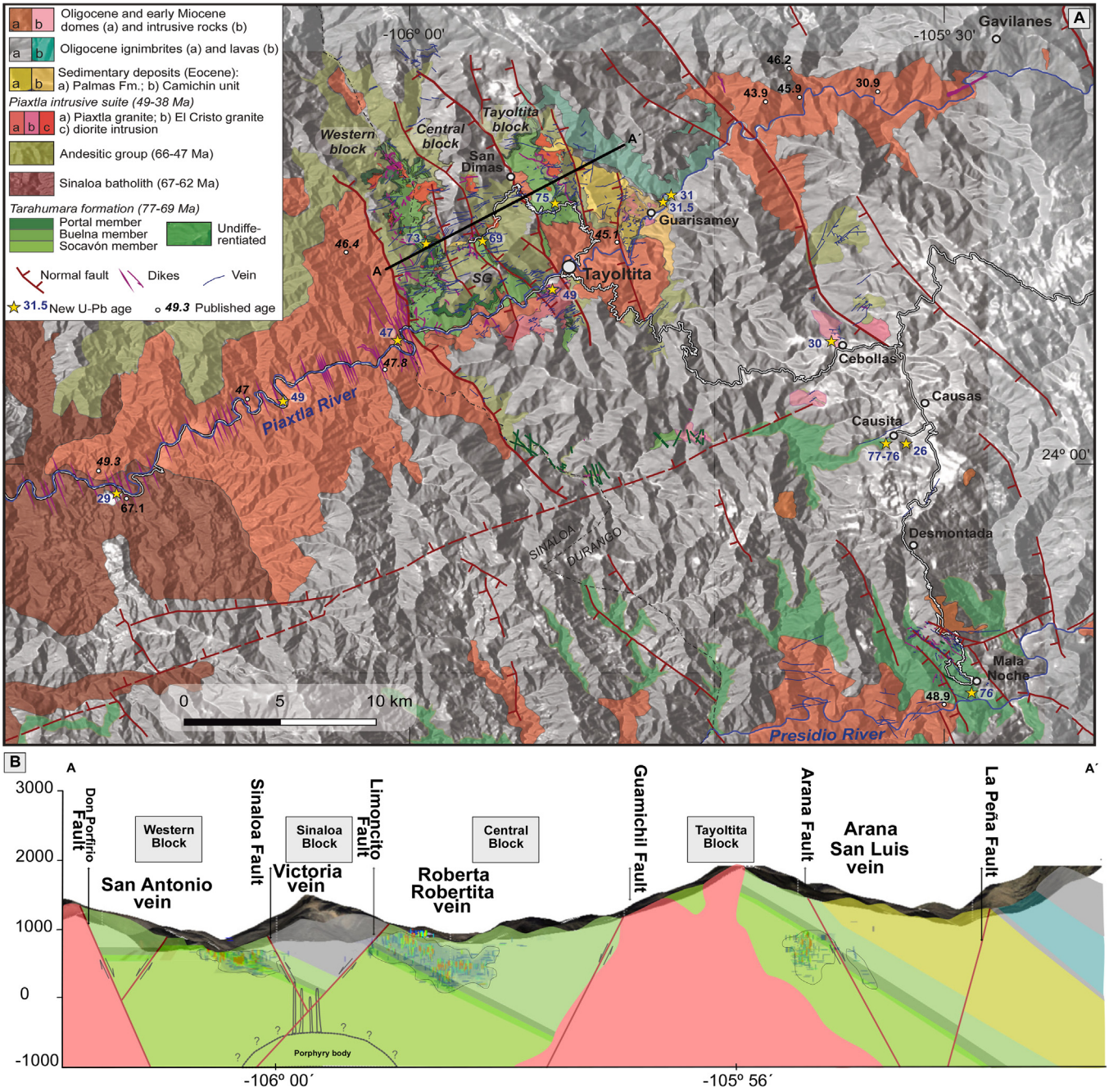

Fig. 2. (A) Geologic map of San Dimas mining district and Causita and Mala Noche southern extension, with location of published ages (from Montoya et al., 2019a) and sampled veins. (B) Simplified geological cross-section of the Ag/Au San Dimas district.

erosional and depositional unconformities. A detailed description of the lithology, petrography and geochronology of the stratigraphic column is given in Montoya et al., (2019a) and is briefly summarized here.

The Late Cretaceous to Eocene LVC, is composed of four volcanic members locally named "Socavón rhyolite", "Buelna andesite", "Portal rhyolite" and the Andesitic Group (Henshaw, 1953; Montoya et al., 2019a; Fig. 2). The LVC consists of an alternating suite of rhyolitic and andesite lavas flows locally intruded by felsic porphyritic bodies (Montoya et al., 2019a). The entire LVC volcanic column is crosscut and locally assimilated by the late Eocene Piaxtla batholith and its porphyritic dikes swarm (49.1–45.2 Ma; Henry et al., 2003; Montoya et al., 2019a). The transition between the LVC and the UVS is marked by the Las Palmas and Camichin continental sedimentary formations with a maximum age of deposition of ~52 Ma and ~43 Ma, respectively (Montoya et al., 2019a). The UVC unconformably covers the La Palmas and Camichin formations, the Piaxtla batholith and the Andesite Group. It is composed by two successions of silicic ignimbrites with ages of ~31.5 to 29 Ma and ~24 Ma respectively, with intercalations of minor amount of mafic lavas and continental conglomerate (Montoya et al., 2019a). The lower ignimbrite succession is intruded by rhyolitic domes dated at ~29 Ma and bimodal dikes swarm (Ferrari et al., 2013; Montoya et al., 2019a).

The San Dimas district is affected by two main fault systems with E-W and NNW-SSE orientation. Both systems present various reactivation events and are mineralized (Horner and Enriquez, 1999; Enriquez et al., 2018; Montoya et al., 2019a). The E-W fault system affects mainly the LVC and is overprinted by the NNW-SSE one. The main NNW-SSE striking normal faults divide the district in tilted fault blocks, dipping

up to 30° to the east or to the west. Based on veins paragenesis sequence and $^{40}Ar/^{39}Ar$ ages, Montoya et al. (2019b) propose that mineralization occurs in two discrete hydrothermal events, a first Eocene Ag-dominant vein system (adularia + rhodochrosite type; ca. 41–40 Ma), mainly developed into E-W striking faults, followed by a Au-dominant epithermal vein mineralization (sericite type; ca. 30 Ma), which was emplaced into NNW-SSE striking faults concurrent with Oligocene rhyolitic domes related to the final stage of the first SMO ignimbrite flare up.

3. Previous fluid inclusions studies of the San Dimas Ag–Au district

Previous hydrothermal fluid studies at San Dimas mainly focused on the "bonanza" level Au-dominant structures of the Tayoltita Block (Fig. 2). Homogenization temperatures for quartz Au/Ag-mineralizing stage range from 250 °C to 310 °C, averaging 260 °C in all studies (Smith et al., 1982; Clarke and Title, 1988; Conrad et al., 1992; Enriquez and Rivera, 2001; Albinson et al., 2001; Churchill, 1980). Reported freezing point show a tide variation range from −0.11 °C to −1.5 °C. (Smith et al., 1982; Clarke and Title, 1988; Conrad et al., 1992; Enriquez and Rivera, 2001). Smith et al., (1982) report positive last solid fusion temperatures ranging from 0.3 °C to 2.9 °C, suggesting clathrate fusion and occurrence of CO_2. They also describe heterogeneous trapping and vapor and liquid phase homogenization processes, suggesting occurrence of boiling. Clark and Titley (1988), present a reverse correlation between Ag/Au ratio and FI salinity. FI data and field relationships indicate an approximate 400 to 1000 m depth range below the surface for the bonanza level at the time of vein formation (Smith et al., 1982; Clark and Titley, 1988). The $\delta^{18}O_{qtz}$ values of Au/Ag mineralizing quartz event range from 3.9 to 9.5‰. Recalculated $\delta^{18}O_{H2O}$ range from −2.9 to 3.7‰, indicating that meteoric water dominated the hydrothermal system (Smith et al., 1982; Conrad and Chamberlain, 1992). Gas spectrometry indicates that water constituted over 99.5 mol percent of the liquid and gas phases, with CO_2 comprising most of the remaining gases, minor CO and traces of H_2, CH_4, N_2, C_2H_6, H_2S, C_3H_8, SO_2 and NO (Smith et al., 1982).

4. Results

Analytical techniques and detailed data are presented in supplementary files.

4.1. Decriptometry

Fig. 3 presents the results of the decrepitation experiment of twenty quartz populations from nine Au- and Ag-dominant veins representative of the San Dimas district as well as its southern extension. All samples display a more or less defined bimodal distribution pattern. The two maximum peaks range from 200 to 220 °C and 400 to 440 °C (Fig. 3A). In a few samples a third high temperature peak roughly developed above 550 °C (Fig. 3A). Burlinson et al. (1983, Burlinson et al., 1988) suggest that peaks like these are not related to FI decrepitation but to quartz crystallization phase transition, therefore should not be considered. Quartz cements from the "Bonanza" level are characterized by higher FI decrepitation count per 10 s than samples collected at the top or at the root of the veins.

Plotting the 400 °C/200 °C peak intensity ratios versus Au/Ag ratio allows distinguishing both Ag- and Au-dominant hydrothermal events (Fig. 3B). The plot also shows a positive relationship between the 200 °C peak intensity with Ag concentration (Fig. 3B).

4.2. Vein and fluid inclusions petrography and microthermometry

The Ag- and Au-dominant veins paragenetic sequence is detailed in Montoya et al. (2019b) and presented in Fig. 4. Ag-dominant veins are characterized by three stages of formation named open, filling and close stage. The opening stage shows open space filling quartz texture. The filling stage corresponds to the mineralization and is characterized by mosaic quartz texture. The closing stage present crack-seal and open space filling quartz texture (Fig. 4).

Based on the petrographic and compositional features of the FI at room temperature, two types were identified: type I and type II. Type I is the dominant type recognized in both Ag- and Au-dominant events and corresponds to two phases liquid–vapor (LVaq), liquid dominant inclusions, with estimated vapor volume of 5 to 10%. Type I primary FI (LVaq) are either found as isolated inclusions, in small clusters, or in quartz growing plans. This population of FI yields very homogeneous volume ratios (Fig. 4 A,B, C). Typically, the FI are negative crystals to ovoid in shape and are less than 20 μm in length. Type II is recognized principally in the filling stage of the Ag-dominant event and corresponds to two-phases vapor dominant (VLaq) inclusions, with estimated vapor volume up to 90% (Fig. 4 D, E, E). Type II FI (VLaq) are crystal negative to ovoid in shape and are less than 30 μm in length. The visual estimate of the liquid-to-vapor ratio is highly variable. These FI are only found in small clusters.

The opening stage presents the highest homogenization temperature. The type I fluid inclusion homogenize to liquid between 128 °C and 320 °C, with a poorly defined modal distribution (median at ca. 240 °C; Fig. 5 A, B; table 1). Final ice melting temperatures occurs between −0.9 °C and 0.3 °C, corresponding to 0 and 1.57 wt% NaCl eq (Fig. 5 C).

The filling stage presents two biphasic fluid inclusions types, liquid dominant (LVaq) and vapor dominant (VLaq). Final homogenization temperatures range from 122 °C to 304 °C with a well-defined unimodal distribution and a median value at ca. 140 °C (Fig. 5A, B). Final solid melting temperatures present a wider distribution, including ice and clathrate melting at temperatures varying from −0.5 °C to 5.6 °C, corresponding to 0 and 0.88 wt% NaCl eq (Fig. 5C).

In the closing stage, type II (LVaq) fluid inclusions homogenize to liquid from 120 °C to 318 °C with a bimodal statistical distribution, with maximum values at 140 °C and 230 °C. Final ice melting temperatures are almost constant, varying between −1.9 °C and 0.0 °C corresponding to 0 and 3.22 wt% NaCl eq (Fig. 5C).

In the Au-dominant veins, the biphasic LVaq FI in the quartz stage yield final ice melting temperatures ranging from −1.4 °C to −0.0 °C, corresponding 0 and 2.4 wt% NaCl eq. Total homogenization occurs in the liquid phases at temperatures ranging from 121 °C to 316 °C in a bimodal distribution (Fig. 5B, D and Table 1).

On a diagram of last melting temperature (Tm) versus homogenization temperature (Th) (Fig. 5C, D), the Ag- and Au-dominant FI from San Dimas district veins swarm overlap historic data trend compilations (Smith, 1982; Conrad et al., 1992; Enriquez and Rivera, 2001). Both Ag- and Au-dominant events record the same evolution from high to low homogenization temperatures with low salinity values, suggesting an adiabatic cooling process in a dominant meteoric environment (Fig. 5C, D). The Ag-dominant filling stage presents low homogenization and positive fusion temperatures indicating clathrate fusion and the presence of dissolved CO_2.

Micro-infrared spectrometry analysis was performed to show the CO_2 concentration in the different events/stages of Au/Ag mineralization. In all Ag- and Au-dominant events analyzed samples, CO_2 concentration in FI vapor phase remain within the analytical noise, including in LVaq vapor dominant inclusions. However, CO_2 concentration was detected in water liquid phase in analyzed fluid inclusions from both mineralization events. CO_2 concentration increases notably in the Ag-dominant filling stage event.

4.3. Fluid inclusions $\delta^{18}O$ and δD isotope analysis

$\delta^{18}O$ and δD isotopic data are presented in Table 2 and Fig. 6 in ‰ deviation relative to the SMOW standard. Data are grouped according to mineralized stages from the older to the more recent. From Victoria

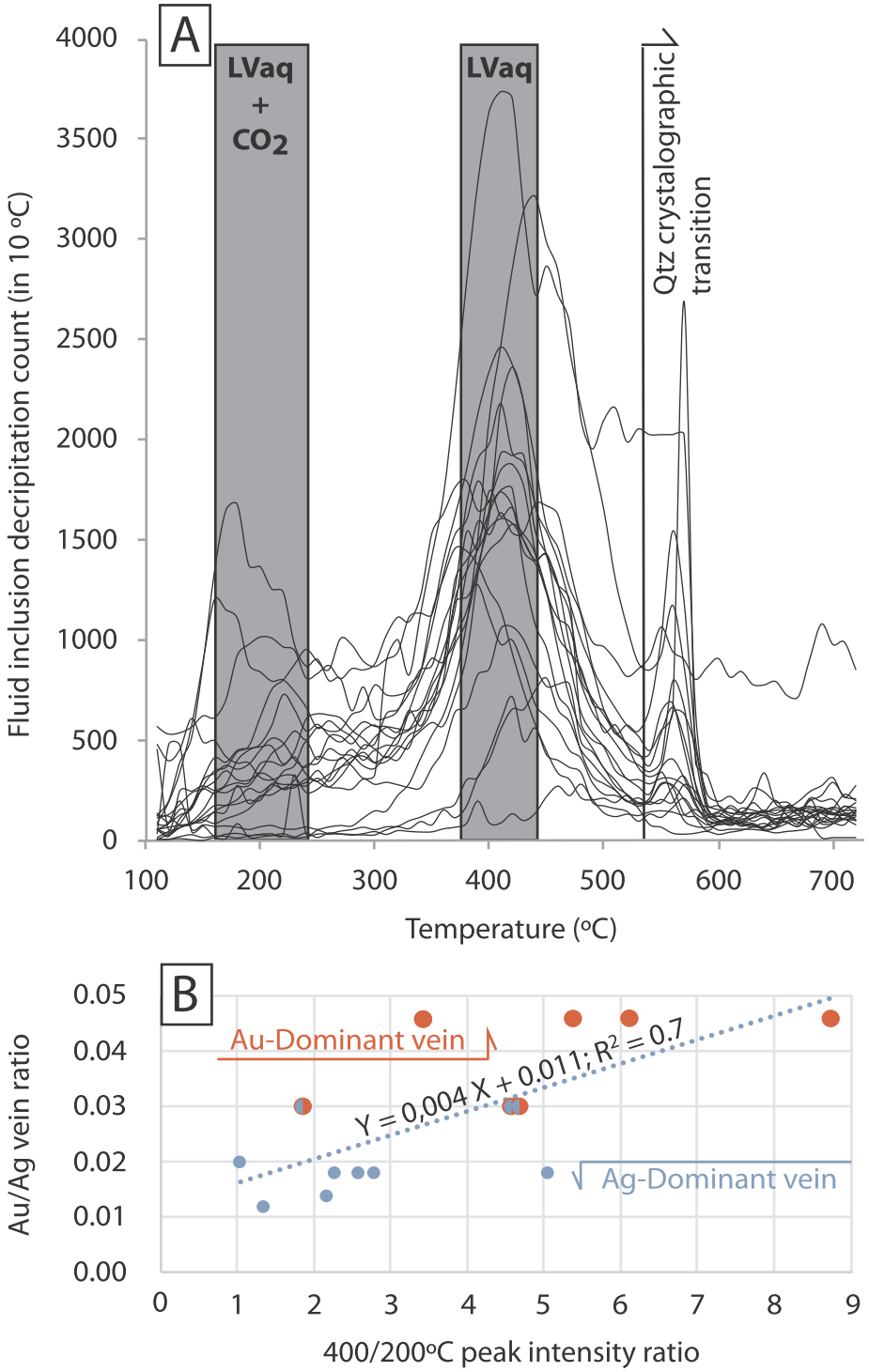

Fig. 3. (A) FI decrepitation diagram of Ag-dominant and Au-dominant quartz veins from Ag/Au San Dimas district. (B) 400/200 °C peak intensity ratio versus Au/Ag metals ratio sample diagram of Ag-dominant and Au-dominant quartz veins from the Ag/Au San Dimas district.

and Robertas Eocene Ag-dominant veins, we analyze six FI populations from opening (n = 1), filling (n = 4) and closing (n = 1) quartz cement stages. The analyzed δD values display a narrow range from −87.98‰ to −63.02‰ whereas the measured $\delta^{18}O$ values display a relatively large range, from −8.79‰ to 10.34‰ (Table 2). $\delta^{18}O$-δD fluid inclusions isotopic signature of Robertas quartz filling stage was detailed following its thermal decrepitation pattern (Fig. 6). Fluid inclusions population in the range 110 °C − 310 °C shows $\delta^{18}O$-δD isotopic signature of 10.34‰ and −87.98‰, whereas that in the 310 °C to 550 °C range has $\delta^{18}O$-δD signature of −0.54‰ and −88‰. Once plotted in the $\delta^{18}O$-δD diagram the results are distributed along a mixing line from the global meteoric water line (GMWL) to the primary magmatic water field. The opening and closing stages results plot closer to the GMWL than the filling (mineralizing) stage, which plot toward or within the Mexican active geothermal fields and epithermal deposits fields.

Four samples from four different Au-dominant veins were analyzed (Arana vein, Causita vein, San Luis vein and San Antonio vein; Fig. 6; table 2). The $\delta^{18}O$-δD values range from −5.13‰ to 1.61‰ and from −72.20‰ to −45.81‰. In the $\delta^{18}O$-δD diagram the results obtained

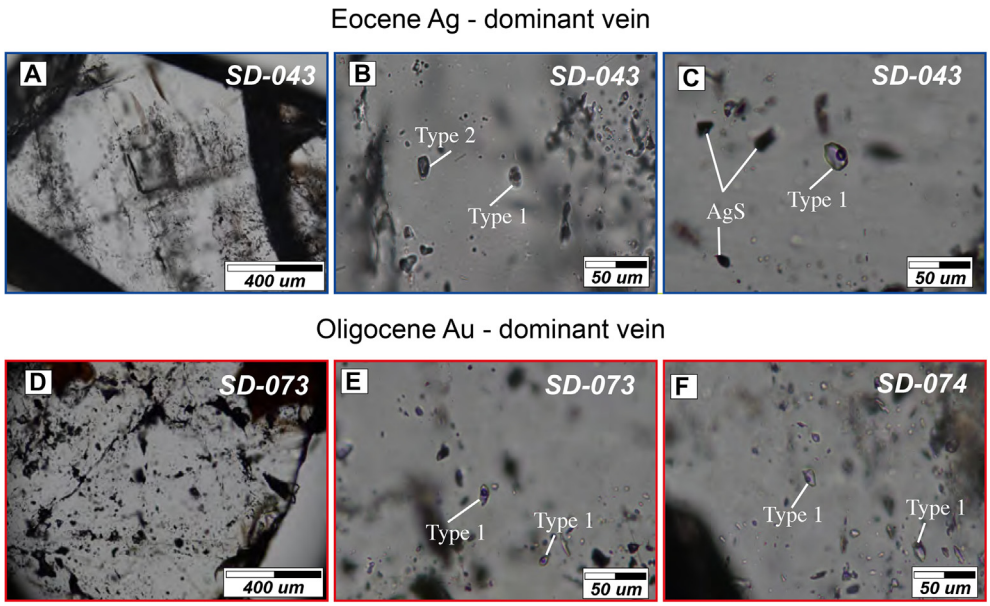

Fig. 4. Photomicrographs image of fluid inclusions paragenesis. (A) Filling quartz stage (mineralization stage) from Roberta vein with primary FI trails along growing quartz plans; (B) Type 1 and type 2 association; Type 2-Primary biphasic Liquid-dominant FI; Type 2-Primary biphasic gas-dominant FI; (C) Type 1-Primary biphasic Liquid-dominant FI associate with silver droplets; (D); Sulphide mineralizing quartz from San Antonio vein with primary biphasic Liquid-dominant FI clouds; (E) Type 1-Primary biphasic Liquid-dominant FI; (F) Type 1-Primary biphasic Liquid-dominant FI.

from Arana, Causita, San Luis and San Antonio Au-dominant veins overlap the Ag-dominant mineralized filling stage isotopic trend data and plot between the LS and IS Mexican epithermal deposit and active geothermal fields.

4.4. Chemistry and noble gas isotope composition of fluid inclusions

4.4.1. Chemistry

For the Eocene Ag-dominant veins we analyzed quartz samples from

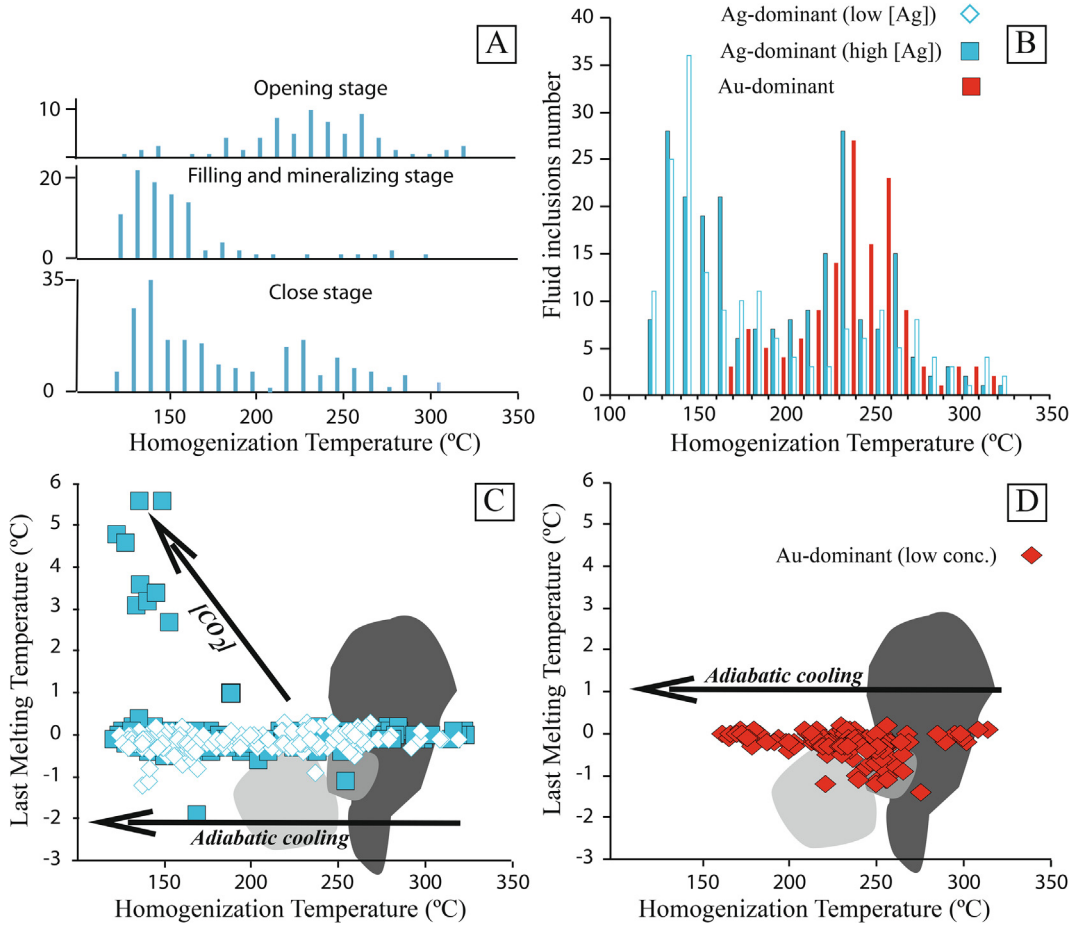

Fig. 5. (A) Homogenization temperature histograms for FI from Ag-dominant opening, filling and close stages. (B) Homogenization temperature histograms for FI from Ag-dominant and Au-dominant quartz events. (C) Homogenization temperature and ice melting temperature plot for Ag-dominant quartz gangue. (D) Homogenization temperature and ice melting temperature plot for Au-dominant quartz gangue. Dark grey area: FI from Smith et al., (1982); grey area: FI from Clark and Titley (1988); light grey area: FI from Enriquez and Rivera (2001a).

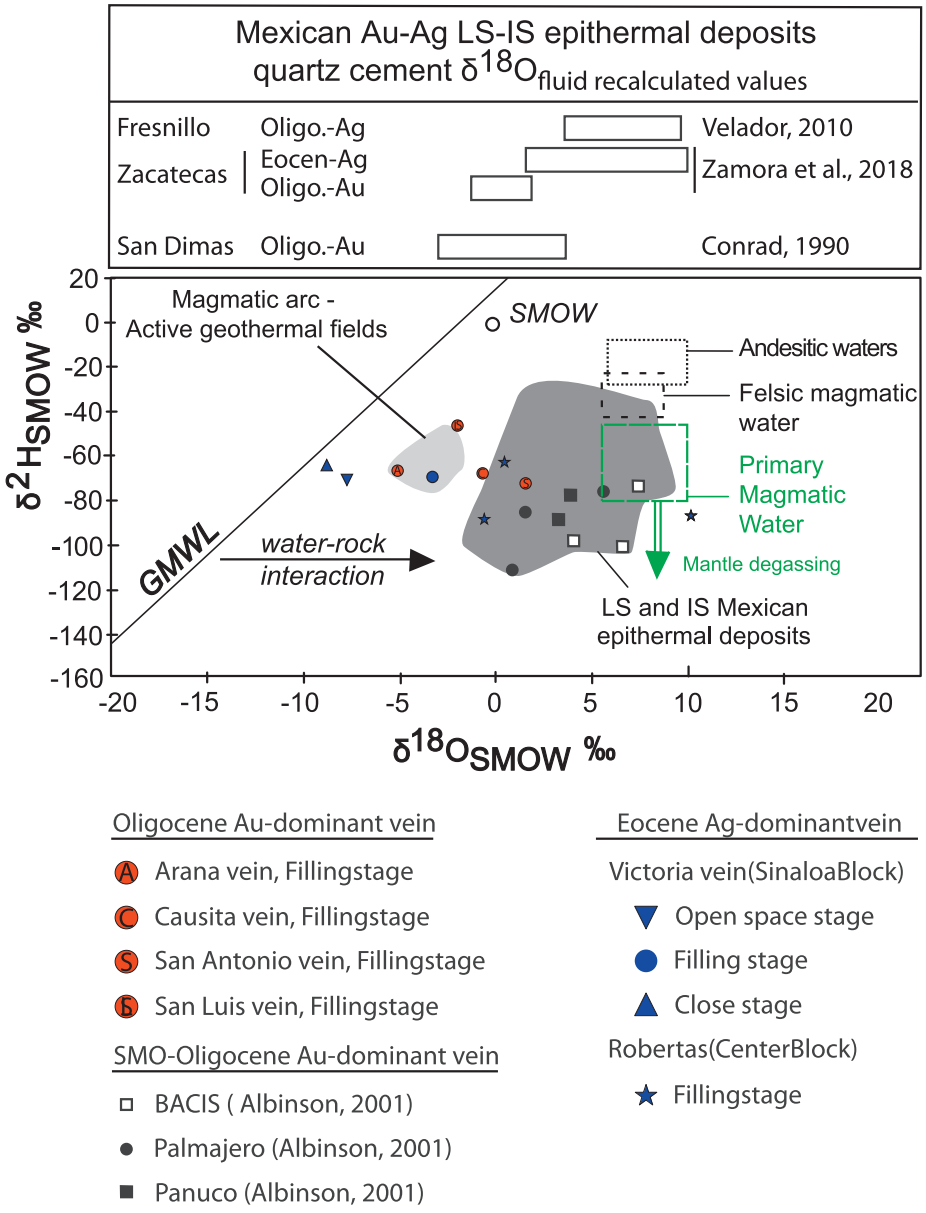

Fig. 6. $\delta^{18}O$-δD diagram of the Eocene Ag-dominant and Oligocene Au-dominant mineralized veins from the San Dimas Au/Ag district. The epithermal deposit field is drawn from Albinson et al. (2001), Camprubi. (2013), Velador, (2010); Simmons et al. (1986); and Zamora Vega et al. (2018). Primary magmatic water, felsic water and Andesitic water fields are taken from Sheppard et al., (1969), Taylor, (1974), Sheppard, (1986), and Giggenbach, (1992a and 1992b). Mexican active geothermal sites: Los Azufres and Los Humeros related to magmatic arc are taken from Pinti et al. (2013) and references therein.

the open-filling and closing stages of the Victoria vein and for the filling stage of the Roberta vein. Quartz samples for the Oligocene Au-dominant vein come from the filling stage of the Arana, San Antonio, San Luis, Causitas and Mala Noche veins (Figs. 7 and 8). The chemistry of FI and noble gases isotopic ratio is given in Table 3. Measurement uncertainties for some samples are relatively high because the amount of gas extracted from these samples was small.

H_2O is the dominant species of FI and varies between $3.6{\cdot}10^{-6}$ and $3.0{\cdot}10^{-5}$ mol g^{-1} (average $1.4{\cdot}10^{-5}$ mol g^{-1}) in the Eocene Ag-dominant vein, and between $4.4{\cdot}10^{-6}$ and $2.5{\cdot}10^{-5}$ mol g^{-1} (average $1.3{\cdot}10^{-5}$ mol g^{-1}) in the Oligocene Au-dominant vein. CO_2 and N_2 are the other major components of FI. CO_2 ranges between $7.1{\cdot}10^{-9}$ and $2.5{\cdot}10^{-8}$ mol g^{-1} (average $1.6{\cdot}10^{-8}$ mol g^{-1}) in the Eocene Ag-dominant vein, and between $8.2{\cdot}10^{-9}$ and $1.8{\cdot}10^{-7}$ mol g^{-1} (average $4.8{\cdot}10^{-8}$ mol g^{-1}) in the Oligocene Au-dominant vein. N_2 varies in a narrow range between $3.1{\cdot}10^{-8}$ and $4.1{\cdot}10^{-8}$ mol g^{-1} (average $3.7{\cdot}10^{-8}$ mol g^{-1}) in the Eocene Ag-dominant vein, while between $1.6{\cdot}10^{-8}$ and $7.1{\cdot}10^{-8}$ mol g^{-1} (average $3.7{\cdot}10^{-8}$ mol g^{-1}) in the Oligocene Au-dominant vein (Fig. 7; Table 3).

Helium varies from $8.7{\cdot}10^{-14}$ to $9.2{\cdot}10^{-13}$ mol g^{-1} (average $3.0{\cdot}10^{-13}$ mol g^{-1}) in the Eocene Ag-dominant vein, while between $3.3{\cdot}10^{-14}$ and $8.1{\cdot}10^{-13}$ mol g^{-1} (average $2.8{\cdot}10^{-13}$ mol g^{-1}) in the Oligocene Au-dominant vein. Helium corrected for atmospheric contamination ($^4He_{corr}$) shows comparable range of values (mean values within 10%), except for the most air contaminated samples. ^{20}Ne varies from $4.4{\cdot}10^{-14}$ to $7.6{\cdot}10^{-14}$ mol g^{-1} (average $5.6{\cdot}10^{-14}$ mol g^{-1}) in the Eocene Ag-dominant vein, while between $3.7{\cdot}10^{-14}$ and $1.1{\cdot}10^{-13}$ mol g^{-1} (average $6.8{\cdot}10^{-14}$ mol g^{-1}) in the Oligocene Au-dominant vein. ^{40}Ar varies in a narrow range from $1.8{\cdot}10^{-11}$ to $2.6{\cdot}10^{-11}$ mol g^{-1} (average $2.1{\cdot}10^{-11}$ mol g^{-1}) in the Eocene Ag-dominant vein, while between $1.3{\cdot}10^{-11}$ and $3.5{\cdot}10^{-11}$ mol g^{-1} (average $2.2{\cdot}10^{-11}$ mol g^{-1}) in the Oligocene Au-dominant vein.

In terms of chemistry, we do not notice appreciable differences between the Eocene Ag- and the Oligocene Au-dominant veins, with a

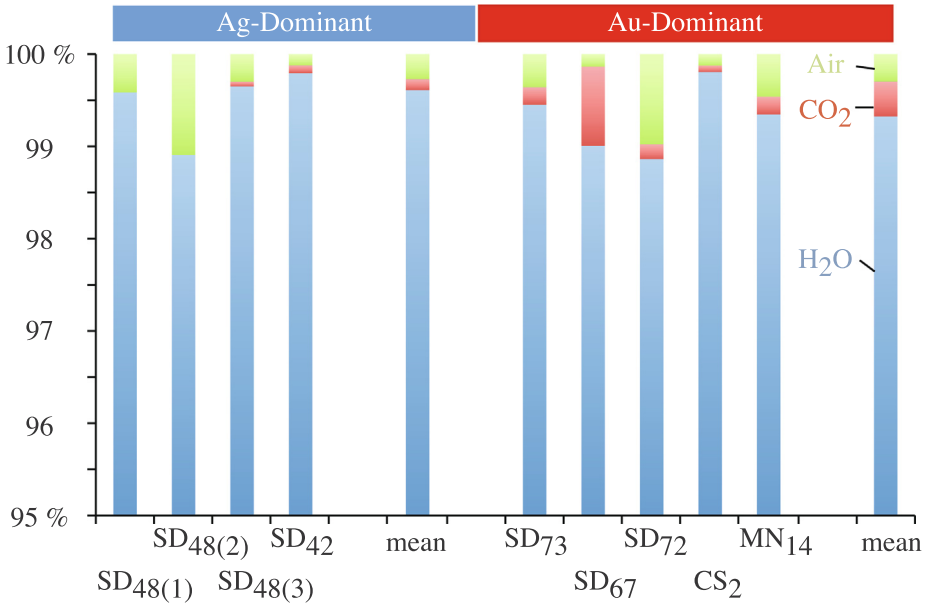

Fig. 7. Major and noble gases Eocene and Oligocene fluid inclusions composition.

general overlap between the two groups of samples.

4.4.2. Noble gas isotope composition

The Eocene and Oligocene quartz $^{4}He/^{20}Ne$ ratios vary from 1.2 to 20.7 and from 0.4 to 11.7, respectively, indicating a strong contribution from an atmospheric-derived component (Ozima and Podosek, 2002). $^{40}Ar/^{36}Ar$ ratios vary from 295.13 to 304.04 (average 298.99) and from 294.04 to 319.71 (average 300.66), respectively, supporting the indications from $^{4}He/^{20}Ne$ (Ozima and Podosek, 2002). $^{20}Ne/^{22}Ne$ and $^{21}Ne/^{22}Ne$ ratios from Eocene and Oligocene quartz give similar indications: 9.79 to 9.81 and 0.0285 to 0.0291, respectively. Fig. 8A is a plot of $^{21}Ne/^{22}Ne$ versus $^{20}Ne/^{22}Ne$ showing trajectories for radiogenic and nucleogenic Ne production extending outward from the air value. Within the error margin all samples plot near the air value. Some Oligocene Au-dominant results plot slightly below it, suggesting a small influence of degassing processes consistent with a hydrothermal component in the gas (Ballentine, 1997, and references therein). Fig. 8B plots Argon (mol/g) versus neon (mol/g) showing air and air saturated water line distribution (Ozima and Podosek, 2002). Within the error margin all samples plot near the air-line.

The $^{3}He/^{4}He$ ratios not corrected for atmospheric contamination (R/Ra) from Eocene Ag-dominant (0.08–0.24 Ra, mean 0.19 Ra) are on average lower than for the Oligocene Au-dominant (0.07–1.19 Ra, mean 0.57 Ra), with a partial overlapping of values from both deposits (Fig. 8C). He corrected for air contamination ($^{4}He_{corr}$) versus Rc/Ra plot (Fig. 8C) shows that overall the two events are in partial overlapping. Au-dominant Oligocene samples are well distributed along a crust-magmatic mixing line, pointing out the predominance of crustal fluids and variable contributions of a "hypothetical local magmatic" reservoir at about 3 Ra. Ag-dominant Eocene samples present a lateral shift, suggesting a dominant presence of crustal fluids. In the $^{4}He/^{40}Ar$ versus R/Ra plot (Fig. 8D) we get similar information, confirming our previous inference of air-crust mixing for most of the samples, except Causita, San Antonio, and Arana samples from Oligocene Au-dominant veins suggesting He_{mantle} contribution in a 3-component mixing. Considering $^{3}He/^{4}He$ ratio values of 0.01–0.05 Ra for the crust and 8 Ra for a MORB-like mantle ($R/Ra = 8 \pm 1$; Graham, 2002), the He_{mantle} contribution is estimated to be up to 1.7% and 24% in the Ag- and Au-dominant veins samples, respectively.

Accordingly, the $^{3}He/^{4}He$ ratios corrected for atmospheric contamination (Rc/Ra) from Eocene Ag-dominant samples (0.07–0.13 Ra, mean 0.10 Ra) is lower than for the Oligocene Au-dominant samples (0.05–1.91 Ra, mean 0.81 Ra), with a partial overlapping of values from both deposits.

5. Discussion

5.1. Sources and evolution of Eocene Ag- and Oligocene Au-dominant ore-forming fluids

The origin of the ore-forming fluids cannot effectively constrain the source of the ore-forming metals. However, they illustrate well the dynamic of the hydrothermal system, metals transport and precipitation conditions. Petrographic examination of FI assemblages provides evidence concerning the chemical and physical conditions of formation of hydrothermal deposits (Bodnar et al., 1985). Two FI assemblages and compositional features were identified in both the Eocene and Oligocene hydrothermal structures: 1) Type I, two phase liquid–vapor (LVaq), liquid dominant, with estimated vapor volume percent of 5 to 10, is the main dominant type recognized in both events; 2) Type II, two-phase vapor dominant (VLaq), with estimated vapor volume percent up to 90, is recognized principally in the filling stage of the Ag-dominant event in the highest Ag grade mineralized area. The presence of vapor-dominated inclusions, the heterogeneous liquid/vapor ratios and the hockey stick shape distributions in the Th vs Tm diagram suggest that boiling was an important process during silver precipitation. The chemistry of FI confirms that H_2O is the major component. In addition, the lack of clear differences in salinity between the Eocene and Oligocene hydrothermal events confirms that Type I FI dominates within the two events and that Type II FI poorly or not contributed to the extracted gas mixture (Fig. 7).

Fluid inclusions microthermometry and FTIR spectroscopy indicate that ore-forming fluid belongs to the H_2O-NaCl-(CO_2) system and has high to low temperature (ca. 320–120 °C) and low salinity. Eocene and Oligocene hydrothermal events homogenization temperature and salinity data are comparable to those described in the literature (Smith, 1982; Conrad et al., 1992; Enriquez and Rivera, 2001). The overlapping of their homogenization temperature ranges prevents using the microthermometry technique to discriminate both events. However, the Eocene Ag-dominant hydrothermal event is characterized by positive ice melting temperature. The low salinity of the solutions, the small amounts of dissolved CO_2 content, and the absence of trapped minerals

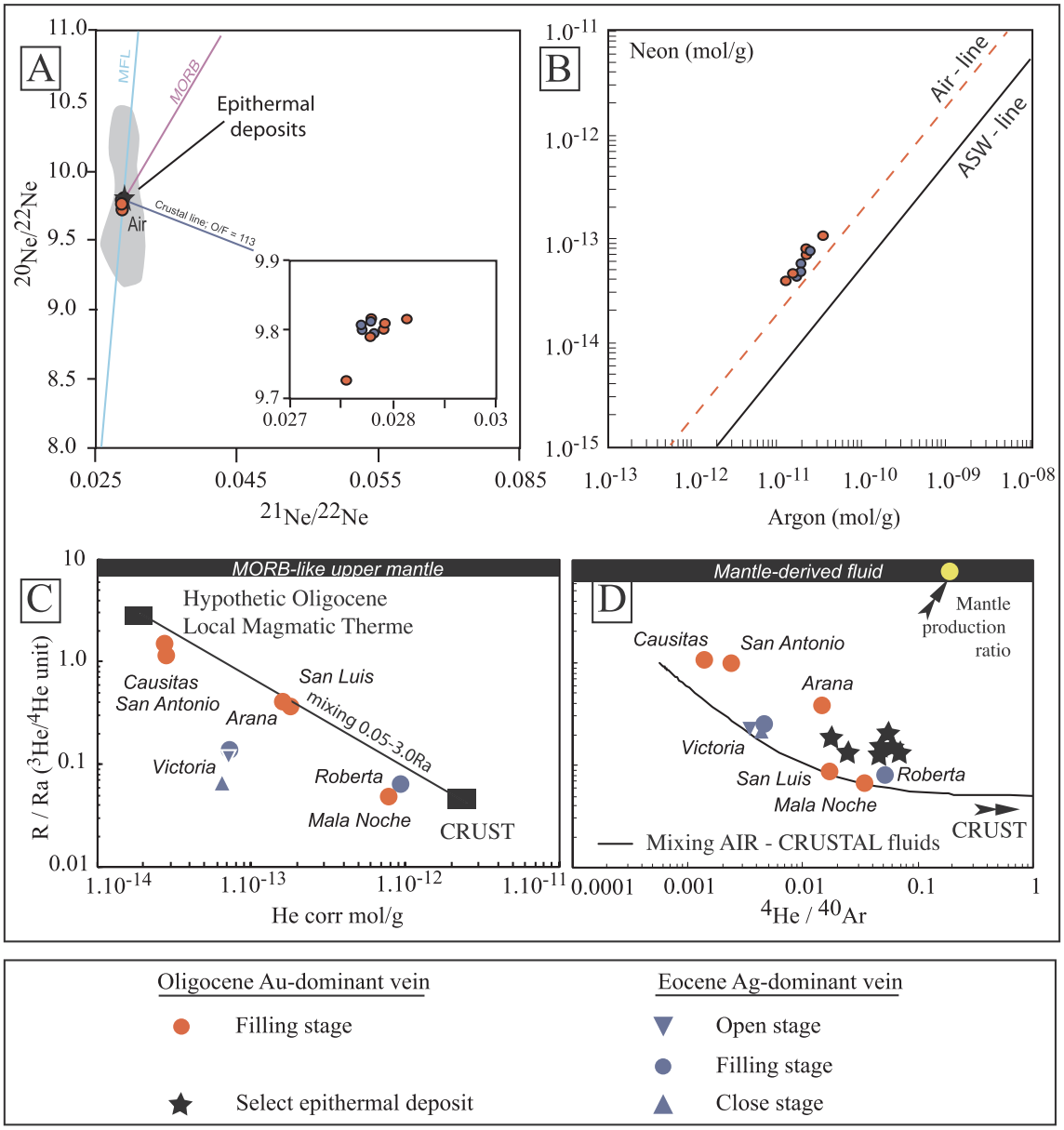

Fig. 8. Noble gases and helium isotope geochemistry diagrams. (A) $^{20}Ne/^{22}Ne$ vs. $^{21}Ne/^{22}Ne$ plot of the Eocene and Oligocene fluid inclusions. The MORB line represents mixing between atmospheric neon and that measured in the upper mantle (Sarda et al., 1988). The crust line represents the evolution of neon isotopic composition by nucleogenic production of ^{20}Ne, ^{21}Ne, $^{22}Ne^*$ in a crustal source having constant O/F ratio of 113 (Kennedy et al., 1990). MFL is the mass fractionation line depicting the isotopic variations of Ne produced by a diffusion-controlled degassing process. (B) Plot of Argon (mol/g) versus Neon (mol/g) including the air- and ASW-line distribution. (C) Plot of R/Ra versus $^{4}He/^{20}Ne$, with mixing trend fitting the data. (D) Plot of R/Ra versus $^{4}He/^{40}Ar$, with air and crustal fluid mixing trend. The assumed mantle and crustal production ratios are taken from Marty (2012) and Ballentine et al. (1994, 2002), respectively. Black stars are compiled data from worldwide mesothermal granite related deposits (references in table).

(halite, sylvite) suggest that the main component is meteoric water. These evidences are corroborated by the chemistry of FI, which clearly indicates H_2O as the major component and significantly low to absent CO_2 content (Fig. 7). In the Eocene and Oligocene hydrothermal events, the FI microthermometric results reveal a continuous adiabatic cooling of the fluid and an increase of CO_2 content during the Ag-dominant filling stage.

$\delta^{18}O$-δD are considered to provide precise information about the sources and evolution of ore-forming fluids (Taylor, 1974). Plotted in the $\delta^{18}O$-δD diagram, both Eocene and Oligocene mineralizing FI are distributed along a mixing line from the global meteoric water line (GMWL) to the primary magmatic water field (Fig. 6). During the Eocene Ag-dominant hydrothermal system, the opening and closing stages data are close to the GMWL, showing the dominance of meteoric fluids, whereas the filling (mineralizing) stage results plot in or near the Mexican active geothermal fields. The $\delta^{18}O$ shift to less negative values of these samples suggests a magmatic input in the mixing fluids isotopic equation. The $\delta^{18}O$-δD data of the Au-dominant hydrothermal events are similar to those of numerous SMO and Mexican LS and IS epithermal deposits (Fig. 6). The $\delta^{18}O$-δD data of the Au-dominant hydrothermal event show a range of compositions indicating that ore fluids are partially magmatic-derived. The obtained $\delta^{18}O$ values suggest mixing and the involvement of meteoric water into the ore fluid, which could lead to the lower $\delta^{18}O$ values. This is also consistent with the measured low homogenization temperatures and salinities of fluids in the Au-dominant event.

The He-Ar-Ne abundance and isotope ratios are a powerful tool in discriminating meteoric, magmatic and crustal reservoirs of the

different fluids (Ballentine, 1997; Ozima and Podosek, 2002). Ar and Ne isotopic data as well as $^4He/^{20}Ne$ and $^4He/^{40}Ar$ ratios indicate that Ar and Ne in both Eocene and Oligocene FI samples are mainly atmospheric (table 3; Fig. 8C and 8D), with very minor nucleogenic production from halogens (F) and crustal contamination (K). The conservative behavior of helium and the difference in isotopic composition between the crust ($^3He/^4He$ = 0.01–0.05 Ra; Ballentine et al., 2002), MORB-like mantle ($^3He/^4He$ = 8 ± 1 Ra; Sarda et al., 1988; Ballentine et al., 2002) and atmosphere ($^3He/^4He$ = 1 Ra; Ballentine et al., 2002) make helium the most sensitive proxy for the determination of the sources of the fluids trapped during mineralization and allow to illustrate possible interactions between these fluids and the country rocks (e.g., Mamyrin and Tolstikyn, 2013). Since Simmons et al. (1986), it is accepted that hydrothermal minerals can preserve mantle-derived ^3He. However, there are evidences that in FI-free quartz crystals He may diffuse from the crystal lattice, especially at progressively higher temperatures (e.g., next to or above 400 °C; Shuster and Farley, 2005). On the other hand, the diffusivity through quartz lattice of ^4He seems indistinguishable from that of ^3He, providing no graphical evidence for the commonly expected inverse square root of the mass diffusion relationship between isotopes. This implies that even in case of a diffusive loss of helium, the $^3He/^4He$ should maintain the original signature. Another indication in support of the conservative behavior of He within FI of quartz crystals of hydrothermal origin comes from the evidence that FI may enhance noble gas retentivity in quartz crystals (Shuster and Farley, 2005). In Fig. 8, our data do not show any graphical evidence of He loss as well as $^3He/^4He$ fractionation (even considering ^3He vs R/Ra; Table 3), suggesting that they can be used to constrain the origin of fluids trapped in Ag- and Au-dominant deposits. We notice that the lowest $^3He/^4He$ are recorded in the most He-rich samples, although there is not a unique trend of decrease of $^3He/^4He$ at increasing $^4He_{corr}$ concentration. This behavior strongly indicates mixing between crustal and magmatic fluids, rather than ingrowths of ^4He from the radiogenic decay of U and Th.

The $^3He/^4He$ not corrected for air contamination from San Dimas Eocene Ag-dominant and Oligocene Au-dominant FI present values spanning a wide range (0.07–1.19 Ra), which is in partial overlapping among a few samples from the two distinct deposits. When $^3He/^4He$ is plotted versus $^4He/^{20}Ne$ and $^4He/^{40}Ar$ (Fig. 8D, respectively), we deduce that air-saturated groundwater is the main isotopic reservoir. However, there are clear evidences that fluids from both hydrothermal events mix with fluids from other sources (i.e., crustal and magmatic fluids). In particular, FI trapped in the Eocene Ag-dominant hydrothermal deposits originate from a mixing mostly involving atmospheric and crustal fluids, with a slight contribution of mantle or magmatic ^3He (Fig. 8C and 8D). This could imply that during the Eocene Ag-dominant hydrothermal event faults pathways only marginally reached the basement or magmatic reservoir. Instead, FI trapped in part of the Oligocene Au-dominant hydrothermal deposits track a 3-components mixing that involve atmospheric, crustal, and mantle fluids (Fig. 8C and 8D). In fact, during the Oligocene Au-dominant hydrothermal event continental extension had already produced a thinner crust and involved a deeper faults system (Ferrari et al., 2017; Montoya et al., 2019a, 2019b), creating effective pathways for the mantle derived gases (up to 24%, Table 3) to escape and be subsequently trapped in the mineralized veins. This evidence is also supported by the $\delta^{18}O$-δD values of the Au-dominant hydrothermal event, which indicate that ore fluids are partially magmatic-derived.

In order to figure out what could be the source of ^3He excess in Causita, San Antonio, and Arana samples from Oligocene Au-dominant veins, we plot $^4He_{corr}$ concentration versus Rc/Ra (Fig. 8C), excluding in this way any effect due to atmospheric contamination. If we consider a possible crustal term having $^3He/^4He$ = 0.05 Ra and $^4He_{corr}$ $\sim 2{\cdot}10^{-12}$ mol g^{-1}, we could fit Causita, San Antonio, and Arana samples assuming a binary mixing with a possible local magmatic term having $^3He/^4He \sim 3$ Ra and $^4He_{corr} \sim 2{\cdot}10^{-14}$ mol g^{-1}. This term could correspond to a differentiated magmatic source that resided and degassed within the crust at the time of formation of quartz and that under cooling and ageing conditions lowered its original MORB-like $^3He/^4He$ values (Ballentine et al., 2002; Batista Cruz et al., 2019). This hypothesis has not strong constraints, so we cannot exclude that a magmatic body with higher $^3He/^4He$ and lower ^4He concentration could have supplied fluids trapped in quartz samples. We are only proposing an alternative explanation to the direct rise of ^3He-rich fluids from the local mantle.

Compared to other studies, the range of $^3He/^4He$ values measured in San Dimas Eocene and Oligocene hydrothermal events is significantly lower than those of epithermal deposits and magmatic arc environments ($^3He/^4He$: 0.1–10; Manning and Hosftra, 2017). In the specific case of the Oligocene Au dominant LS-epithermal event, the most comparable with similar deposits, the low $^3He/^4He$ ratios values could be explained by several reasons: (1) analyzed samples do not represent the highest Au grade areas, (2) quartz could present post-entrapment He ingrowth or exchange with external fluids rich in radiogenic ^4He (Kendrick and Burnard, 2011), and (3) despite our attempt to remove secondary inclusions a variable proportion of secondary inclusions probably contributed to enrich FI in the crustal component, saturating the isotopic ratio end member.

In hydrothermal systems, gold and silver transport and deposition depend on fluid composition, temperature, pressure, pH, oxygen and sulphur fugacity, and type and amount of dissolved sulphur and other species (e.g. Mikucki, 1998). The low salinity, low to intermediate sulphidation and near-neutral pH environments and occurrences of several sulphides and sulphosalts, gold–silver from both hydrothermal mineralizing fluids (Tmi = −1.9 to 5.6 °C) pleads in favor of silver and gold transport as $AgHS^-$ and $Au(HS)_2$ complex (Zotov et al.,1995; Barnes, 1997; Cooke and Simmons, 2000; Stefansson and Seward, 2003, 2004; Pokrovski et al., 2014). The stability of $Au(HS)_2$ complexes is greatly increased by the presence of low concentrations of chlorine (Zajacz et al., 2010). Near neutral to slightly alkaline solutions originating in the field of maximum gold solubility as a bisulphide complex produced sericite as the most common potassium aluminosilicate in the alteration assemblages (Romberger, 1986). In the San Dimas district, the Au-dominant vein and telescoped structures are characterized by a well-defined sericite alteration halo, while Eocene Ag-dominant hydrothermal structures are characterized by quartz-adularia-rhodochrosite gangue and chlorite alteration halo (Montoya et al., 2019b). Solubility of $AgHS^-$ and $Au(HS)_2$ is extremely sensitive to changes in temperature and pressure. Depressurization (which occurs during hydraulic fracturing, boiling or as hot fluids ascend up faults) and/or rapid cooling (50 °C or more) decrease Au-Ag solubility by 90% (Zhu et al., 2011). The adiabatic decrease in homogenization temperature recorded in both events and the boiling process observed in Eocene and Oligocene events provided favorable conditions for the deposition of precious metals deposition.

In absence of external geothermometer, pressure and temperature (P-T) trapping conditions could not be estimated for both mineralizing hydrothermal events. However, the chronology of the magmatism and hydrothermal events give us some key information to estimate mineralization depth formation within a reliable geological evolution scenario. The space–time association of Oligocene rhyolitic magmatism with the Au mineralized veins, as well as the chemical and isotopic evidences for a meteoric fluids source (Montoya et al., 2019b), clearly indicate a connection to an air saturated groundwater under hydrostatic P-T conditions. The sericite alteration halos of Au-dominant veins are observed in the stratigraphic column up to the Las Palmas sedimentary formation and are sealed by the Oligocene ignimbrite flows, suggesting that the mineralization structure almost reach the paleosurface, and probably developed within 1 km depth.

The synchronism of Eocene porphyric dikes and Ag mineralized veins, and the chemical evidences for a meteoric fluids source indicate a connection to an air saturated groundwater and degassing process

under hydrostatic P-T conditions, apparently in a shallow position.

However, several authors report that fluids exist at deeper depth in magmatic arcs context (down to 10 km, Menzies et al., 2014 among other). Reliable mineral (chlorite) or isotopic equilibrium geothermometers are needed to correct the minimum fluid inclusion homogenization determination (up to 20 bars). In our case, the alteration induced by the later Oligocene hydrothermal event does not allow to obtain reliable data, but the local geological evolution is well constrained and give us some reliable information. The Piaxla batholith mineral texture and its stratigraphic position, locally overlain by the Camichin sedimentary formation or by the Oligocene ignimbrite flows (~30 Ma, Montoya et al., 2019a), highlight an important extensional tectonic context since the Eocene. Continental conglomerates of Eocene to Oligocene age are widespread in all Central Mexico (Montoya et al., 2019a; Nieto-Samaniego, et al., 2019). At regional scale, the extensional tectonic and exhumation-erosion rate has been estimated at ca. ~0.3 mm/yr (Nieto-Samaniego, et al., 2019), in well agreement with the value for magmatic arc environments (Burkan et al., 2002). Taking into account these observations the difference in the maximum depth formation needed to overlap the Eocene and the Oligocene "bonanza" levels could be estimated at 2–3 km. Such conditions are in agreement to those reported in literature for comparable plutonic related vein deposits (Prokofiev and Pek, 2015; Nieva et al., 2019). At this depth, the silver mineralization trapping temperature, corrected for the hydrostatic pressure, could be estimated at ~350 °C (Steele-MacInnis et al., 2012).

5.2. A new genetic model for the San Dimas district

The San Dimas Ag–Au district is an example of a Eocene-Oligocene telescoped deposit that comprises two mineralizing events: (a) an Eocene Ag-dominant epithermal event (40–41 Ma; Montoya et al., 2019b) associated with the late stage intrusion of a batholith dated at 45–43 Ma (Henry et al., 2003; Montoya et al., 2019a); (b) an Oligocene Au-dominant low sulfidation epithermal event (ca. 30 Ma), associated with rhyolitic volcanism dated at 31–29 Ma (Montoya et al., 2019b). Zircon chemistry also illustrates the most likely magmatic sources for the hydrothermal pulses and thus brackets the age of the mineralization events (Montoya et al., 2019b).

The integration of microthermometry and noble gases, oxygen and deuterium isotope data, in conjunction with a detailed geological re-evaluation and tectonic and petrographic studies, permit a coherent genetic model to be drafted. This model is summarized in Fig. 9.

Eocene silver bearing veins are hosted in the Cretaceous to Paleocene Laramide arc volcanic sequence (Lower Volcanic Complex). Ag-dominant mineralization structures are mainly hosted in E-W sigmoidal gashes and geographically distributed in proximity with the Eocene Piaxtla batholith (Montoya et al., 2019a). The Ag-dominant veins are composed of different quartz and breccia events and are characterized by adularia and rhodochrosite gangue. The proximity of the epithermal alteration $^{40}Ar/^{39}Ar$ cooling ages (41–40 Ma) and the U/Pb zircon ages of the Piaxla batholith last magmatic pulses (45–43 Ma) support a genetic relationship (Montoya et al., 2019a, b). The continuous enrichment of the Eu/Eu* and (Ce/Nd)/Y) ratios through time, from 50 to 43 Ma in zircon crystals, strongly suggest that the most enriched magmatism occurred during the last and shallowest stage of the batholith formation (Montoya et al., 2019b). It is reasonable to suppose that the batholith building process not only provided the heat, part of the fluids and the metals, but also generated shallow extension and the formation of mineralized tension gashes during its ascent. The Piaxla batholith shallow position in the stratigraphic column suggest the enrichment of the magma in precious metals and metalloids by assimilation of the Cretaceous porphyry bodies (Montoya et al., 2019a), as recognized in other granite-related deposits in Northwest Europe (Nieva et al., 2019; Vallance et al., 2003). Furthermore, during the batholith emplacement the thermal anomaly remained elevated for a long period of time. In such geological environment, the mineralized fluids could come from three reservoirs: magmatic, metamorphic and/or meteoric. Microthermometry results, O-D, H_2O and CO_2 concentration, as well as noble gases trapped in FI, all point to the dominance of meteoric fluid, or air saturated groundwater in the hydrothermal system. He isotopes indicate that magmatic/mantle fluids are very low to negligible (< 2%), with a dominant contribution by a crustal reservoir, in good agreement with the geological context. The low salinity of the fluids (Tmi = −1.9 to 5.6 °C; wt% NaCl eq = 0–3.22 wt%) pleads in favor of silver transport as a bisulphur complex ($AgHS^-$; Zotov et al., 1995; Barnes, 1997). Hydrosulphide complex is dominant in neutral to alkaline pH and moderate to low salinity fluid (Akinfiev and Zotov, 2001; Gammons and Barnes, 1989; Seward and Barnes, 1997). In this situation, degassing may be more effective for silver deposition rather than conductive cooling or mixing. According to Stefansson and Seward, (2003), the hydrosulphide complex of silver can be stable in a wide range of temperature so that mixing or cooling may not dramatically reduce its solubility. However, the gas separation during degassing leads to the loss of volatile H_2S, which can effectively break the hydrosulphide complex and cause the deposition of silver (Seward, 1989; Stefansson and Seward, 2003). During the filling stage, hydraulic breccia and the evidence of heterogeneous trapping of FI illustrate the boiling/degassing process. Silver precipitation was probably linked to cooling temperature and pressure drop/boiling during the batholith ascent (Vallance et al., 2003).

The Eocene Ag-dominant mineralization event does not fit into a classic metallogenetic model. Based on the mineral paragenesis and following the literature of Mexican deposits it would be classified as intermediate sulphidation silver epithermal deposit (Camprubí and Albinson, 1996). In fact, these deposits are commonly hosted in calc-alkaline andesitic-dacitic arcs and found at the margins of high-sulphidation and/or porphyry deposits (John, 1999; 2001). The historical classification of San Dimas district as an IS epithermal deposit was based on mineralogical paragenesis and an incomplete knowledge of the chronological and geological context (Enriquez et al., 2018; Montoya et al., 2019b). If we accept the intermediate sulphidation character of the San Dimas Ag mineralization, the epithermal concept does not seem the better representation for such a deep (2–3 km), high temperature (up to ~350 °C) and plutonic-related deposit. However, the Eocene Ag-dominant mineralization event has also several characteristics that do not fit into the traditional "intrusion-related" type (IRGS; Lang and Baker, 2001; Hart, 2005), such as the location above a large and elongated batholith, the absence of regional mineralogical zonation with As–Au at the center of the batholith and Ag–Pb–Zn associations at the periphery, the very low gold content, a low sulphur fugacity and the dominant meteoric fluids.

The Oligocene Au-dominant mineralization structures are mainly hosted in N-S faults systems that have undergone multiple reactivations and are geographically and chronologically associated with Oligocene rhyolitic domes (at ca. 30 Ma, Montoya et al., 2019b). The Au-dominant veins are characterized by a single hydrothermal pulse, an intense sericitization and low-temperature formation (FI homogenization temperatures of 121 °C to 316 °C). The Au, Hg, Sb, and Bi metals association is commonly related to shallow epithermal systems (Gray et al.,1991; Bornhorst et al., 1995). The source of the fluids in this model, like classic LS epithermal models (Henley, 1986; Sillitoe, 1993; Hedenquist et al., 2000), is meteoric. The low salinity of the fluids (Tmi = −1.4 to 0.0 °C; wt% NaCl eq = 0–2.40 w%) argues in favor of gold transport as a bisulfide complex ($AuHS_2^-$; Zotov et al., 1995; Barnes, 1997). The paragenetic mineralogy, the low salinity of the fluids, as well as their gas content (H_2O > 99.5 mol percent of the liquid and gas phases, with CO_2 comprising most of the remaining gases, minor CO and traces of H_2, CH_4, N_2, C_2H_6, H_2S, C_3H_8, SO_2 and NO; Smith et al., 1982), is characteristic of the low sulphidation epithermal type (Henley, 1986). Concerning the sources of the FI trapped in quartz, H_2O reveals the dominant species as in Ag-dominant deposits. Ar-Ne-He isotopic

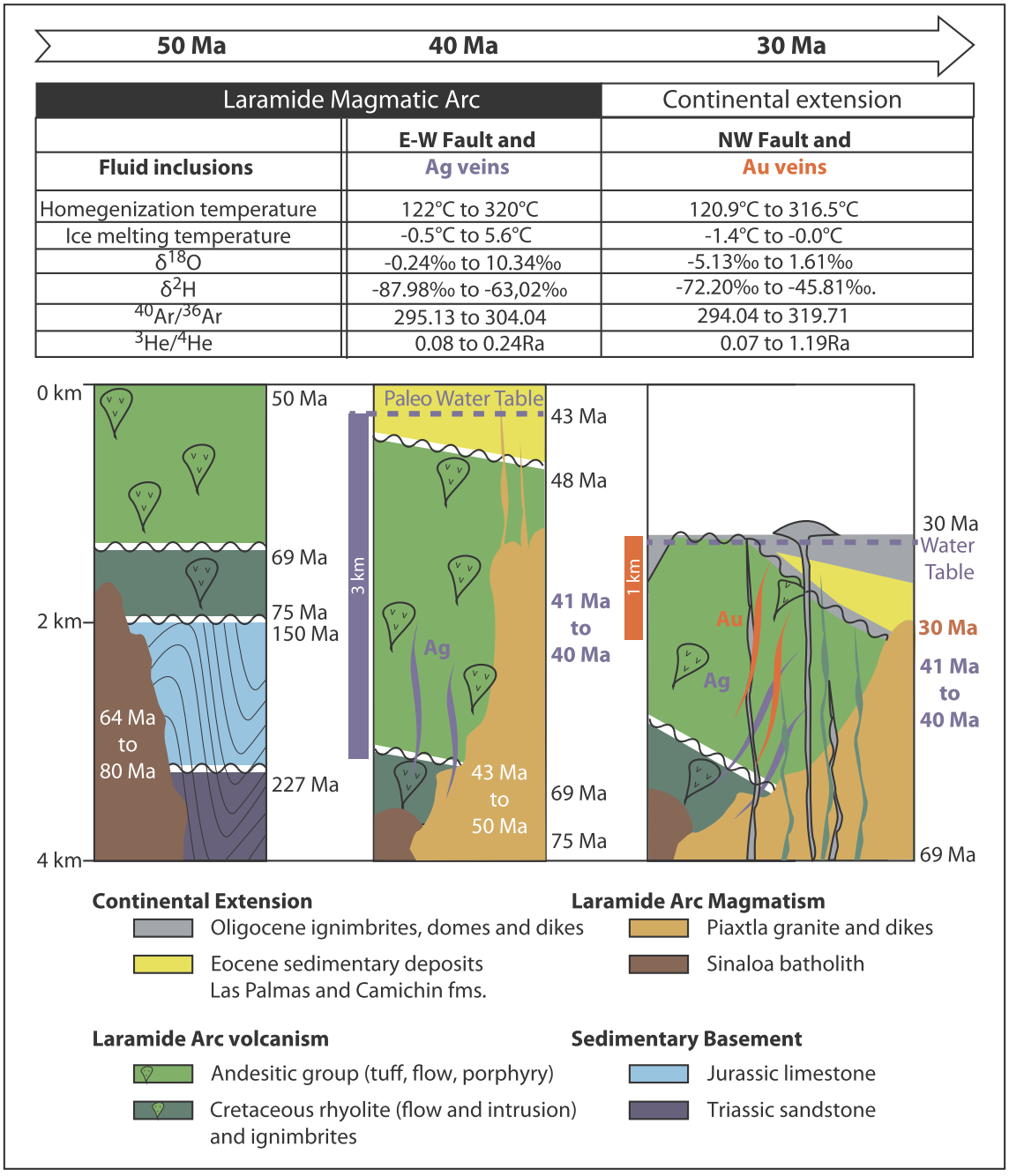

Fig. 9. Genetic model for the evolution for the Eocene-Oligocene telescoped San Dimas Ag–Au deposit. Boxes summarize the isotopic characteristics of the different reservoirs. Helium isotopic results are given in $^{3}He/^{4}He$ (Rac) ratios, and oxygen and deuterium in ‰ deviation relative to the SMOW standard. The synthesized geological cross-section is drawn from the East-West transect (modified from Montoya et al., 2019b). For legend, see Fig. 2.

systematics illustrates a hydrothermal system dominated by air saturated groundwater. Helium isotopes indicate that a not negligible contribution to FI has a magmatic/mantle origin (up to 24%), although some samples show a classical crustal signature. The Oligocene Au-dominant mineralization event matches all the geological and geochemical characteristics of the gold low sulphidation epithermal deposit model (Henley, 1986; Campbell and Larson, 1998).

As a consequence, it seems likely that the development of the San Dimas Oligocene Au-dominant mineralization event and probably many other epithermal precious metal deposits are related to the activation of extensional or transtensional fault systems within a major crustal discontinuity rooted in the lower crust or even in the mantle. The ascent of bimodal magma batches is accompanied by fluids rich in gas and sulphur, promoting the gold transport. The reactivation of the NNW-SSE structural corridor at ca. 30 Ma was an important event in the evolution of the SMO during a major pulse of crustal thinning associated to the ascent of asthenospheric melts (Ferrari et al., 2017). This process was accompanied by the melting of the mantle lithosphere and the lower crust and could explain the temporal and spatial association between the ascent of deep mineralizing fluids and silicic magmatism, and upper crustal extensional structures.

Finally, our study highlights the necessity to integrate geological observations and independent chronological and geochemical techniques to better understand the complexity of the hydrothermal magmatic processes involved in the formation of many Mexican ore deposits.

Declaration of Competing Interest

The authors declare that they have no known competing financial interests or personal relationships that could have appeared to influence the work reported in this paper.

Acknowledgments

This research is part of the PhD project of the first author at Universidad Nacional Autónoma de Mexico (UNAM) Postgraduate Program. The research was funded by CONACYT grant CB-237745-T and PAPIIT IV100117 to L. Ferrari. We thank Primero Mining (presently First Majestic Silver Corp.) for sharing unpublished information and for logistical support. Special thanks to Nicolas Landón for his strong support in the initial phase of the research and to Miguel Pérez for sharing his knowledge or the ore geology on the central SMO. We also thank Marina Vega for assistance at Laboratorio de Fluidos Corticales, personnel at Stable Isotope Laboratory at Laboratorio Nacional de Geoquímica y Mineralogía, Instituto de Geología, Universidad Nacional Autónoma de México, Ciudad de México, and Juan Tomás Vazquez for the elaboration of thin sections. We thank Maria Grazia Misseri and Mariano Tantillo from INGV-Palermo for helping in samples preparation, H2O-CO2 concentration, and noble gases isotope analysis of fluid inclusions, as well as Fausto Grassa for useful discussions on data elaboration. Authors are special grateful to Seequent for providing an academic license of Leapfrog Mining.

Appendix A. Supplementary data

Supplementary data to this article can be found online at https://doi.org/10.1016/j.oregeorev.2020.103427.

References

Akinfiev, N., Zotov, A., 2001. Thermodynamic description of chloride, hydrosulfide, and hydroxo complexes of Ag (I), Cu (I), and Au (I) at temperatures of 25–500°C and pressures of 1–2000 bar. Geochem. Int. 39, 990–1006.

Albinson, T., Norman, D.I., Cole, D., Chomiak, B., 2001. Controls on formation of low sulfidation epithermal deposits in Mexico: Constraints from fluid inclusion and stable isotope data. In: New Mines and Discoveries in Mexico and Central America. Society of Economic Geology Special Publication, 8, 1–32.

Ballentine, C.J., 1997. Resolving the mantle He/Ne and crustal 21Ne/ 22Ne in well gases. Earth Planet. Sci. Lett. 152, 233–249.

Ballentine, C.J., Mazurek, M., Gautschi, A., 1994. Thermal constraints on crustal rare gas release and migration: Evidence from Alpine fluid inclusions. Geochim. Cosmochim. Acta 58, 4333–4348.

Ballentine, C., Burgess, R., Marty, B., 2002. Tracing fluid origin, transport and interaction in the crust. In: Porcelli, D., Ballentine, C.J., Wieler, R. (Eds.), Noble Gases. Geochemistry and Cosmochemistry, 47, 539–614.

Barnes, H., 1997. Geochemistry of Hydrothermal Ore Deposits, Third Edition. Wiley-Interscience Inc., New York.

Batista Cruz, R.Y., Rizzo, A.L., Grassa, F., Bernard Romero, R., González Fernández, A., Kretzschmar, T.G., Gómez-Arias, E., 2019. Mantle degassing through continental crust triggered by active faults: The case of the Baja California Peninsula, Mexico. Geochem. Geophys. Geosyst. 20, 1912–1936.

Bodnar, R., Reynolds, T., Kuehn, C., 1985. Fluid inclusion systematics in epithermal systems, In: Berger, B.R., Bethke, P.M. (Eds.), Geology and geochemistry of epithermal systems. Rev. Economic Geology, 2, 73–97.

Bornhorst, T., Nurmi, P., Rasilainen, K., Kontas, E., 1995. Trace element characteristics of selected epithermal gold deposits of North America. Geol. Surv. Finland Spec. Pap. 20, 47–52.

Burlinson, K., 1988. An instrument for fluid inclusion decrepitometry and examples of its application. Bull. Mineral. 111, 267–278.

Burlinson, K., Dubessy, J., Hladky, G., Wilkins, R., 1983. The use of fluid inclusio decrepitometry to distinguish mineralised and barren quartz veins in the Aberfoyle tin-tungsten mine area. J. Geochem. Explor. 19, 319–333.

Campbell, A., Larson, P., 1998. Introduction to stable isotope applications in hydrothermal systems. Rev. Econ. Geol. 10, 173–193.

Camprubí, A., 2013. Tectonic and Metallogenic History of Mexico. Soc. Econ. Geol., Special Publication 17, 201–243.

Camprubí, A., Albinson, T., 1996. Depósitos epitermales en México: Actualización de su conocimiento y reclasificación empírica. Boletín de la Sociedad Geológica Mexicana 58, 27–81.

Camprubí, A., Albinson, T., 2007. Epithermal deposits in México-Update of current knowledge, and an empirical reclassification. Geol. Soc. Am. Special Papers 422 (14), 377–415.

Chen, Y., Bao, J., Zhang, Z., Chen, H., Liu, Y., 2003. Laumontitization as exploration indicator of epithermal gold deposits: A case study of the Axi and other epithermal systems in West Tianshan, China. Geochem. J. 22, 289–303.

Chen, Y., Pirajno, F., Wu, G., Qi, J., Xiong, X., 2012. Epithermal deposits in North Xinjiang, NW China. Int. J. Earth Sci. 101, 889–917.

Churchill, R.K., 1980. Meteoric water leaching and ore genesis at the Tayoltita silver-gold mine, Durango, Mexico. Unpublished Ph.D. dissertation, 162.

Clarke, M., Titley, S., 1988. Hydrothermal evolution in the formation of silver-gold veins in the Tayoltita mine, San Dimas district, Mexico. Econ. Geol. 83 (8), 1830–1840.

Conrad, M., Chamberlain, C.P., 1992. Laser-based, in situ measurements of fine-scale ariations in the $\partial^{18}O$ of hydrothermal quartz. Geology 20 (9), 812–816.

Cooke, D., Simmons, S., 2000. Characteristics and genesis of epithermal gold deposits – SEG Reviews. Econ. Geol. 13, 221–244.

Einaudi, M., 1992. Ore deposits in the Oquirrh and Wasatch Mountains, Utah: Examples of large-scale water-rock interaction. In: eds,, . (Ed.), Kharaka and Maest. Water-Rock Interaction, pp. 879–887.

Enriquez, E., Rivera, R., 2001. Geology of the Santa Rita Ag-Au Deposit, San Dimas District, Durango, Mexico. Special Publication, Soc. Econ. Geol. 8, 39–58.

Enríquez, E., Iriondo, A., Camprubí, A., 2018. Geochronology of Mexican mineral deposit. VI: The Tayoltita low-sulfidation epithermal Ag-Au district, Durango and Sinaloa. Boletín de la Sociedad Geológica Mexicana 70 (2), 531–547.

Ferrari, L., Valencia-Moreno, M., Bryan, S., 2007. Geology of the western Mexican volcanic belt and adjacent Sierra Madre Occidental and Jalisco block, in Delgado-Granados. Geol. Soc. Am. Spec. Pap. 334, 65–83.

Ferrari, L., López-Martínez, M., Orozco-Esquivel, T., Bryan, S., Duque-Trujillo, J., Lonsdale, P., 2013. Late Oligocene to Middle Miocene rifting and synextensional magmatism in the southwestern Sierra Madre Occidental, México: The beginning of the Gulf of California rift. Geol. Soc. Am. 9 (5), 1–40.

Ferrari, L., Orozco, T., Bryan, S., Lopez, M., Silva, A., 2018. Cenozoic extension and magmatism in western Mexico: Linking the Sierra Madre Occidental Silicic Large Igneous Province and the Comondú Group with the Gulf of California rift. Earth-Sci. Rev. 183, 115–152.

Gammons, C., Barnes, H., 1989. The solubility of Ag2S in near-neutral aqueous sulfide solutions at 25 to 300°C. Geochim. Cosmochim. Acta 53, 279–290.

Giggenbach, W., 1992a. Magma degassing and mineral deposition in hydrothermal systems along convergent plate boundaries. Econ. Geol. 87, 1927–1944.

Giggenbach, W.F., 1992b. The composition of gases in geothermal and volcanic systems as a function of tectonic setting. International Symposium Water-Rock Interaction 7th, Park City, 873–878.

Graham, D.W., 2002. Noble gas isotope geochemistry of Mid-Ocean ridge and Ocean island basalts: Characterization of mantle source reservoirs. In Noble Gases in Geochemistry and Cosmochemistry, Rev. Mineral. Geochem. 47, In: Porcelli, D.P., Ballentine, C.J., Wieler, R. (Eds.), Mineralogical Society of America, 247–317.

Gray, D., Goldfarb, R., Detra, D., Slaughter, K., 1991. Geochemistry and exploration criteria for epithermal cinnabar and stibnite vein deposits in the Kuskokwim River region, southwestern Alaska. J. Geochem. Explor. 41, 363–386.

Hart, C., 2005. Classifying, distinguishing and exploring for intrusion-related gold systems: The Gangue. Newslett. Geol. Assoc. Can. Miner. Deposits Div. 87, 4–9.

Heald, P., Foley, N., Hayba, D., 1987. Comparative anatomy of volcanic-hosted epithermal deposits: Acid-sulfate and adularia-sericite types. Econ. Geol. 82 (1), 1–26.

Hedenquist, J.W., 1987. Mineralization associated with volcanic-related hydrothermal systems in the circum-Pacific basin: Circum Pacific. Energy and Mineral Resource Conference, 4th, Singapore, August 17–22, 513–524.

Hedenquist, J.W., Arribas, A.J., 2000. Epithermal gold deposits: I. Hydrothermal processes in intrusion-related systems, and II. Characteristics, examples and origin of epithermal gold deposits. Soc. Econ. Geol. 31, 13–63.

Henley, R.W., Hedenquist, J.W., 1986. Introduction to the geochemistry of active and fossil geothermal systems. In: Henley, R.W., Hedenquist, J.W., Roberts, P.J. (Eds.), Guide to the active epithermal systems and precious metal deposits of New Zealand. Monography Series Mineral Deposits, 26, 129–145.

Henry, C., McDowell, F., Silver, L., 2003. Geology and geochronology of granitic batholithic complex, Sinaloa, México: Implications for Cordilleran magmatism and tectonics. Geological Society of America, Special Paper 374: Tectonic evolution of northwestern Mexico and the Southwestern USA, Vol. 374, pp. 237–273.

Henry, D., Fredrikson, G., 1987. Geology of southern Sinaloa adjacent to the Gulf of California. Geological Society of America, Map and Chart Series. Map MCH063, 14p.

Henshaw, P.C., 1953. Geology and Ore Deposit of the San Dimas District. Sinaloa and Durango, Private document, pp. 531.

Horner, J., Enriquez, E., 1999. Epithermal precious metal mineralization in a strike-slip corridor: The San Dimas District, Durango, Mexico. Econ. Geol. 94 (8), 1375–1380.

John, D., 1999. Magmatic influence on characteristics of Miocene low-sulfidation Au-Ag deposits in the northern Great Basin (abs). Geol. Soc. Am. Abstracts Program 31 (7), pp. A-405.

John, D.A., Garside, L.J., Wallace, A.R., 1999. Magmatic and tectonic setting of late Cenozoic epithermal gold-silver deposits in northern Nevada, with an emphasis on the Pah Rah and Virginia Ranges and the northern Nevada rift: Geological Society of Nevada. Spring Field Trip Guidebook Special Publication 29, 64–158.

John, D., 2001. Miocene and Pliocene epithermal gold-silver deposits in the northern Great Basin, western USA: Characteristics, distribution, and relationship to magmatism. Econ. Geol. 96, 1827–1853.

Kendrick, M., Burnard, P., 2011. Noble gases and halogens in fluid inclusions: a journey through the earth's crust. In: The noble gases as geochemical tracers. Springer, Berlin, Heidelberg, pp. 319–369.

Kennedy, B.M., Hiyagon, H., Reynolds, J.H., 1990. Crustal neon: A striking uniformity. Earth Planetary Sci. Lett. 98, 277–286.

Kerrich, R., Goldfarb, R., Groves, D., Garwin, S., Jia, Y., 2000. The characteristics, origins, and geodynamic settings of supergiant gold metallogenic provinces. Sci. China (Series D) 43, 68.
Lang, J., Baker, T., 2001. Intrusion-related gold systems: The present level of understanding. Miner. Deposita 36, 477–489.
Leach, T., Corbett, G., 1994. Porphyry-related carbonate-base-metal gold systems: Characteristics. In: Rogerson, R. (Ed.), Geology, exploration and mining conferences. The Australasian Institute of Mining and Metallurgy, 84–91.
Lindgren, W., 1922. A suggestion for the terminology of certain mineral deposits. Econ. Geol. 17 (4), 292–294.
Lindgren, W., 1933. Mineral deposits. McGraw-Hill Book Company Inc, London.
Mamyrin, B., Tolstikyn, I., 2013. Helium isotope in nature. Dev. Geochem. 3, 273p.
Manning, A.H., Hostra, A.H., 2017. Noble gas data from Goldfield and Tonopah epithermal Au-Ag deposits, ancestral Cascades Arc, USA: Evidence for a primitive mantle volatile source. Ore Geol. Rev. 89, 683–700.
Mikucki, E., 1998. Hydrothermal transport and depositional processes in Archean lode-gold systems: A review. Ore Geol. Rev. 13, 307–321.
Moncada, D., Baker, D., Bodnar, R., 2017. Mineralogical, petrographic and fluid inclusion evidence for the link between boiling and epithermal Ag-Au mineralization in the La Luz area, Guanajuato Mining District, México. Ore Geol. Rev. 89, 143–170.
Moncada, D., Mutchler, S., Nieto, A., Reynolds, T.J., Rimistidt, J.D., Bodnar, R.J., 2012. Mineral textures and fluid inclusion petrography of the epithermal Ag-Au deposits at Guanajuato, Mexico: Application to exploration. J. Geochem. Explor. 114, 20–35.
Montoya-Lopera, P., Ferrari, L., Levresse, G., Abdullin, F., Mata, L., 2019a. New insights into the geology and tectonics of the San Dimas mining district, Sierra Madre Occidental, Mexico. Ore Geol. Rev. 105, 273–294.
Montoya-Lopera, P., Levresse, G., Ferrari, L., Orozco-Esquivel, T., Hernandez-Quevedo, G., Abdullin, F., 2019b. New geological, geochronological and geochemical characterization of the San Dimas mineral system: Evidence for a telescoped Eocene-Oligocene Ag/Au deposit in the Sierra Madre Occidental, Mexico. Ore Geology Reviews. In press.
Nieto-Samaniego, A., Olmos-Moya, M., Levresse, G., Alaniz-Alvarez, A., Abdullin, F., Pilar-Martinez, A., 2019. Thermochronology and exhumation rates of granitic intrusions at Mesa Central, Mexico. Int. Geol. Rev. 1–8.
Nieva, A.M.R., Moura, A., Leal gomes, C.A., Pereira, M.F., Corfu, F.,, 2019. The granite-hosted Variscan gold deposit from Santo Antonio mine in the Iberian massif (penedono, NW Portugal): Constraints from mineral chemistry, fluid inclusions, sulfur and noble gases isotopes. J. Iberian Geol. 1–27.
Ozima, M., Podosek, A.P., 2002. Noble Gas Geochemistry, second, ed. Cambridge University Press, Cambridge, pp. 10–15.
Panteleyev, A., 1996. Epithermal Au-Ag: Low sulphidation, in selected British Columbia Mineral Deposit Profiles. British Columbia Ministry of Employment and Investment, Open File 2, 41–44.
Pinti, D.L., Castro, M.C., Shouakar-Stash, O., Tremblay, A., Garduño, V.H., Hall, C.M., Helie, J.F., Ghaleb, B., 2013. Evolution of the geothermal fluids at Los Azufres, Mexico as traced by noble gases ∂18O, ∂D, ^{13}C and $^{87}Sr/^{86}Sr$. J. Volcanol. Geoth. Res. 249, 1–11.
Pirajno, F., 2009. Hydrothermal processes and mineral systems. Springer, Berlin, Australia, pp. 1250p.
Pokrovski, Gleb S., Akinfiev, Nikolay N., Borisova, Anastassia Y., Zotov, Alexandre V., Kouzmanov, Kalin, 2014. Gold speciation and transport in geological fluids: Insights from experiments and physical-chemical modelling. Geological Society, London, Special Publications 402 (1), 9–70. https://doi.org/10.1144/SP402.4.
Prokofiev, V., Pek, A., 2015. Problems in estimation of the formation depth of hydrothermal deposits by data on pressure of mineralization fluids. Geol. Ore Deposits 57, 1–20.
Ramos-Rosique, A., Bryan, S., Ferrari, L., Allen, C., Lopez-Martinez, M., Rankin, A., 2010. Timing and evolution of Late Oligocene to Miocene magmatism in the southern Sierra Madre Occidental silicic large igneous province: Insights from zircon chronochemistry and $^{40}Ar/^{39}Ar$ geochronology. EGU General Assembly Conference Abstracts 12, 9788.
Romberger, S., 1986. Ore deposits #9 Disseminated gold deposits. Geosci. Can. 13, 23–31.
Sarda, P., Staudacher, T., Allegre, C.J., 1988. Neon isotopes in submarine basalts. Earth Planetary Sci. Lett. 91, 73–88.
Seward, T., 1989. The hydrothermal chemistry of gold and its implications for ore formation: Boiling and conductive cooling as examples. Econ. Geol. Monogr. 6, 398–404.
Seward, T., Barnes, H., 1997. Metal transport by hydrothermal ore fluids. In: Dans H.. Barnes, Geochemistry of hydrothermal ore deposits, (third ed.) John Wiley and Sons, New York, 435–486.
Sheppard, S., 1986. Characterization and isotopic variations in natural waters. In: Valley, J.W., Taylor, H.P.J., O'Neil, J.R., (Eds)., Stable isotope in high temperature geological processes. Mineralogical Society of America, Reviews in Mineralogy, 16, 165–183.
Sheppard, S., Nielsen, R., Taylor, H., 1969. Oxygen and hydrogen isotope ratios of clay minerals from porphyry copper deposits. Econ. Geol. 64, 755–777.
Shuster, D.L., Farley, K.A., 2005. Diffusion kinetics of proton-induced ^{21}Ne, ^{3}He, and ^{4}He in quartz. Geochim. Cosmochim. Acta 69, 2349–2359.
Simmons, S.F., White, N.C., John, D.A., 2005. Geological characteristics of epithermal precious and base metal deposits. Society of Economic Geologist, 100th Anniversary, 485–522.
Simmons, S., Sawkins, F., Schlutter, D., 1986. Mantle derived helium in two hydrothermal ore deposits, Peru. Nature 329, 429–432.
Smith, D., Albinson, T., Sawkins, F., 1982. Geologic and fluid inclusion studies of the Tayoltita silver-gold vein deposit, Durango Mexico. Soc. Econ. Geol. 1120–1145.
Steele-Maclnnis, M., Lecumberri-Sanchez, P., Bodnar, R., 2012. Short note: HokieFlincs_H_2O-NaCl: A Microsoft Excel spreadsheet for interpreting microthermometric data from fluid inclusions based on the PVTX properties of H_2O-NaCl. Comput. Geosci. 49, 334–337.
Stefansson, A., Seward, T., 2003. Experimental determination of the stability and stoichiometry of sulphide complexes of silver (I) in hydrothermal solutions to 400°C. Geochim. Cosmochim. Acta 67, 1395–1413.
Stefansson, A., Seward, T., 2004. Gold (I) complexing in aqueous sulphide solutions to 500°C at 500 bars. Geochemica et Cosmochimica Acta 68 (20), 4121–4143.
Taylor, H., 1974. The application of oxygen and hydrogen isotopic studies to problems of hydrothermal alteration and ore deposition. Econ. Geol. 69 (6), 843–883.
Vallance, J., Cathelineau, M., Boiron, M., Fourcade, S., Shepherd, T., Naden, J., 2003. Fluid-rock interactions and the role of late Hercynian aplite intrusion in the genesis of the Castromil gold deposit, northern Portugal. Chem. Geol. 194, 201–224.
Velador, J., Heizler, W., Campbell, A., 2010. Timing of magmatic activity and mineralization and evidence of a long-lived hydrothermal system in the Fresnillo silver district, Mexico: Constraints from $^{40}Ar/^{39}Ar$ geochronology. Econ. Geol. 105, 1335–1349.
Wang, J., Wang, X., Liu, J., Zhai, D., Wang, Y., 2019. Geology, geochemistry, and geochronology of gabbro from the Haoyaoerhudong Gold Deposit, Northern Margin of the North China Craton. Minerals 9, 63.
White, C., 2003. Epithermal Gold Deposits. Society of Economic Geologist Beijing Gold Workshop 25–26 Oct, 118.
Zajacz, Z., Seo, J., Candela, P., Piccoli, P., Heinrich, C., Guillong, M., 2010. Alkali metals control the release of gold from volatile-rich magmas. Earth Planet. Sci. Lett. 297, 50–56.
Zamora-Vega, O., Richards, J., Spell, T., Dufrane, S., Williamson, J., 2018. Multiple mineralization events in the Zacatecas Ag-Pb-Zn-Cu-Au district, and their relationship to the tectonomagmatic evolution of the Mesa Central, Mexico. Ore Geol. Rev. 102, 519–561.
Zhang, C., Wang, E., Bi, Z., Han, R., Shao, J., Liu, B., 2019. Geochronology and isotope geochemistry studies of an epithermal gold deposit in the northern Lesser Khingan Range, NE China: The Gaosongshan example. Ore Geol. Rev. 105, 356–374.
Zhu, Y., An, F., Tan, J., 2011. Geochemistry of hydrothermal gold deposits: A review. Geosci. Front. 2 (3), 367–374.
Zotov, A., Kudrin, A., Levin, K., Shikina, N., VaŕYash, L., 1995. Experimental studies of the solubility and complexing of selected ore elements (Au, Ag, cu, Mo, As, Sb, Hg) in aqueous solutions. In: Shmulovich, K.L., Yardley, B.W.D., Gonchar, G.G. (Eds.), Fluids in the Crust. Equilibrium and Transport Properties, 95–138.

Capítulo 5: **Conclusiones**

En la presente tesis contribuimos a mejorar el conocimiento sobre la relación tectono-magmática y el desarrollo de multiples mineralizaciones en el distrito minero de San Dimas en tres aspectos principales:

1) *Re-evaluación estratigráfica*: se demostró que las unidades geológicas mas antiguas del distrito son pertenecientes al CVI con una edad Cretácico tardío y por lo tanto representan el equivalente volcánico del batolito de Sinaloa y pueden correlacionarse con la Formación Tahuramara de Sonora. Las secuencias lavícas del CVI son cubiertas por lavas intrusionadas por cuerpos hipoabisales de afinidad intermedia (Grupo Andesítico, GA) de edades Paleocénicas. GA es de particular importancia en el distrito debido a que eran asociados geneticamente a la mineralización por presentar ambos edades similares, adicional por ser las hospedantes de la mayor parte de la mineralización (Enríquez y Rivera, 2001b).

   Basados en las nuevas edades U/Pb en circón reportadas en este estudio, mas las relaciones de corte entre Piaxtla y GA, demostramos que estos cuerpos intermedios hacen parte de pulsos magmáticos desarrollados entre el Paleoceno al Eoceno temprano, y que las edades K-Ar, Ar-Ar reportadas por Enríquez y Rivera (2001b) eran el resultado del reseteo parcial de los minerales debido a la alta alteración hidrotermal en el área.

   Observamos también que el Batolito Piaxtla intruye todo el CVI desde la base hasta el techo, y que fue formado en diferentes pulsos magmáticos separados textural, composicional y geocronologicamente. Nuestras nuevas edades de U/Pb delimitan el Piaxtla entre ~49 a 44 Ma confirmando así las edades reportadas por Enríquez y Rivera (2001b) y Henry et al., (2003). Adicional a lo anterior, y como una contribucción importante del estudio, son las nuevas edades reportadas para los diques intermedios “San Rita” y “Bolaños”, los cuales hacen parte de los últimos pulsos magmáticos del Piaxtla. Estas edades son relevantes para el estudio, debido a que estan asociadas geneticamente con la mineralización.

   Basados en la ocurrencia de la formación sedimentaria de afinidad continental Las Palmas, la Fm Camichin, y a las nuevas edades U/Pb de las mismas, se demuestra el inicio de una extensión en el Eoceno. Regionalmente, correlacionamos estas formaciones sedimentarias con los depositos de capas rojas continentales que marcan un periodo de erosión y baja actividad volcánica entre el CVI y SVS reportado por

otros autores (McDowell y Keizer, 1977; McDowell y Clabaugh, 1979; Ferrari et al., 2007).

Las nuevas edades U/Pb de la base de las sucesiones ignimbríticas del SVS en el distrito, son consistentes con las edades de las secuencias volcánicas de Durango reportadas previamente por otros autores en un rango de ~31 a 29 Ma (McDowell y McIntosh, 2012), confirmando así la prolongación al Oeste de esta secuencia en la SMO.

En conjunto la nuevas observaciones geológicas y edades de U-Pb demuestran que existen tres pulsos magmáticos mayores: 1) el magmatismo asociado al arco Laramide, 2) el magmatismo asociado al batolito Piaxtla y 3) el volcanismo sílicico y bimodal de la gran provincia silícica de la SMO.

2) *Re-evaluación de la mineralización del distrito de San Dimas:* la integración de una detallada reevaluación geológica, geocronológica, tectónica y petrográfica versus análisis multivariados, tales como geoquímica, microtermometría, gases nobles e isotopía estable, nos permitío reevaluar el origen del clásico epitermal de baja sulfuración de San Dimas y a su vez desarollar un nuevo modelo genético para el distrito (Montoya-Lopera et al., 2020).

La mineralización del distrito de Ag-Au San Dimas es un ejemplo de un yacimiento telescopeado desarrollado en dos eventos mineralizantes separados en el tiempo: i) evento de vetas eocénicas (~40-41 Ma; Montoya et al., 2019b) dominantes en Ag, hospedadas en las secuencias lavícas del CVI y desarrolladas principalmente en sistemas extensionales incipientes de orientación E-W. Estos sistemas son tipo cuarzo-adularia-rodocrosita y se desarrollan en tres eventos de apertura, relleno y cierre. Basados en los resultados de REE en circones de la roca caja (relaciones Eu/Eu* y (Ce/Nd)/Y) Montoya et al., 2019b) y geocronología se asocian genéticamente las vetas de Ag dominante a los últimos pulsos hidratados y oxidados del batolito Piaxtla (~44 Ma Montoya et al., 2019a).

Los resultados de microtermometría, O-D, H_2O y concentración de CO_2 así como tambien los resultados de gases nobles atrapados en IF, indican dominancia de fluidos meteóricos o aire saturado en el sistema hidrotermal (Montoya et al., 2020). Los isotópos de He indican bajo aporte de fluidos magmáticos o de manto (menos al 2%), con una contribucción importante cortical, lo cual estaría de acuerdo con el contexto geológico (Montoya et al., 2020). La baja salinidad de los fluidos (Tmi =-1.9 to 5.6ºC; wt% NaCl eq = 0 to 3.22 wt%) favorece el transporte de Ag como complejo bisulfurado (AgHS-; Zotov et al., 1995; Barnes, 1997). En este contexto, la

degasificación sería mas efectiva para la depositación de Ag antes que el enfriamiento o mezcla (Montoya et al., 2020).

Debido a la profunidad de emplazamiento de las vetas (2-3km), la alta temperatura de formación (mayor a ~350ºC) y fisicoquímica de los fluidos hidrotermales, el sistema eocénico dominante en Ag no podría catalogarse como clásico epitermal de baja sulfuración.

ii) evento de vetas Oligocénicas dominantes de Au (~30Ma Montoya et al., 2019b), emplazados principalmente en sistemas estructurales de orientación NNW-SSE, se desarrollan como un solo pulso hidrotermal, tipo sericita-clorita (Montoya et al., 2019b). Estos sistemas de Au dominante se asocian geneticamente a domos riolíticos de afinidad reducida (~31-29 Ma Montoya et al., 2019b) desarrollados durante el inicio de la extensión que llevó a la apertura del Golfo de California.

Las vetas de Au dominante se caracterizan por tener bajas temperaturas de homogenización (121ºC to 316ºC) (Montoya et al., 2020). La asociación mineral del Au con Hg, Sb y Bi sugiere un emplazamiento superficial (Gray et al., 1991; Bornhorst et al., 1995). La fuente de estos fluidos sigue los clásicos modelos epitermales de baja sulfuración (Henley y Hedenquist, 1986; Sillitoe, 1993; Hedenquist y Arribas, 2000). La baja salinidad de los fluidos (Tmi = -1.4 to 0.0ºC; wt% NaCl eq = 0 to 2.40 w%) favorece el transporte de Au como un complejo bisulfatado (AuHS-2; Zotov et al., 1995; Barnes, 1997). Por lo tanto, basados en las anteriores caracteristicas, seguido por el bajo contenido de gases en IF (IF bifasicas H_2O > 99.5 mole percent, Montoya et al., 2020) indicarían que estas vetas se catalogarían como vetas epitermales de baja sulfuración (Henley y Hedenquist,1986).

Con respecto a los sistemas isotópicos, los resultados de Ar-Ne-He indican un sistema hidrotermal dominado por aire saturado. Isótopos de He en gases de IF mostraron alta contribución de origen magmático/mantélico (encima de 24%), lo cual es coherente con el ambiente geológico (Montoya et al., 2020).

Como consecuencia, las vetas de Au dominante se asocian a la activación de sistemas de fallas extensionales o transtensionales de alto ángulo las cuales permiten el ascenso de magma bimodal acompañado de fluidos ricos en sulfuros promoviendo el transporte de Au (Montoya et al., 2020). La reactivación de esos sistemas (NNW-SSE) comenzo para los 30 Ma durante la evolución de la SMO (Ferrari et al., 2017)

3) *Re-evaluación geocronológica al sur de San Dimas*

Observamos la presencia de miembro basal del CVI ~77-75 Ma (equivalente al Miembro Socavón en SD, ~75-73 Ma) en contacto discordante con la formación Palmarito (~52 Ma, correlacionada con la Fm Las Palmas), indicando una erosión casi completa del CVI o una no deposición del GA por ser ya un alto del basamento al sur de San Dimas (Montoya et al., 2019 a). Lo anterior trae consigo implicaciones importantes desde el punto de vista del yacimiento y la tectónica regional del área.

Implicaciones desde el punto de vista tectónico: 1) el bloque al sur del Piaxtla, Mala Noche – Causitas, estaría por lo menos 1000 metros mas elevado; 2) a escala regional, el desarrollo de estructuras extensionales regionales EW en la SMO durante el Cretácico tardío al Oligoceno temprano debe ser estudiado con mayor detalle.

Implicaciones desde el punto de vista del yacimiento: 1) las secuencias volcánicas Buelna, Portal y GA se habría exhumado en el bloque Causitas – Mala Noche para los ~40-41 Ma, edad de formación de las vetas de Ag dominante ; 2) San Dimas representa un bloque hundido donde se preserva la sobreimposición de los diferentes eventos mineralizantes desde la raíz hasta el techo, hecho que permitió la formación de un distrito excepcional de clase mundial.

Capítulo 6: Referencias

Abdullin, F., Solari, L., Ortega-Obregon, C., & Sole, J. (2018). New fission-track results from the northern Chiapas Massif area, SE Mexico: trying to reconstruct its complex thermo-tectonic history. Rev. Mex. Cienc. Geol. 35 (1), 79-92.

Albinson, T., Norman, D., Cole, D., & Chomiak, B. (2001). Controls on formation of low sulfidation epitermal deposits in Mexico: constraints from fluid inclusion and stable isotope data. In: New Mines and Discoveries in Mexico and Central America 8. Society of Economic Geology Special Publication, 1-32.

Barnes, H. (1997). Geochemistry of hydrothermal ore deposits (Third edition). New York: Wiley-Interscience, Inc.

Bornhorst, T., Nurmi, P., Rasilainen, K., & Kontas, E. (1995). Trace element characteristics of selected epithermal gold deposits of North America. Geological Survey of Finland Special Paper, 20, 47-52.

Camprubí, A., Ferrari, L., Cosca, M., Cardellach, E., & Canals, A. (2003). Ages of epithermal deposits in Mexico: regional significance and links with the evolution of Tertiary volcanism. Economic Geology, 1029-1037.

Conrad, M., Petersen, U., & O´Niel, J. (1992). Evolution of an Au-Ag producing hydrothermal system: the Tayoltita mine, Durango, Mexico. Economic Geologist, 1451-1474.

Conrad, M., & Chamberlain, C. (1992). Laser-based, in situ measurements of fine-scale variations in the ^{18}O of hydrothermal quartz. Geology, 812-816.

Coplen, T. (1988). Normalization of oxygen and hydrogen isotope data. Chemical Geology (Isotope Geoscience Section) 72, 293-297.

Coplen, T., Brand, W., Gehre, M., Groning, M., Meijer, A., & Verkouteren, T. (2006). New guidelines for $d^{12}C$ measurements. Analytical Chemistry, 78, 2439-2441.

Clarke, M. (1986). Hydrothermal geochemistry of Ag-Au veins in the Tayoltita and the San Dimas mining district, Durango and Sinaloa, Mexico. Unpublished Ph.D. thesis, 151.

Clarke, M., & Title, S. (1988). Hydrothermal evolution in the formation of silver-gold veins in the Tayoltita mine, San Dimas district, Mexico. In: New Mines and Mineral

Discoveries in Mexico and Central America 8. Society of Economic Geologist Special Publication, 1830-1840.

Di Piazza, A., Rizzo, A., Barberi, F., Carapezza, M., De Astis, G., Romano, C., & Sortino, F. (2015). Geochemistry of the mantle source and magma feeding system beneah Turrialba volcano, Costa Rica. Lithos 232, 319-335.

Donelick, R., OSullivan, P., & Ketcham, R. (2005). Apatite fission-track analysis. Rev. Mineral. Geochem. 58 (1), 49-94.

Enríquez, E., & Rivera, R. (2001a). Geology of the Santa Rita Ag-Au Deposit, San Dimas District, Durango, México. In: New Mines and Mineral Discoveries in Mexico and Central America 8. Society of Economic Geologist Special Publication, 39-58.

Enríquez, E., & Rivera, R. (2001b). Timing of magmatic and hydrothermal activity in the San Dimas District, Durango, Mexico. In: New Mines and Mineral Discoveries in Mexico and Central America. Society of Economic Geologist Special Publication 8, 33-38.

Enríquez, E., Iriondo, A., & Camprubí, A. (2018). Geochronology of Mexican mineral deposits. VI: The Tayoltita low-sulfidation epithermal Ag-Au district, Durango and Sinaloa. Bol. Soc. Geol. Mexico., 70, 531-547.

Ferrari, L., Bryan, S., & Rosique, A. (2014). Crustal extension, silicic magmatism, and epithermal mineralization in the Sierra Madre Occidental : a multiphase history. 4to Congreso: Tendencias de la Minería en México. AIMMGM AC, Durango, 9-14.

Ferrari, L., Orozco-Esquivel, T., Lopez-Martinez, M., Martinez-Resendiz, V., & Avalos-Ledesma, A. (2018). Geochronology and isotope geochemistry of the mafic volcanism of the Sierra Madre Occidental silicic large igneous province, Mexico: Implications for the Cenozoic geodynamics of western North America. 11th South American Symposium on Isotope Geology (SSAGI).

Ferrari, L., Rosas-Elguera, J. (2000). Late Miocene to Quaternary extension at the northern boundary of the Jalisco block, western Mexico: the Tepic-Zacoalco rift revised. Geol. Soc. Am. Spec. Pap. 334, 41–64.

Ferrari, L., Valencia-Moreno, M., & Bryan, S. (2005). Magmatismo y tectónica en la Sierra Madre Occidental y su relación con la evolución de la margen occidental de Norteamérica. Boletín de la Sociedad Geológica Mexicana, 3, 343-378.

Ferrari, L., Valencia-Moreno, M., & Bryan, S. (2007). Geology of the western Mexican Volcanic Belt and adjacent Sierra Madre Occidental and Jalisco block. Geol. Soc. Am. Spec. Pap. 334, 65-83.

Goldoff, B., Webster, J., & Harlov, D. (2012). Characterization of fluor-chlorapatites by electron probe microanalysis with a focus on time-dependent intensity variation of halogens. Am. Mineral. 97, 1103-1115.

Gray, D., Goldfard, R., Detra, D., & Slaughter, K. (1991). Geochemistry and exploration criteria for epithermal cinnabar and stibnite vein deposits in the Kuskokwim River region, southwestern Alaska. Journal of Geochemical Exploration 41, 363-386.

Hasebe, N., Barbarand, J., Jarvis, K., Carter, A., & Hurford, A. (2004). Apatite fission-track chronometry using laser ablation ICP-MS. Chem. Geol 207 (3-4), 135-145.

Hedenquist, J., & Arribas, A. (2000). Epithermal gold deposits: I. Hydrothermal processes in intrusion-related systems, and II. Characteristics, examples and origin of epithermal gold deposits. Society of Economic Geologist, 31, 13-63.

Henley, R., & Hedenquist, J. (1986). Introduction to the geochemistry of active and fossil geothermal systems. In: Henley RW, Hendequist RW, Roberts PJ (eds): Guide to the active epithermal systems and precious metal deposits of New Zealand. Monography Series Mineral Deposits, 26, 129-145.

Henry, C. (1975). PhD Dissertation In: Geology and geochronology of the granitic batholith complex, Sinaloa, México. University of Texas , 158.

Henry, C., & Fredrikson, G. (1987). Geology of southern Sinaloa adjacent to the Gulf of California. Geol. Soc. Am. Map Chart Ser, 14.

Henry, C., McDowell, F., & Silver, L. (2003). Geology and geochronology of granitic batholithic complex, Sinaloa, Mexico: implications for cordilleran magmatism and tectonics. Geol. Soc. Am. Spec. Pap., 374, 237-273.

Henshaw, P. (1953). Geology and Ore Deposit of the San Dimas District. Sinaloa and Durango, Private document. 531.

Hilton, D., Hammerschmidt, K., Loock, G., & Friedrichsen, H. (1993). Helium and argon isotope systematics of the cetral Lau Basin and Valu Fa Ridge: evidence of crust/mantle interactions in a back.arc basin. Geochimica et Cosmochimica Acta 57 (12), 2819-2841.

Hilton, D., Fischer, T., & Marty, B. (2002). Noble gases and volatile recycling at subduction zones. . Reviews in Mineralogy and Geochemistry 47 (1), 319-370.

Horner, J., & Enríquez, E. (1999). Epithermal precious metal mineralization in a strike-slip corridor: The San Dimas District, Durango, Mexico. Soc. Econ. Geologist, 1375-1380.

Hurford, A. (2019). An historical perspective on fission-track thermochronology. In: Fission-track thermochronology and its application to geology. Springer, Cham, 3-23.

Kohn, B., Chung, L., & Gleadow, A. (2019). Fission-track analysis: field collection, sample preparation and data acquisition. In: Malusa, M.G. Fitgerald, P.G. eds, Fission-Track Thermochronology and its application to geology. Springer, Cham., 25-48.

Kuiper, K., Deino, A., Hilgen, F., Krisjgsman, W., Renne , P., & Wijbrans, J. (2008). Synchronizing rock clocks of earth history. Science 320 (5875), 500-504.

Kurz, M. (1986). Cosmogenic Helium in a terrestrial igneous rock. Nature 320, 435-439.

Levresse, G., Villarreal-Fuentes, J., Nieto-Samaniego, A., Alexandre, P., Corona-Esquivel, R., & Sole-Viñas, J. (2017). New metallogenic model of telescoped Eocene-Miocene Au-U epithermal mineral deposit in the Placer de Guadalupe District, Chihuahua, Mexico. Ore Geology Reviews, 133-152.

Ludwing, K. (2008). User manual for Isoplot 3.7. A geochronological toolkit for Microsoft Excel. Berkeley Geochronol. Center Spec. Publ. 4, 77.

Montoya-Lopera, P., Levresse, G., Fitz-Diaz, E., Cienfuegos-Alvarado, E., Otero-Trujano, F., & Morales-Puente, P. (en preparación). A detail thermal decrepitation procedure - Ultra Vacuum Borosilicate Glas Line Test - to extract fluid inclusion water from quartz crystals.

Montoya-Lopera, P., Ferrari, L., Levresse, G., Abdullin, F., & Mata, L. (2019 (a)). New insights into the geology and tectonics of the San Dimas mining district, Sierra Madre Occidental, Mexico. Ore Geology Reviews, 273-294.

Montoya-Lopera, P., Levresse, G., Ferrari, L., Orozco-Esquivel, T., Hernandez-Quevedo, G., Abdullin, F., & Mata , L. (2019 (b)). New geological, geochronological and geochemical characterization of the San Dimas mineral system: evidence for a telescoped Eocene-Oligocene Ag/Au deposit in the Sierra Madre Occidental, Mexico. Ore Geology Reviews. V. 118, p. 1-15.

Montoya-Lopera, P., Levresse, G., Ferrari, L., Rizzo, A.L., Urquiza, S., Mata, L. (2020). Genesis of the telescoped Eocene silver and Oligocene gold San Dimas deposits, Sierra Madre Occidental, Mexico: constraints from fluid inclusions, oxygen - deuterium and noble gases isotopes. Ore Geology Reviews. V. 120, p. 1-14.

McDowell, F., & Clabaugh, S. (1979). Ignimbrites of the Sierra Madre Occidental ans their relation to the tectonic history of western Mexico. Geol. S. Am. S., 113-124.

McDowell, F., & Keizer, R. (1977). Timing of mid Tertiary volcanism in the Sierra Madre Occidental between Durango city and Mazatlan, Mexico. Geolo. Soc. Am. Bull, 1479-1487.

McDowell, F., Roldán-Quintana, J., Connelly, J. (2001). Duration of Late Cretaceous-early Tertiary magmatism in east-central Sonora, Mexico. Geol. Soc. Am. Bull. 113, 521–531.

McDowell, F., & McIntosh, W. (2012). Timing of intense magmatic episodes in the northern and central Sierra Madre Occidental, western. Geosphere 8, 1505-1526.

Nemeth, K. (1976). Petrography of the Lower Volcanic Group, Tayoltita-San Dimas District, Durango, Mexico. Unpublished M.A. thesis, 141.

Ortega-Obregon, C., Solari, L., Gomez-Tuena, A., Elias-Herrera, M., Ortega-Gutierrez, F., & Macias-Romo, C. (2014). Permian-Carboniferous arc magmatism in southern Mexico: U-Pb dating, trace element and Hf isotopic evidence on zircon of earliest subduction beneath the western margin of Gondwana. Int. J. Earth Sci 103 (5), 1287-1300.

Paton, C., Hellstrom, J., Woodhead, J., & Hergt, J. (2011). Iolite: Freeware for the visualisation and processing of mass spectrometric data. J. Anal. At. Spectrom. 26 (12), 2508-2518.

Pearce, N., Perkins, W., Westgate, J., Gorton, M., Jackson, S., Neal, C., & Chenery, S. (1997). A compilation of new and published major and trace element data for NIST SRM 610 and NIST SRM 612 glass reference materials. Geostandars and Geoanalytical Research, 21, 115-144.

Petrus, J., & Kamber, B. (2012). A novel approach to laser ablation ICP-MS U-Pb geochronology data reduction. Geoanal. Res. 36 (3), 247-270.

Randall, J. P. (1971). Geology and geochemistry of upper Rio Piaxtla hypothermal deposits and their relationships to nearby precious veins. Unpublished Ph.D. dissertation, 141.

Rizzo, A., Barberi, F., Carapezza, M., Di Piazza, A., Francalanci, L., Sortino, F., & DAlessandro, W. (2015). New mafic magma refilling a quiescent volcano: evidence from He-Ne-Ar isotopes durng the 2011-2012 unrest at santorini, Greece. Geochemistry, Geopgysics.

Solari, L., Gomez-Tuena, A., Bernal, J., Perez-Arvizu, O., & Tanner, M. (2010). U-Pb zircon geochronlogy by an integrated LA-ICPMS microanalytical workstation: achivements in precision and accuracy. Geostand. Geoanal. Res. 34, 5-18.

Schmitz, M., & Bowring, S. (2001). U-Pb zircon and titanite systematics of the Fish Canyon Tuff: An assessment of high-precision U-Pb geochronology and its application to young volcanic rocks. Geochemica et Cosmochimica Acta 65, 2571-2587.

Smith, D., & Hall, D. (1974). Geology of the Tayoltita mine. Society of Mining Engineers of A.I.M.E., Durango, Mexico, 48.

Smith, D., Albinson, T., & Sawkins, F. (1982). Geologic and fluid inclusion studies of the Tayoltita silver-gold vein deposit, Durango, mexico. Society of Economic Geologist, 1120-1145.

Steiger, R., & Jager, E. (1977). Subcommission on geochronology: convention on the use of decay constants in geo-and cosmochronology. Earth and Planetary Science Letters 36, 3, 359-362.

Sillitoe, R. (1993). Giant and bonanza gold deposits in the epithermal environment: Assessment of potential genetic factor in Giant ore deposit, Whiting, B.H., Mason, R., and Hodgson, C.J., eds. . Special Publication 2 Society of Economic Geologist, 125-156.

Valencia, V., Righter, K., Rosas-Elguera, J., Lopez-Martinez, M., Grove, M. (2013). The age and composition of the pre-Cenozoic basement of the Jalisco Block: implications for and relation to the Guerrero composite terrane. Contrib. Miner. Petrol. 166 (3), 801–824.

Vermeesch, P. (2018). IsoplotR: a free and open toolbox for geochronology. Geosci. Front.

Vermeesch, P. (2017). Statistic for LA-ICP-MS based fission track dating. Chem. Geol. 456, 19-27.

Vermeesch, P. (2009). RadialPlotter: a Java application for fission track, luminescence and other radial plots. . Radiat. Meas. V. 44, 409-410.

Wendt, I., & Carl, C. (1991). The statistical distribution of the mean squared weighted deviation. Chemical Geology 86, 275-285.

Wilson, F.O., Rocha, S. (1949). Coal deposits of the Santa Clara district near Tónichy, Sonora, México. U.S. Geol. Surv. Bull. 962A. 80.

Wiedenbeck, M., Alle, P., Corfu, F., Griffin, W., Meier, M., Oberli, F., & Spiegel, W. (1995). Three natural zircon standards for U-Th-Pb, Lu-Hf, trace element and REE analyses. Geostand. Newslett. 19 (1), 1-23.

York, D., Evensen, N., Lopez-Martinez, M., & De Basabe-Delgado, J. (2004). Unified equations for the slope, intercep, and standard errors of the best straight line. American Journal of Physics, 72, 3, 367-375.

Zamora-Vega, O., Richards, J., Spell, T., Dufrane, S., & Williamson, J. (2018). Multiple mineralization events in the Zacatecas Ag-Pb-Zn-Cu-Au district, and their relationship to the tectonomagmatic evolution of the Mesa Central, Mexico. Ore Geology Reviews, 519-561.

Zotov, A., Kudrin, A., Levin, K., Shikina, N., & VarYash, L. (1995). Experimental studies of the solubility and complexing of selected ore elements (Au, Ag, Cu, Mo, As, Sb, Hg) in aqueous solution. In: Shmulovich, K.L., Yardley, B.W.D. and Gonchar, G.G. (eds) fluids in the crust. Equilibrium and transport properties, 95-138.

Capítulo 7: Anexos

Anexo 1: Material suplementario del artículo: Montoya-Lopera, P., Ferrari, L., Levresse, G., Abdullin, F., Mata, L. 2019. New insights into the geology and tectonics of the San Dimas mining district, Sierra Madre Occidental, Mexico. Ore Geology Reviews. V. 105, p. 273-294

- Resultados completos geocronología U-Pb en circón
- Resultados completos geocronología Trazas de Fisión en apatito
- Imágenes petrográficas completas macro y micro de toda la columna estratigráfica

Descargar el material suplementario en la siguiente link

https://www.sciencedirect.com/science/article/pii/S0169136818306930?via%3Dihub

Anexo 2: Material suplementario del artículo: Montoya-Lopera, P., Levresse, G., Ferrari, L., Orozco-Esquivel, T., Hernán-Quevedo, G., Abdullin, F., Mata, L. 2019. New geological, geochronological and geochemical characterization of the San Dimas mineral system: Evidence for a telescoped Eocene-Oligocene Ag/Au deposit in the Sierra Madre Occidental, Mexico. Ore Geology Reviews. V. 118, p. 1-15

- Procedimientos analíticos
- Resultados completos de geoquímica en cristales de Au y Ag
- Resultados completos de geocronología U-Pb en circón
- Resultados completos de geocronología ^{40}Ar-^{39}Ar
- Resultados completos geoquímica de elementos traza en circón (U-Pb)

Descargar el material suplementario en la siguiente link

https://www.sciencedirect.com/science/article/pii/S0169136819302975?via%3Dihub

Anexo 3: Material suplementario del artículo: Montoya-Lopera, P., Levresse, G., Ferrari, L., Rizzo, A.L., Urquiza, S., Mata, L. 2020. Genesis of the telescoped Eocene silver and Oligocene gold San Dimas deposits, Sierra Madre Occidental, Mexico: constraints from fluid inclusions, oxygen - deuterium and noble gases isotopes. Ore Geology Reviews. V. 120, p. 1-14

- Procedimientos analíticos
- Resultados completos de estudios de inclusiones fluidas
- Resultados completos de geoquímica isotópica (isótopos estables)
- Resultados completos de geoquímica isotópica (gases nobles)

Descargar el material suplementario en la siguiente link

https://www.sciencedirect.com/science/article/pii/S016913681930928X?via%3Dihub